

# Frequency Modulation Atomic Force Microscopy on Biomolecules: Force Measurements and High Resolution Images of DNA

THÈSE N° 5846 (2013)

PRÉSENTÉE LE 20 AOÛT 2013

À LA FACULTÉ DES SCIENCES DE BASE  
LABORATOIRE DE PHYSIQUE DE LA MATIÈRE VIVANTE  
PROGRAMME DOCTORAL EN PHYSIQUE

ÉCOLE POLYTECHNIQUE FÉDÉRALE DE LAUSANNE

POUR L'OBTENTION DU GRADE DE DOCTEUR ÈS SCIENCES

PAR

Andrea CERRETA

acceptée sur proposition du jury:

Prof. V. Savona, président du jury  
Prof. G. Dietler, directeur de thèse  
Prof. R. Garcia, rapporteur  
Prof. O. Sahin, rapporteur  
Prof. F. Stellacci, rapporteur



ÉCOLE POLYTECHNIQUE  
FÉDÉRALE DE LAUSANNE

Suisse  
2013



Ai miei nonni Alfonso e Marianna:  
ricorderò sempre la sapienza nei gesti  
delle vostre mani antiche e laboriose  
e la dignità del vostro vivere.



# Acknowledgements

I would like to express my deepest gratitude to prof. Giovanni Dietler for giving me the opportunity to make this experience. The four years I spent in Lausanne greatly contributed to my professional and personal growth. Giovanni has always been ready to give me suggestions, to help when possible in the lab work, to propose interesting articles to read or talks to listen. Moreover, he always supported me and believed in my skills especially in the moments in which I doubted of them, and for this I am in debt to him. His intelligence, generosity and humour are qualities that every Ph D. student would like to find in a thesis director.

The second person that I have to thank is Dr. Dusan Vobornik. We shared the work on this project and his experience and his open-mindedness were fundamental to reach the results presented in this thesis. I learnt a lot of things from him about how to do research and how to focus on the main points of a subject, without getting lost in details (e.g. avoiding to redemonstrate the fundamental physics from scratch, as I love to do!). It was a pleasure to work with him and I enjoyed all the conversations we had during the coffee breaks, and the jokes and music we shared in our office.

Any activity of research in the LPMV group would be impossible without the precious work of an irreplaceable member, that is Christine Vuichoud. Her competence and helpfulness are unique qualities that made considerably easier my life at EPFL. I also had the chance to know her as a very pleasant person mostly during our lunches at Banane and during lab outings. I want to thank her also for all the improvements that she made me do with my French, and I hope that she found useful my short tutorials of Italian (in spite of my “strange” accent!).

The LPMV group is a multicultural environment in which people are ready to share their knowledge and to help colleagues. I learnt a lot staying here and I am glad to have had the possibility to work in this group, in which there is an enjoyable and stimulating atmosphere. I would like to thank all of the LPMV members, and in particular Dr. Andrzej Kulik and Dr. Sergey Sekatskii for their availability in answering to the infinite number of questions I made them during this years. Among the Ph. D. students that shared this time in the LPMV group with me, I want to thank in particular Simone Ruggeri, who was a friend more than a colleague and shared with me not only the work life, but especially beers, concerts and night walks in Lausanne.

All researchers and students in our group are lucky to collaborate with an efficient technical staff. I would like to thank here: Caroline Maillard for the precious work in the preparation of the samples I studied during my Ph. D.; Michel Kessous for fixing the (frequent) problems to my laptop; Jean-Luc Baumberger for “taking care” of the cryo-AFM lab and for the practical

## Acknowledgements

---

help in the construction of a new microscope. I want to acknowledge the skillfulness and the kindness of all of them.

The private thesis defense I recently made was an exceptional occasion to discuss my project with a jury made by extremely competent and renowned members, which I would like to thank again for their participation and for the interesting exchange we had during the defense. These members are prof. Vincenzo Savona (president of the jury) and prof. Francesco Stellacci from EPFL, prof. Ricardo García from the Instituto de Microelectrónica of Madrid and prof. Ozgur Sahin from Columbia University.

I would like to thank very much my father Pietro, my mother Lina and my brothers Davide and Raffaele for their continuous presence in my life, in spite of the distance that keeps us far. I would like that everything I do is a reason for them to be proud of me. Together with them, I want to say thanks also to my friends in Lausanne, Calitri and Rome for getting behind me, hoping to preserve their nice friendship in the future.

Finally, there is a person that took care of me with love and patience during the redaction of this thesis. I would like to show all my gratitude for her closeness, hoping to share other moments with her for a long time. Grazie Julia.

*Lausanne, 15th July 2013*

A. C.

# Abstract

My thesis explores the conformation of DNA molecules in UHV by means of atomic force microscopy (AFM). The aim is to determine if a DNA molecule can remain in its physiological state when inserted in highly dehydrated environments. The interest in this subject arises from the possible applications of DNA molecules in several fields of nanotechnology, where ambient conditions can be far from the physiological ones. I used different AFM techniques to characterize the DNA structure in vacuum, namely Frequency Modulation non-contact AFM, force mapping, and constant height imaging. Moreover, I modeled the interaction of the DNA with the AFM probe in order to interpret apparent incongruities between experimental data and the predicted DNA structure.

In the first chapter of this thesis, I will present general physical concepts governing atomic force microscopy. First of all, I will explain the notion of scanning probe microscopy and illustrate the main components of the atomic force microscope (the scanner, the cantilever probe, the detector and the feedback system). The difference between static and dynamic mode of AFM operation will be explained. The dynamic mode, that is the AFM technique in which the probe is forced to oscillate over the sample surface, is the one implemented on my microscope. Therefore, I will discuss the cantilever dynamics under the influence of the probe-sample forces making some simplifying assumptions. I will define and compare Amplitude Modulation (AM) and Frequency Modulation (FM) AFM and explain the advantages of using the FM feedback in vacuum. Finally, I will show the mathematical relations that exist between the cantilever frequency detuning and the tip-sample forces. These relations will be of fundamental importance for most of the topics discussed in the following chapters.

In the second chapter I will describe the experimental setup. I will give details about the elements composing the AFM head and about the vacuum chamber containing the microscope. Then I will briefly introduce the electronics and the software used to control the microscope. The third chapter will be dedicated to the AFM measurements made on DNA samples in vacuum. An introductory section will be devoted to the description of the DNA polymorphisms and to the role that DNA has in biology and in other fields of research. I will show measurements made in vacuum on DNA samples prepared in different ways and I will discuss DNA conformation in vacuum. I will introduce two AFM techniques complementary to high resolution AFM imaging that were applied to the study of the DNA structure. One of them consists of the acquisition of a series of spectroscopy curves along the axis of a DNA molecule. The other one is a constant height imaging of DNA molecules.

Finally, I will tackle the issue of the mismatch between the measured height of the DNA

## Acknowledgements

---

molecule and the theoretical DNA diameter. In all AFM experiments made on DNA molecules in dry (air or vacuum) environments, the measured height is always smaller than real DNA diameter. I will show calculations based on the AFM probe-DNA van der Waals interaction that explain to this phenomenon.

**Keywords:** Atomic Force Microscopy, Frequency Modulation, DNA, van der Waals, Hamaker constant, high resolution, UHV, force curves, constant height imaging.



# Résumé

Le sujet de ma thèse est l'étude de la conformation des molécules d'ADN en utilisant la microscopie à force atomique (AFM). Le but est de déterminer si une molécule d'ADN peut rester dans son état physiologique quand elle se trouve dans des environnements extrêmement déshydratés. L'intérêt pour ce sujet est dû à des possibles applications des molécules d'ADN dans plusieurs champs de la nanotechnologie, où les conditions environnementales peuvent être très différentes par rapport à celles physiologiques. J'ai utilisé diverses techniques AFM pour caractériser la structure de l'ADN dans le vide et les résultats de mes expériences sont présentés ici. De plus, j'ai modelé l'interaction de l'ADN avec la sonde AFM pour pouvoir interpréter des incohérences apparentes entre les résultats expérimentaux et la structure prévue de l'ADN.

Dans le premier chapitre de cette thèse, je présenterai des concepts physiques généraux qui gèrent la microscopie à force atomique. Premièrement, j'expliquerai la notion de microscopie à sonde locale et j'illustrerai les composants du microscope à force atomique (le scanner, le levier, le détecteur et le système de feedback). De plus, la différence entre les modes d'opération statique et dynamique de l'AFM sera expliquée. Le mode dynamique, qui est la technique AFM dans laquelle la sonde est forcée à osciller proche de la surface de l'échantillon, est celle qu'est implémentée dans mon microscope. Donc, je discuterai la dynamique du levier soumis à l'influence des forces entre sonde et échantillon, en faisant quelques hypothèses simplificatrices. Je définirai et comparerai l'AFM à modulation d'amplitude (AM) et à modulation de fréquence (FM) et j'expliquerai les avantages d'utiliser le feedback FM dans le vide. Enfin, je montrerai les relations mathématiques qui existent entre la variation de fréquence du levier et les forces entre sonde et échantillon. Ces relations seront d'importance fondamentale pour la majorité des arguments discutés dans les chapitres suivants.

Le deuxième chapitre décrira l'instrumentation. Je donnerai des détails à propos des éléments que composent la tête de l'AFM et à propos de la chambre à vide que contient le microscope. Après j'introduirai brièvement l'électronique et le logiciel utilisés pour contrôler le microscope. Le troisième chapitre sera dédié aux mesures AFM faites sur des échantillons d'ADN sous vide. Une partie introductive sera dédiée à la description des polymorphismes de l'ADN et au rôle que l'ADN a en biologie et dans d'autres champs de recherche. Je montrerai des mesures faites sous vide sur des échantillons d'ADN préparés de différentes façons et je discuterai la conformation de l'ADN sous vide. J'introduirai deux techniques AFM complémentaires à l'imagerie à haute résolution qui étaient appliquées à l'étude de la structure de l'ADN. La première consiste dans l'acquisition d'une série de courbes spectroscopiques le long de l'axe

## Acknowledgements

---

de la molécule d'ADN. La deuxième est l'imagerie à hauteur constante des molécules d'ADN. Je montrerai les résultats expérimentaux de ces techniques.

Pour finir, j'aborderai le problème de la différence entre la hauteur mesurée de la molécule d'ADN et son diamètre théorique. Dans toutes les expériences AFM faites sur les molécules d'ADN en environnement sec (dans l'air ou sous vide), la hauteur mesurée était toujours plus petite par rapport au vrai diamètre de l'ADN. Je montrerai des calculs basés sur l'interaction de van der Waals entre la sonde AFM et l'ADN que fourniront une explication à ce phénomène.

**Mots clés :** Microscopie à force atomique, Modulation de Fréquence, ADN, van der Waals, constante d'Hamaker, haute résolution, ultravide, courbes de force, imagerie à hauteur constante.

# Contents

<b>Acknowledgements</b>	<b>v</b>
<b>Abstract (English/Français)</b>	<b>vii</b>
<b>1 Atomic force microscopy</b>	<b>1</b>
1.1 Introduction . . . . .	1
1.2 Description of the technique . . . . .	2
1.3 Cantilever dynamics . . . . .	4
1.3.1 Periodic excitation and quality factor . . . . .	6
1.3.2 Effects of tip-sample interactions on the oscillation . . . . .	8
1.4 Amplitude and frequency modulation feedbacks . . . . .	9
1.4.1 Noise sources in FM AFM . . . . .	11
1.5 Force and frequency shift . . . . .	12
<b>2 Experimental setup</b>	<b>15</b>
2.1 Home made AFM . . . . .	15
2.1.1 Tips . . . . .	20
2.2 Commercial electronics and software . . . . .	21
2.2.1 Software . . . . .	23
2.2.2 Amplitude calibration . . . . .	27
<b>3 Revealing the sub-molecular structure of DNA</b>	<b>31</b>
3.1 DNA and its polymorphisms . . . . .	31
3.2 DNA in biology and DNA in nanotechnology . . . . .	34
3.3 AFM imaging of DNA . . . . .	36
3.4 DNA imaging in vacuum . . . . .	37
3.4.1 Mg <sup>2+</sup> and APTES deposition protocols . . . . .	38
3.4.2 Statistical analysis of DNA . . . . .	38
3.4.3 Substrate roughness . . . . .	43
3.4.4 High resolution images . . . . .	44
3.5 Constant height imaging . . . . .	47
3.5.1 Experimental details . . . . .	49
3.5.2 Frequency shift maps on DNA and APTES . . . . .	51
3.6 Spectroscopy measurements on DNA . . . . .	56

## Contents

---

3.6.1	Drift correction . . . . .	57
3.6.2	Grooves in topography vs. grooves in force periodicity along DNA . . . . .	58
3.6.3	Grooves with a blunt 10 nm radius tip . . . . .	61
3.6.4	Sphere-chain of spheres: grooves contrast . . . . .	62
<b>4</b>	<b>Quantitative AFM height measurements</b>	<b>65</b>
4.1	Measured DNA height with DLC and silicon tips . . . . .	65
4.2	Tip and DNA models for the AFM height calculations . . . . .	68
4.2.1	Van der Waals potential energy for simple geometries . . . . .	69
4.2.2	Modeling the tip as a sphere . . . . .	70
4.2.3	Cylinder vs. sphere van der Waals interaction . . . . .	76
4.2.4	Chain of spheres vs. sphere van der Waals interaction . . . . .	82
4.3	Results of calculations . . . . .	84
4.3.1	Calculation of the DNA height in FM AFM . . . . .	85
4.3.2	Calculations of the groove contrast in FM AFM . . . . .	89
4.3.3	Applicability to the study of other biomolecules . . . . .	91
<b>5</b>	<b>Conclusions</b>	<b>95</b>
	<b>Bibliography</b>	<b>97</b>
	<b>Curriculum Vitae</b>	<b>103</b>

# 1 Atomic force microscopy

In this chapter I will introduce basic concepts of Atomic Force Microscopy (AFM). The advantages of AFM with respect to other microscopies will be mentioned. A simplified but quantitative description of the cantilever dynamics will be given. Major AFM feedback mechanisms will be introduced, explained and compared. Finally, I will show the advantages that led me to use the Frequency Modulation AFM in this thesis.

## 1.1 Introduction

The best resolution achievable with conventional lens-based light microscopy is of the same order of magnitude as the wavelength of the incident light. This is the so-called diffraction limit. Therefore, objects with dimensions of less than several hundreds of nanometers cannot be imaged with an optical microscope. Different approaches were developed to decrease this limit, such as X-Ray or Electron Microscopy, which are similar to optical microscopy but use lower wavelengths.

Recently, the combination of confocal microscopy with fluorescence gave origin to several techniques such as Stimulated Emission Depletion (STED) or Photoactivated Localization Microscopy (PALM), which are capable of enhancing resolution by one order of magnitude with respect to optical microscopy [1]. Yet, the resolution limit is still approximately 10÷50 nm.

Scanning Probe Microscopy (SPM) appeared in 1980's and is a conceptual revolution in the field of microscopy. In 1986 Binnig and Rohrer were awarded with Nobel Prize in Physics for the development of the first SPM technique: the Scanning Tunneling Microscopy (STM) [2], which they invented in 1981. AFM was introduced in 1986 by Binnig, Quate and Gerber [3]. AFM is a versatile tool which can function in a wide range of environmental conditions and, as opposed to STM, can image both conductive and dielectric samples. AFM is used in very different fields of research that span from biology to nanotechnology and surface science. In this chapter, I will give a basic introduction about how an AFM microscope works.

In particular, I will focus the attention on one mode of operation, the Frequency Modulation (FM) AFM [4], which has been used in our experiments. I will also show how information about the interaction forces between the AFM probe and the sample can be extracted with FM AFM.

### 1.2 Description of the technique

SPM techniques are based on the local interaction of the sample surface with a probe. The sample can be moved with respect to the probe using piezoelectrical scanners, in vertical ( $z$ ) or horizontal ( $x,y$ ) directions. The movement of the probe over a selected area on the surface is represented in fig. 1.2 b). The probe interacts with the sample moving sequentially along parallel lines. Each line is divided in a fixed number of pixels. When the tip is over a certain pixel, several signals can be measured, recorded and assigned to the pixel itself. Once that the scan is finished, pixelated maps representing the variation of the selected signal over the area can be visualized. SPM microscopes can measure the topography (fig. 1.2), but also other properties (conductivity, elasticity, etc.) of the sample.

Probes commonly used in AFM are cantilever oscillators of micrometer dimensions with a sharp tip at the free end (see fig. 1.1). They can have different geometries, among which triangular or rectangular levers are the most used (see fig. 1.1). Quartz tuning forks are sometimes used, mostly as oscillators for dynamic AFM applications (fig. 1.1 d)). The dimensions of the tip apex can be chosen depending on the length scale that one wants to resolve. They typically range from 1 to 30 nm in radius. When measuring, the tip apex is approached to the surface of the sample in order to sense the tip-sample interaction forces. These forces can have different

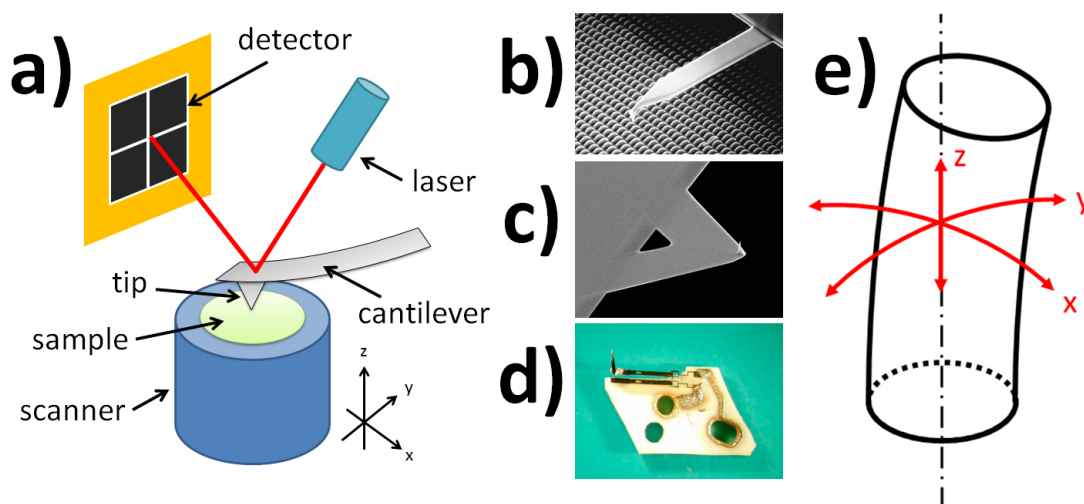


Figure 1.1: **a)** Sketch of an AFM microscope where a rectangular cantilever and an optical detecting system are used. **b)** Rectangular cantilever. **c)** Triangular cantilever. **d)** Tuning fork probe. **e)** Representation of the movements of the cylindrical scanner.

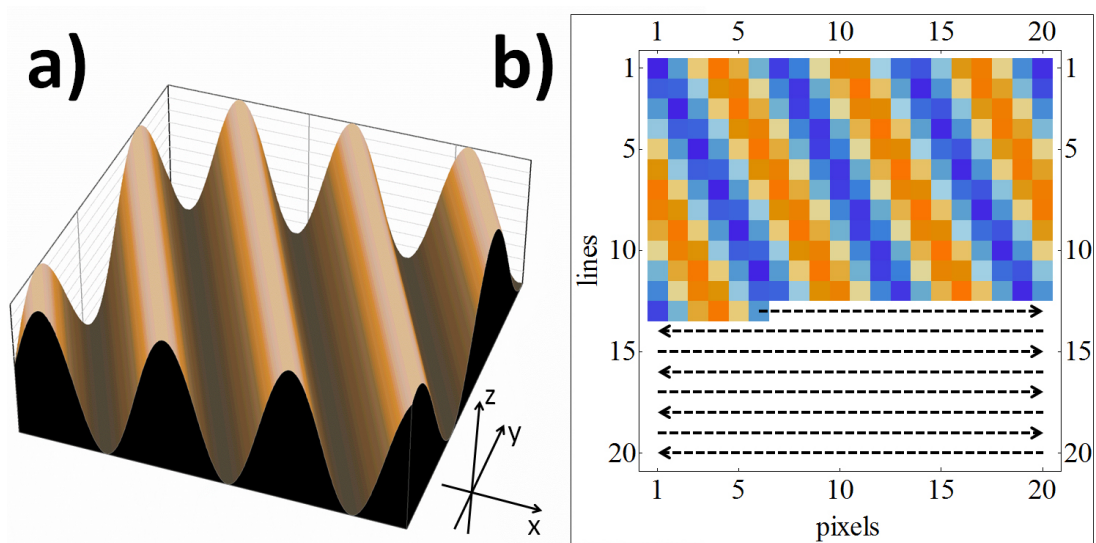


Figure 1.2: **a)** A surface presenting a periodical corrugation. **b)** The probe moves along lines recording data for each pixel (in this case, the local topography).

nature and can be summarized according to their typical range. Electrostatic and magnetic forces are long range (hundreds of nanometers) contributions. At distances of a couple of nanometers, van der Waals and capillary forces can be felt by the probe. At very short range (sub-nanometer) we can observe the formation of chemical bonds, Pauli repulsive forces and elastic effects due to the deformation of both the sample and the tip.

The simplest realization of AFM is the so called *static mode*, in which the probe is approached to the surface in such a way that forces cause an elastic deformation of the probe. For a cantilever probe, the probe bending can be monitored through an optical detection system, as shown in fig. 1.1 a). A laser beam is focused on the back of the cantilever and the reflected light is collected by a 4-quadrant photodiode detector. The most efficient way to determine the topography is to use a feedback system that allows to move vertically the scanner in such a way that the cantilever bending is maintained almost constant while scanning the surface in the  $(x,y)$  plane. This means that when the laser spot moves on the detector, the feedback system reacts extending or compressing the scanner in order to recover the reference spot position. The vertical displacement  $z$  of the scanner is recorded for each pixel and the  $z$  map corresponds to the sample topography. In our setup, the scanner is a piezoelectric cylinder divided in four quadrants. The application of different voltages to each quadrant can move the scanner in the three directions. The cylinder bending is small compared with its dimensions so that we can approximate it to be a horizontal movement (fig. 1.1 e)).

The interaction of the probe with the sample influences quantities such as the cantilever deflection, its oscillation amplitude and frequency. The detection system measures these quantities and each of them is converted into an electric signal  $V(t)$ . The mechanism to determine the sample topography is based on the continuous attempt to minimize the variation

## Chapter 1. Atomic force microscopy

---

$\Delta V(t)$  of one of these signals with respect to a reference value  $V_0$  imposed by the user. This task is accomplished by a feedback loop system on the scanner vertical elongation  $z(t)$ . In our setup the error on the feedback signal  $\Delta V(t)$  is converted in a vertical displacement  $\Delta z(t)$  of the piezo crystal by a proportional-integral (PI) controller:

$$\Delta z(t) = K_P \left( \Delta V(t) + \frac{1}{\tau} \int_0^t \Delta V(t') dt' \right) \quad (1.1)$$

where  $K_P$  and  $\tau$  are parameters to optimize according to the sample dimensions and the scan rate. The topography of the sample is then obtained assigning a  $z(t)$  to each pixel of the scanned area.

Static mode AFM performs the best when the probe is pushed enough towards the sample to sense strong repulsive forces. However, the strong interaction between the tip apex and the surface can cause deformations and often damages both the sample and the tip. *Dynamic mode* AFM techniques have been introduced in order to reduce the damage to the sample and to the tip. In this mode a dithering piezo is used to induce an oscillation of the cantilever. Tip-sample forces have an effect on the oscillation amplitude, frequency and phase. These signals are again collected by the 4-quadrant photodiode and can be used as feedback signals.

### 1.3 Cantilever dynamics

In this section I will describe the dynamics of the oscillating probe in presence of an external field of forces, making a few simplifications. The discussion below follows to large extent the reasoning presented in [5]. The probe will be modeled as a point-like damped harmonic oscillator with mass  $m$ , spring constant  $k$  and damping coefficient  $\beta$ . The general equation of this oscillator is:

$$m \ddot{x}(t) + \beta \dot{x}(t) + k x(t) = \sum_i F_i \quad (1.2)$$

where each term  $F_i$  represents an external force. When none of these forces is applied to the oscillator, the equation reduces to:

$$m \ddot{x}(t) + \beta \dot{x}(t) + k x(t) = 0 \quad (1.3)$$

The general solution of this second order homogeneous differential equation is:

$$x(t) = c_1 e^{s_1 t} + c_2 e^{s_2 t} \quad (1.4)$$



where  $c_1$  and  $c_2$  are constants fixed by the boundary conditions and:

$$s_{1,2} = -\frac{\beta}{2m} \pm \sqrt{\left(\frac{\beta}{2m}\right)^2 - \frac{k}{m}} \quad (1.5)$$

Calling  $\gamma = \frac{\beta}{2m}$  e  $\omega_0 = \sqrt{\frac{k}{m}}$ , we can write:

$$s = -\gamma \pm \sqrt{\gamma^2 - \omega_0^2} \quad (1.6)$$

Then eq. (1.4) can be rewritten as:

$$x(t) = e^{-\gamma t} \left\{ c_1 e^{+\sqrt{\gamma^2 - \omega_0^2} t} + c_2 e^{-\sqrt{\gamma^2 - \omega_0^2} t} \right\} \quad (1.7)$$

The multiplicative factor  $e^{-\gamma t}$  shows that oscillations are damped with a lifetime  $\tau = 1/\gamma$ . The solution depends on the sign of the discriminant  $\Delta = \gamma^2 - \omega_0^2$ . In cases in which the viscosity of the environment is low, we can assume that  $\gamma < \omega_0$  and study only the under-damped solution. Defining  $\omega = \sqrt{-\Delta} = \sqrt{\omega_0^2 - \gamma^2} > 0$ , we can write:

$$x(t) = e^{-\gamma t} \left\{ c_1 e^{+i\omega t} + c_2 e^{-i\omega t} \right\} \quad (1.8)$$

while the velocity  $v(t)$  is:

$$v(t) = e^{-\gamma t} \left\{ c_1 (-\gamma + i\omega) e^{+i\omega t} + c_2 (-\gamma - i\omega) e^{-i\omega t} \right\} \quad (1.9)$$

Fixing the boundary conditions  $x(0) = x_0$  and  $v(0) = v_0$ , we find  $c_{1,2} = \frac{x_0}{2} \pm \frac{v_0 + \gamma x_0}{i2\omega}$  and then:

$$x(t) = e^{-\gamma t} \left\{ x_0 \cos(\omega t) + \frac{v_0 + \gamma x_0}{\omega} \sin(\omega t) \right\} \quad (1.10)$$

In order to simplify this expression, we can define  $A_0 \cos \delta = x_0$  and  $A_0 \sin \delta = -\frac{v_0 + \gamma x_0}{\omega}$  and consequently obtain:

$$x(t) = A_0 e^{-\gamma t} \cos(\omega t + \delta) \quad (1.11)$$

where:

$$A_0 = \sqrt{x_0^2 + \left(\frac{v_0 + \gamma x_0}{\omega}\right)^2} \quad (1.12)$$

$$\delta = \arctan\left(-\frac{\nu_0 + \gamma x_0}{\omega x_0}\right) \quad (1.13)$$

The energy stored in the oscillator at the time  $t = 0$  is:

$$E_{tot} = \frac{m\nu_0^2}{2} + \frac{kx_0^2}{2} \quad (1.14)$$

and it is progressively lost due to the presence of frictional term.

### 1.3.1 Periodic excitation and quality factor

For an AFM probe, oscillations are sustained using a dithering piezoelectric element. We can suppose this exciting force to be cosinusoidal, with an angular frequency  $\omega_e$ . The equation of forces is then modified in this way:

$$m \ddot{x}(t) + \beta \dot{x}(t) + k x(t) = F_e \cos(\omega_e t) \quad (1.15)$$

The general solution of this equation is the sum of the previous homogeneous solution and a special solution for the complete expression, that we can find using phasors:

$$m \frac{d^2 \tilde{x}(t)}{dt^2} + \beta \frac{d\tilde{x}(t)}{dt} + k \tilde{x}(t) = F_e e^{i\omega_e t} \quad (1.16)$$

Assuming  $\tilde{x}(t) = A_e e^{i\delta_e} e^{i\omega_e t} = \tilde{A}_e e^{i\omega_e t}$ , we obtain:

$$\tilde{A}_e (-m\omega_e^2 + i\beta\omega_e + k) = F_e \quad (1.17)$$

and then:

$$\tilde{A}_e = \frac{F_e}{m} \frac{1}{\omega_0^2 - \omega_e^2 + i2\gamma\omega_e} = \frac{F_e}{m} \frac{\omega_0^2 - \omega_e^2 - i2\gamma\omega_e}{[(\omega_0^2 - \omega_e^2)^2 + (2\gamma\omega_e)^2]} \quad (1.18)$$

and it can be easily derived that:

$$A_e = \frac{F_e}{m} \frac{1}{\sqrt{(\omega_0^2 - \omega_e^2)^2 + (2\gamma\omega_e)^2}} \quad (1.19)$$

$$\delta_e = \arctan\left(-\frac{2\gamma\omega_e}{\omega_0^2 - \omega_e^2}\right) \quad (1.20)$$

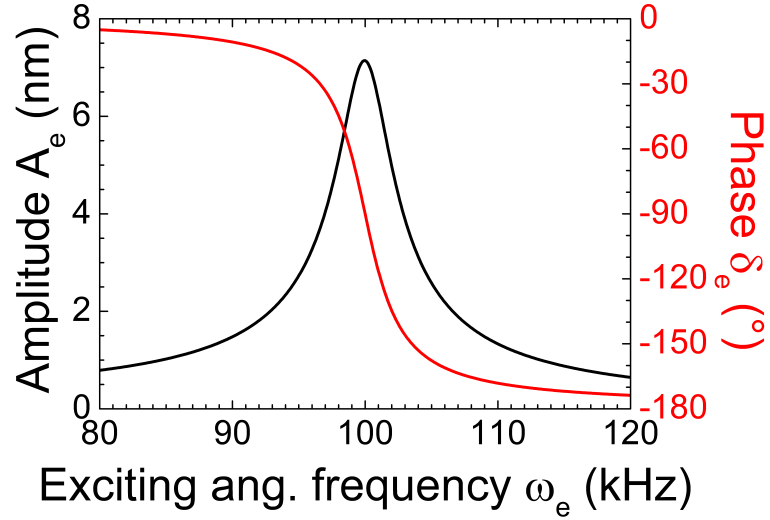


Figure 1.3: Amplitude (black) and phase (red) vs. exciting angular frequency. Parameters:  $\omega_0 = 100$  kHz,  $\gamma = 2000$  Hz,  $m = 3.5 \times 10^{-11}$  kg,  $F_e = 100$  pN.

The general solution for the forced oscillator is then:

$$x(t) = A_0 e^{-\gamma t} \cos(\omega t + \delta) + A_e \cos(\omega_e t + \delta_e) \quad (1.21)$$

For  $t \gg 1/\gamma$  only the second term remains and the system oscillates at the angular frequency  $\omega_e$  of the external force. In the steady state the oscillator behaves like a simple (not damped) harmonic oscillator, in the sense that for each cycle of oscillation the damping is exactly compensated by the energy supplied by the external force. The work can be calculated as  $W = \int F dx = \int F v dt$ . Knowing that  $v(t) = -\omega_e A_e \sin(\omega_e t + \delta_e)$  and that  $F_{fric} = -\beta v(t)$ , it can be found that:

$$|W_{fric}(T)| = \pi \beta \omega_e A_e^2 \quad (1.22)$$

Using the analogy with the simple harmonic oscillator, the energy stored in the steady state is:

$$E_{tot} = \frac{1}{2} m v_{max}^2 = \frac{1}{2} m \omega_e^2 A_e^2 \quad (1.23)$$

The quality factor  $Q$  is an evaluation of the oscillator efficiency in storing energy and it represents the ratio between the total energy of the excited oscillator and the energy dissipated in a cycle, at  $\omega_e = \omega_0$ :

$$Q = 2\pi \frac{E_{tot}}{|W_{fric}(T)|} = \frac{m\omega_0}{\beta} = \frac{\omega_0}{2\gamma} \quad (1.24)$$

The  $Q$  factor is linked to the shape of the peak of  $E_{tot}(\omega_e)$ . It is easy to verify that the stored energy reaches the half of its peak value for  $\omega_e = \pm\gamma + \sqrt{\gamma^2 + \omega_0^2}$  and then the width of the peak at the half of its maximum is  $\Delta\omega = 2\gamma$ . As a consequence, the  $Q$  factor corresponds to the ratio between the peak angular frequency and the peak FWHM width:

$$Q = \frac{\omega_0}{\Delta\omega} \quad (1.25)$$

This means that a narrower resonance curve has a higher  $Q$  factor. From eq. (1.23) we can see that this statement holds also for the peak of the amplitude, although there is not a simple mathematical relation between  $Q$  and the width of this peak as for eq. (1.25). As it will be discussed later, the  $Q$  factor plays an important role in the AFM feedback performances and on the signal to noise ratio and therefore it must be calculated exactly when characterizing our oscillator. A way to do it is calculating the derivative of the phase  $\delta_e$  with respect to  $\omega_e$  at resonance:

$$\left. \frac{\partial \delta_e}{\partial \omega_e} \right|_{\omega_e=\omega_0} = - \frac{2\gamma(\omega_0^2 + \omega_e^2)}{(\omega_0^2 - \omega_e^2)^2 + (2\gamma\omega_e)^2} \Bigg|_{\omega_e=\omega_0} = -\frac{1}{\gamma} \quad (1.26)$$

and so:

$$Q = -\frac{\omega_0}{2} \left. \frac{\partial \delta_e}{\partial \omega_e} \right|_{\omega_e=\omega_0} \quad (1.27)$$

### 1.3.2 Effects of tip-sample interactions on the oscillation

When the sample is at close separation with respect to the oscillating probe, tip-sample forces  $F_{ts}$  must be considered in eq. (1.2) and they will affect both the amplitude and the frequency of the oscillation. In order to see this in a simple way, we will consider the tip-sample forces as a slowly varying function of the distance:

$$F_{ts}(x) = F_0 + \left. \frac{\partial F_{ts}}{\partial x} \right|_{x=x^*} x + \frac{1}{2} \left. \frac{\partial^2 F_{ts}}{\partial x^2} \right|_{x=x^*} x^2 + \dots \simeq F_0 + k' x \quad (1.28)$$

where the separation  $x$  between the sample and the tip apex ranges in a neighborhood of  $x^*$  and  $k' = \partial_x F_{ts}(x^*)$ . It must be noticed that this approximation is valid for amplitudes small with respect to the range of distances considered. Summing  $F_{ts}$  to the cantilever excitation force, we have:

$$m \ddot{x}(t) + \beta \dot{x}(t) + k x(t) = F_0 + k' x(t) + F_e \cos(\omega_e t) \quad (1.29)$$

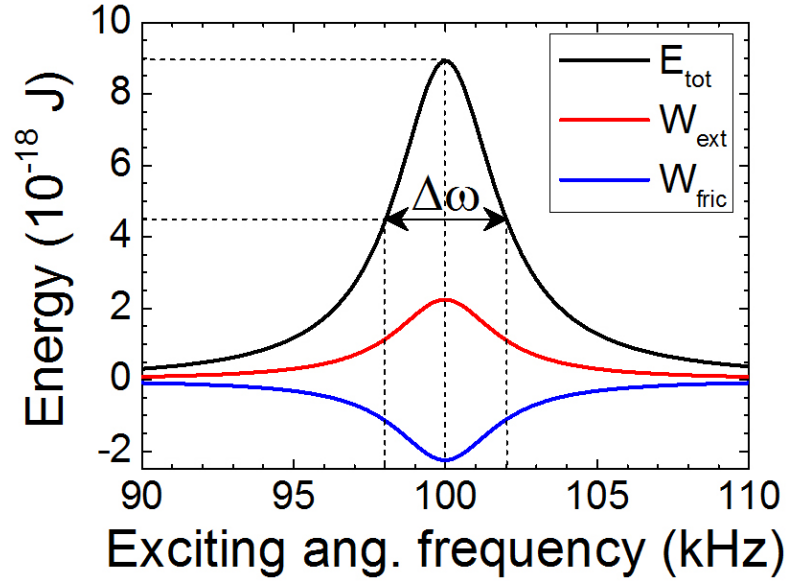


Figure 1.4: Stored energy (black), energy per cycle supplied by the external solicitation (red), and energy per cycle lost by friction (blue) vs. exciting angular frequency. Parameters:  $\omega_0 = 100$  kHz,  $\gamma = 2000$  Hz,  $m = 3.5 \times 10^{-11}$  kg,  $F_e = 100$  pN.

The apparent complexity of this expression is easily resolved defining  $y(t) = x(t) - \frac{F_0}{k-k'}$  and  $\omega'_0 = \sqrt{\frac{k-k'}{m}}$ , and writing:

$$m \ddot{y}(t) + \beta \dot{y}(t) + m\omega_0'^2 y(t) = F_e \cos(\omega_e t) \quad (1.30)$$

The solution for  $y(t)$  is identical to eq. (1.21), and substituting  $x(t)$  we arrive to:

$$x(t) = \frac{F_0}{k-k'} + A_0(\omega'_0) e^{-\gamma t} \cos(\omega(\omega'_0) t + \delta(\omega'_0)) + A_e(\omega'_0) \cos(\omega_e t + \delta_e(\omega'_0)) \quad (1.31)$$

where  $\omega(\omega'_0) = \sqrt{\omega_0'^2 - \gamma^2}$ . Let's imagine the tip oscillating during the scan far enough from a flat surface, in such a way that tip-sample forces can be ignored. The cantilever dynamics is then determined by the eq. (1.19)-(1.21). If suddenly the tip encounters a step on the sample surface, the oscillation is affected by this change. The cantilever deflects itself modifying its average position, an intermediate state lasts until  $t \gg 1/\gamma$  and finally the oscillation becomes again harmonic, with different amplitude and phase.

## 1.4 Amplitude and frequency modulation feedbacks

This simplified model illustrates quite well how Amplitude Modulation (AM) AFM works. An excitation with constant amplitude, frequency and phase is sent to the cantilever through

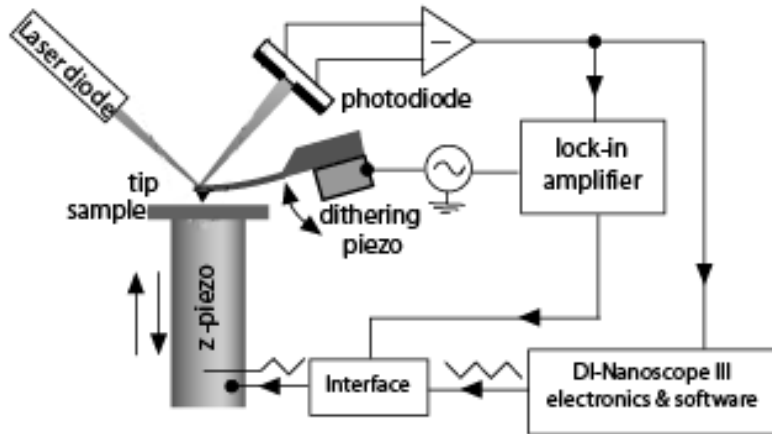


Figure 1.5: Typical scheme of AM AFM.

the dithering piezo (see fig. 1.5). The interaction with the sample modifies the cantilever oscillation amplitude  $A(t)$ . Setting a reference value  $A_{set}$  for this amplitude, a feedback loop system allows changing the relative tip-sample distance during the scan in order to maintain the value of  $A(t)$  as close as possible to  $A_{set}$ . Eq. (1.31) shows that there is an experimental limitation to the use of AM mode in conditions of low dissipation, as it happens in vacuum. For high values of  $Q$ , the time to reach the steady state solution becomes longer and consequently the scan speed has to be decreased. Nevertheless, AM AFM is a commonly used technique to image samples in air or in liquid.

Several ways to decouple the scan speed from the  $Q$  factor have been developed to improve the AFM performance in vacuum, and among them the Frequency Modulation (FM) AFM. To understand how it works let's consider a damped oscillator without external forces, as the one described by eq. (1.11). In these conditions the cantilever oscillates with a frequency  $\omega = \sqrt{\omega_0^2 - \gamma^2}$ , progressively reducing its amplitude. In order to sustain this oscillation, a driving force with the same frequency  $\omega$  must be sent to the cantilever. Moreover, the energy exchange is maximized if the driving signal has a phase difference of  $90^\circ$  with respect to the oscillation of the cantilever. FM AFM accomplishes these two tasks using the same deflection signal collected by the detector to create the driving signal (fig. 1.6). The deflection signal is amplified, phase shifted and then sent back to the cantilever. When tip-sample forces modify  $\omega$ , the closed loop system allows changing the driving frequency in such a way that the cantilever is excited always at its resonant frequency. The main advantage of FM is that the time the system takes to react to a variation of the cantilever resonant frequency is of the same order of magnitude as the oscillation period [6]. As for AM AFM, a value of the *frequency shift*  $\Delta f_{set}$  can be chosen and the elongation of the scanner is changed in order to keep  $\Delta f(t)$  close to the reference value. The amplitude of the driving signal can be set constant or modulated to maintain the cantilever amplitude constant.

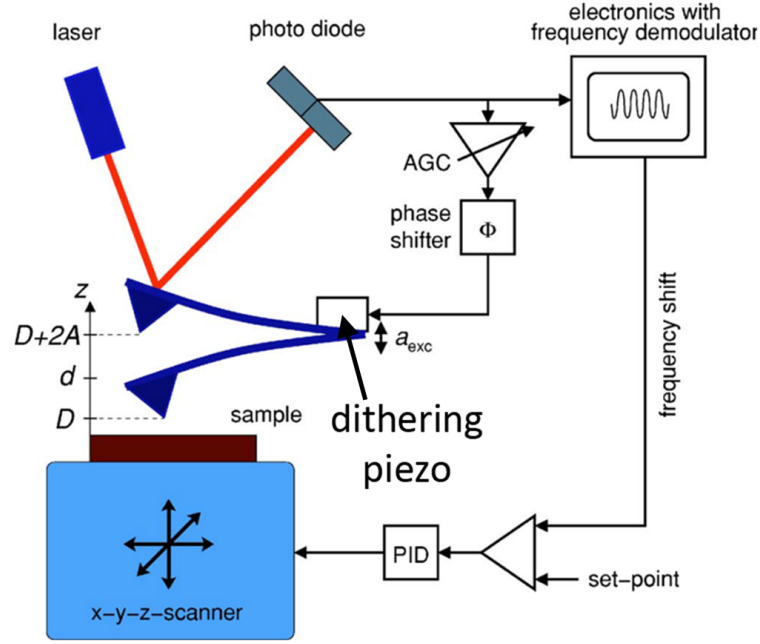


Figure 1.6: Scheme of FM AFM (readapted from [7]).

#### 1.4.1 Noise sources in FM AFM

Several sources of noise can affect the FM measurement. First of all there is the thermal noise, which introduces an indetermination on the resonant frequency. It can be evaluated as [4]:

$$\delta f_{th} = \sqrt{\frac{f_0 k_B T B}{\pi k Q A_0^2}} \quad (1.32)$$

where  $f_0$  is the resonant frequency far from the sample,  $k_B$  is the Boltzmann's constant,  $T$  is the temperature,  $B$  the detection bandwidth,  $A_0$  the oscillation amplitude. The bandwidth goes from zero to an upper limit in order to cut off the noise at high frequency.  $B$  is related to the spatial frequency of the sample that we want to observe. We can ideally express the topography of the sample along one line of scan as the sum of Fourier components. If we call  $\Delta x$  the minimal separation to resolve, the upper frequency to be included in the sum is  $B = \frac{1}{\Delta x} \times v_x$ , where  $v_x$  is the scan speed. Eq. (1.32) shows that the thermal noise can be decreased using resonators with a high  $Q$  factor. This can be done without modifying the bandwidth, as the two quantities are independent in FM. Similarly, eq. (1.32) shows that low temperature and high amplitudes are optimal conditions to lower thermal noise.

This noise must be summed to the one associated to the detector, which can be expressed as [6]:

$$\delta f_{det} = \frac{n}{\pi A_0} B^{3/2} \quad (1.33)$$

where  $n$  is the spectral density of the detector (assumed as constant around  $f_0$ ). The total noise is then given by:

$$\delta f = \sqrt{\delta f_{th}^2 + \delta f_{det}^2} \quad (1.34)$$

## 1.5 Force and frequency shift

In 1.3.2 I used a simple model for tip-sample forces to make several general considerations about AFM performances. However, these forces often have a more complicated dependency on the tip-sample distance. They can include electrostatic and magnetic forces, van der Waals forces, Pauli repulsion, chemical and adhesion forces. Effects of the environment such as the formation of capillary bridges when measuring in air should be taken into account. The shape and the chemical composition of both the tip and the sample influence their mutual interaction.

In Dynamic AFM the tip generally probes a sum of all these forces during each cycle of oscillation. This makes it difficult to find analytical solutions of eq. (1.2). Nevertheless, it is possible to establish a mathematical connection between forces and frequency shift. Giessibl approximated the cantilever as an weakly disturbed unidimensional harmonic oscillator, with a Hamiltonian [8]:

$$H_0 = \frac{p^2}{2m^*} + \frac{kq^2}{2} \quad (1.35)$$

where  $m^*$  is the effective mass of the lever and  $q'(t)$  the instantaneous tip position minus its average value (see fig. 1.7). In presence of a small disturbance, the cantilever motion can be assumed to still be harmonic with frequency  $f = f_0 + \Delta f$ , where:

$$\Delta f(d) = -\frac{f_0}{kA_0^2} \frac{1}{T} \int_0^T F_{ts}(q(t)) q'(t) dt \quad (1.36)$$

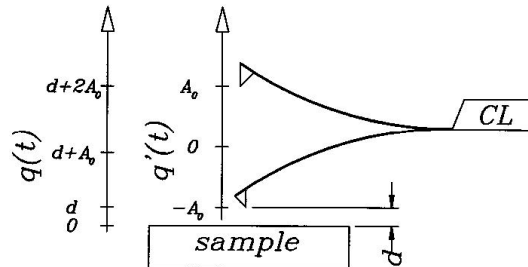


Figure 1.7: Scheme of the cantilever oscillating close to the sample [8].



Here  $q(t) = d + A_0 + q'(t)$  represents the instantaneous tip-sample separation;  $d$  is the minimal value of separation. This equation allows to predict the frequency detuning given a certain model of tip-sample interactions. Inversely, interaction forces can be calculated from frequency shift in FM AFM spectroscopy experiments. Frequency shift as a function of the tip-sample distance can be acquired over a point (x,y) of the sample surface. Sader and Jarvis [9] demonstrated that forces can be computed from frequency shift using the following equation:

$$F_{ts}(d) = \frac{2k}{f_0} \int_d^\infty \left[ \left( 1 + \frac{A_0^{1/2}}{8\sqrt{\pi(t-d)}} \right) \Delta f(t) - \frac{A_0^{3/2}}{\sqrt{2(t-d)}} \frac{d\Delta f(t)}{dt} \right] dt \quad (1.37)$$



## 2 Experimental setup

In this chapter I will describe the main components of the AFM used for the experiments presented in this thesis. In the first part I will give details of the home made AFM head, the vacuum chamber and cryostats. The entire experimental setup was largely developed by Aleksandra Radenovic and Susana Tobenas and a lot of information about it can be found in their Ph. D. theses [10, 11].

### 2.1 Home made AFM

The microscope used for the FM measurements discussed in this thesis is described in this section. It consists of a home-made AFM head shown in fig. 2.1, made from Oxygen-free high thermal conductivity (OFHC) copper. The microscope is based on an optical detection scheme, as described in section 1.2. The system uses an ultrastable temperature stabilized laser diode with incorporated fiber coupled system (OZ-2000, OZ-Optics Ltd. [13]), which has an output power tunable up to 10 mW. The typical value I used in my experiments is close to 10 mW. The solid state diode laser produces a laser light with a wavelength  $\lambda = 658$  nm. The laser source is placed outside the vacuum chamber and there is an optical fiber UHV throughput connecting the fiber coming from the laser with the one guiding the laser beam to the AFM head. The termination of the optical fiber inside the vacuum chamber is mounted in a metal holder on the AFM head, which contains a lens at its end in order to focus the light on the cantilever. The laser beam is sent to a mirror mounted on a slip-stick piezo-based (see fig. 2.1) spherical tilter. The user can adjust the angle of the mirror in order to send the laser beam on the back of the cantilever. The lens on the laser holder allows focusing the laser beam to minimize its lateral spread in the region of space where cantilevers are placed (small adjustments of the optical path are necessary each time when the cantilever is replaced by a new one). A second mirror directs the light reflected from the cantilever on the 4-quadrant detector. A slip-stick piezo-based slider allows moving the detector on a plane in order to place the laser beam at the center of the detector. Each quadrant converts the amount of light incident on it in a proportional voltage. The four quadrants are identical and adjacent squares. It can be assumed that the internal edges identify two Cartesian axes ( $x_D, y_D$ ) in the

## Chapter 2. Experimental setup

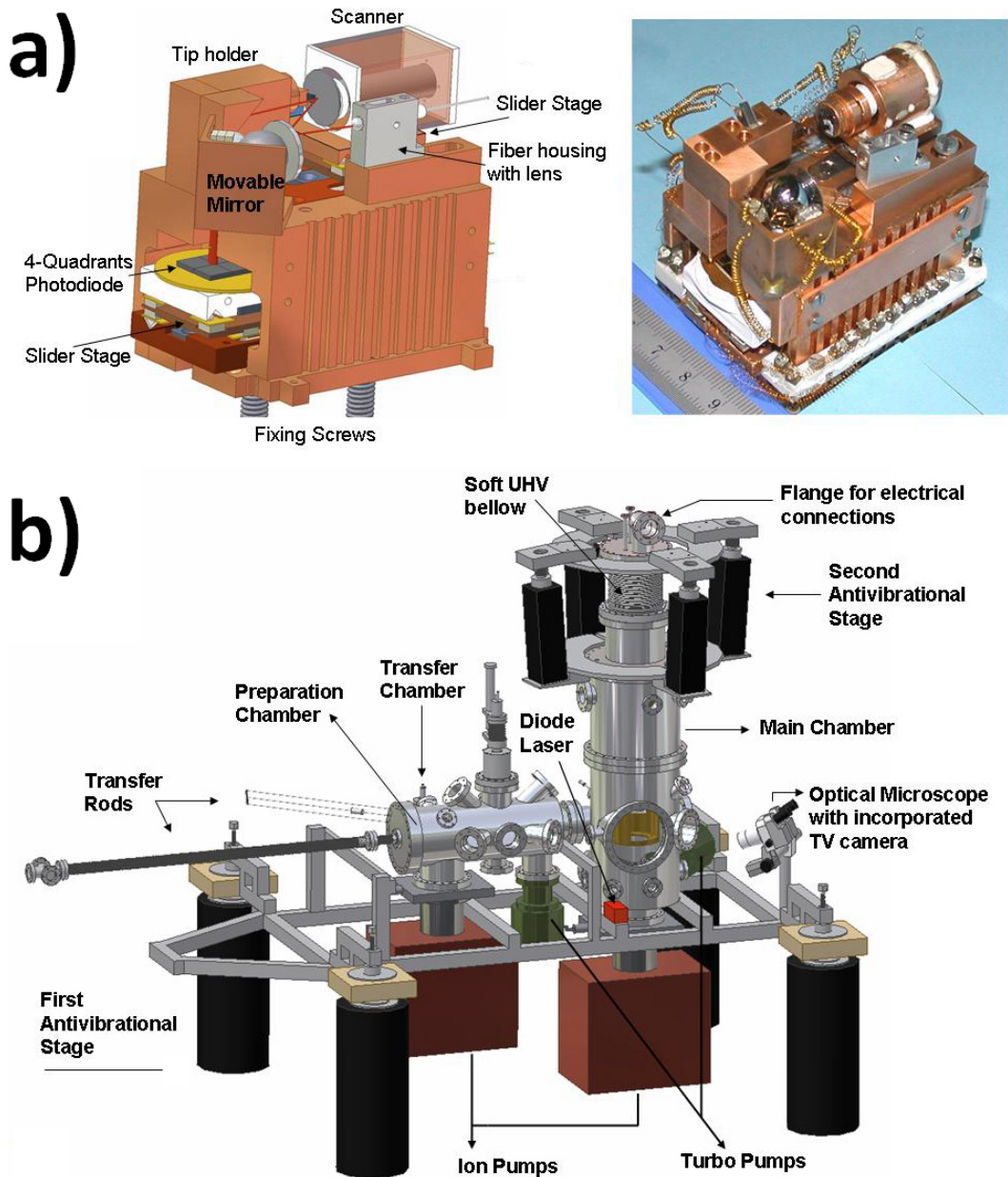


Figure 2.1: **a)** The microscope head: the image on the left summarizes its main components, while the one on the right is a real picture. **b)** Schematic representation of the vacuum chambers.

detector reference. Any deflection of the cantilever causes a displacement of the spot in this reference. The orientation of the detector is such that a deflection of the cantilever in the direction perpendicular to the sample surface traduces itself in a displacement of the spot only along  $y_D$ , while any torsion of the lever causes the movement of the spot along  $x_D$ . Signals acquired by the detector are used to calculate the total intensity of the laser spot (sum of the voltages of the four quadrants), its vertical position (the two “upper” minus the two “lower”

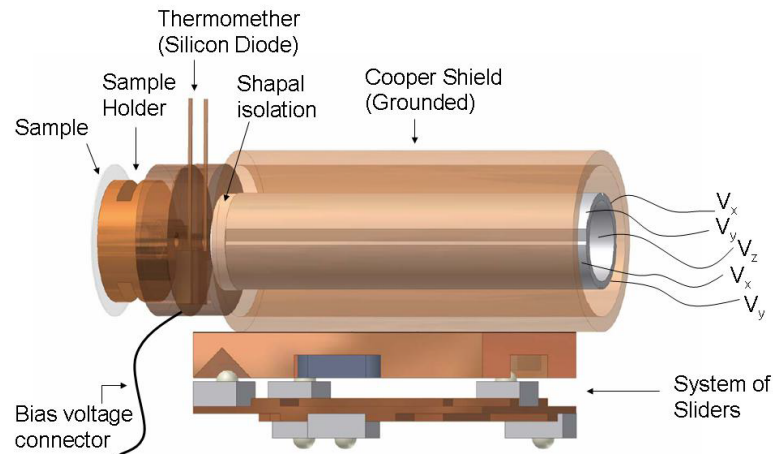


Figure 2.2: A representation of the scanner.

quadrants) and its horizontal position (the two “right” minus the two “left” quadrants).

The scanner is a quartered piezoelectrical tube and the sample is mounted on it (fig. 2.2). The application of opposite sign voltages to the opposite quadrants of the scanner causes its bending in  $x$  or  $y$  direction, while a uniform voltage applied to the four quadrants together causes an elongation or contraction in  $z$ . The voltage that can be applied in the three directions ranges from  $-150$  to  $+150$  V. The maximum scanner movement is  $\pm 3.75 \mu\text{m}$  in  $x$ ,  $\pm 4 \mu\text{m}$  in  $y$  and  $\pm 0.9 \mu\text{m}$  in  $z$ . A coarse approach to the cantilever is done using a slip-stick piezo slider onto which the scanner is mounted. The detector is mounted on a similar slider. The same slider allows moving the scanner in left/right direction, allowing to change the area of the sample to scan. A thermocouple is attached to the body of the scanner and allows measuring the temperature of the sample. It is also possible to apply a bias voltage between the tip and the sample using a bias voltage connector on the sample holder. This option is routinely used during our experiments to compensate the presence of contact electrostatic potential differences.

The operation of the sliders and of the tilter is based on the concept of slip-stick motion. A sawtooth wave voltage is applied to piezoelectrical elements. These elements deform themselves when the voltage is progressively changed, then the quick jump in the voltage makes the elements to perform a step (see fig. 2.3). Therefore, the slider movement is the sum of discrete steps, whose number is proportional to the frequency and the time of application of the sawtooth signal; the amplitude of each step is determined by the peak-to-peak voltage of the driving signal. The user can set all these parameters in order to make coarse or fine movements. The sample must be brought close to the tip before starting measurements and this is done automatically through a combination of movements of the scanner and its slider. The scanner elongates itself to explore the region of space in front of the sample. If the tip is still far (that is, the frequency shift set point is not reached) the scanner retracts and the

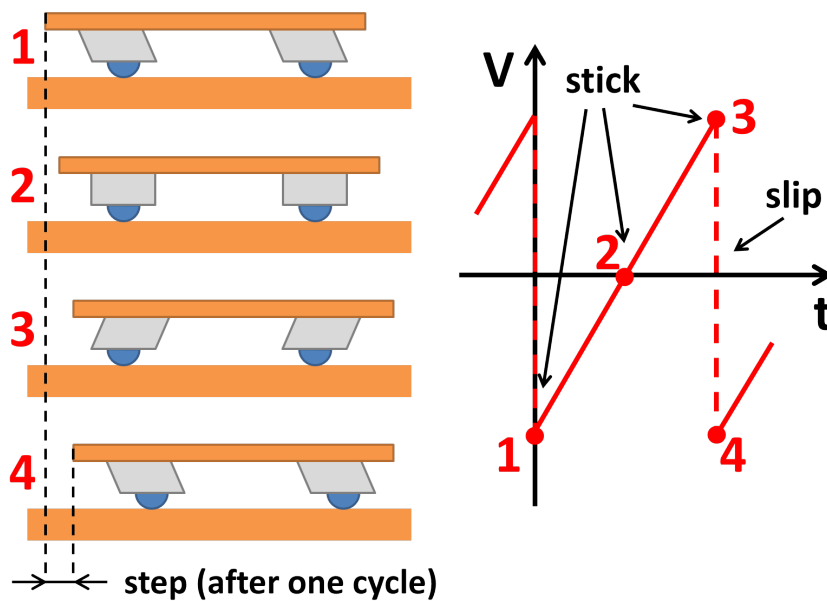


Figure 2.3: Description of one cycle of slip-stick motion. The piezoelectrical elements of the slider deform themselves linearly with the applied voltage. This allows to shift the slider from the position 1 to 3. During this period (“stick” phase) the contact point of element with the ground remains the same due to the friction. The sudden jump in the applied voltage (4) allows the elements to win the friction with the ground and to make a step, assuming again the initial configuration (“slip” phase).

slider makes an appropriate number of steps (corresponding typically to  $100\div 500$  nm, a value smaller than the z-range of the scanner which is  $1.8\ \mu\text{m}$ ) to push the scanner closer to the tip. The operation is repeated until the frequency detuning matches the set point value.

The AFM head is placed in a vacuum chamber and it is in thermal contact with a cooling system made by two coaxial cryostats (fig. 2.4). This allows varying the environmental conditions, from ambient pressure to high vacuum and from room temperature (RT) to low temperature (LT). Two chambers are constantly under vacuum, as shown in fig. 2.1 b): one (the *main* chamber) contains the microscope and the cryostats, while the second one (the *preparation* chamber) is intended for the treatment in vacuum of tips and samples. These two chambers can be separated with a valve and a mechanical rod is used to transfer tips and samples from one chamber to the other. Vacuum is achieved through the use of turbomolecular pumps put in series with rotative pumps. The lower pressure that can be reached without baking is of the order of  $10^{-9}$  mbar. When this pressure is reached, ion pumps are activated and the rotative and turbo pumps are shut down to reduce mechanical noise that could hamper AFM measurements. The AFM head is mounted at the bottom of the cooling system. The AFM head is in direct thermal contact with the inner cryostat. A layer of sapphire electrically insulates the AFM from the base on which it is lodged, but in the same time it ensures good thermal contact with cryostats. A sliding copper shield surrounds the AFM head and it can be closed

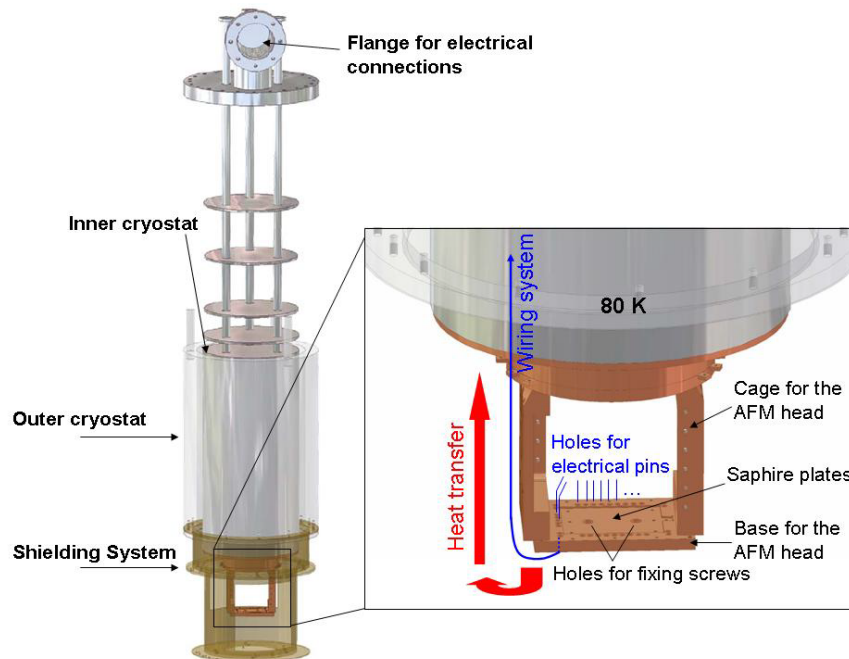


Figure 2.4: Scheme representing the cooling system, the shield and the base of the AFM head.

during measurements, providing an isolation from the external electromagnetic radiation and the thermal radiation from the room. The shield is in thermal contact with the outer cryostat (see fig. 2.4).

The microscope is cooled down filling the cryostats with liquid nitrogen or helium. If only nitrogen is used both cryostats are filled with it and the equilibrium temperature that can be reached is 82 K circa. Lower temperatures are achieved when using liquid helium; in this case, the inner cryostat is filled with liquid helium and the outer one with liquid nitrogen, which acts as a thermal screen. The system can be cooled down to 10 K circa in this case.

The microscope is decoupled from external mechanical noise using two anti vibrational stages in series, as shown in fig. 2.1 b). Each of the stages consists of four pneumatic legs from Newport Inc. [12]. The first stage (Newport I-2000 series) carries all vacuum chambers and pumps, while the second one (I-325A series) carries only the cryostats and the AFM head. The frame supporting the entire system is filled with sand in order to further damp the internal vibrations.

A fast entry chamber makes it possible to avoid breaking the vacuum each time that a new tip or sample are introduced in UHV. The fast entry chamber has a small volume ( $\sim 200 \text{ cm}^3$ ) and can be pumped from atmospheric pressure to  $10^{-7}$  mbar in 20 minutes, which then represents the typical time to introduce a new sample or tip in the UHV chamber. The cantilever chips and the samples are mounted on OFHC copper holders having magnets on their base. Up to three samples or cantilevers can be fixed on the fast entry transfer rod, which has adapted

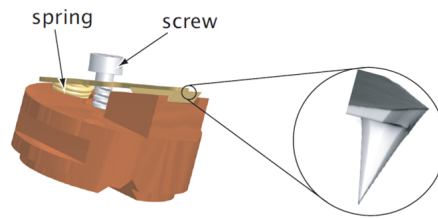


Figure 2.5: Representation of the cantilever holder. The chip is fixed through a lever screwed to the holder.

magnetic slots. Vacuum in the fast entry chamber is achieved using a turbomolecular pump in series with a membrane pump. A valve divides the fast entry chamber from the preparation chamber. A wobble stick allows moving objects from the fast entry rod to the main transfer rod, having a similar three magnetic slots. A motor moves the transfer rod between the preparation and the main chamber. In the main chamber tips and samples can be grabbed with a second wobble stick and placed on the AFM head, where they are fixed magnetically. Samples are attached to their holders using a conductive glue. The chip containing the cantilever is held by a lever tightened through a screw (fig. 2.5).

### 2.1.1 Tips

Two kinds of cantilever probes have been used for the experiments presented in this thesis: Mikromasch NSC35 [14] and Mikromasch 15 Series terminated with Diamond-Like Carbon (DLC) whiskers [15]. Properties of these probes are summarized in tab. 2.1:

Probe	$k$ (N/m)	$f_0$ (kHz)	tip radius (nm)	tip material
Mikromasch (NSC35)	4.5, 7.5, 14	150, 210, 315	$\leq 10$	Silicon
Diamond Like Carbon (DLC)	40	325	$\leq 3$	Diamond

Table 2.1: Probes and their nominal parameters.

In both cases, the cantilevers are aluminium coated on the backside. There are three cantilevers on Mikromasch NSC35 silicon chips and they have different lengths, in order to be used progressively for imaging. There is only one cantilever on the Mikromasch 15 Series chips and the DLC whiskers are grown on the original silicon tip. Mikromasch NSC35 tips have relatively larger apex radii with respect to DLC tips. I have verified that the quality of images obtained with these probes is lower, due to the tip-molecule convolution and the “doubling” effect appearing sometimes on images and caused by the apex corrugation. DLC tips produce images of better quality. Moreover, DLC tips generally present a sharp new termination even after crashing and breaking, and often also after several breakings. This fact allows to save time during measurements, because it is possible to reuse the same probe even after an evident damage to the tip, which can be noticed when a piece of the tip is seen lying on the sample surface or when a sudden modification of the shape of force curves and of the ideal value of the frequency shift feedback set point are observed. Due to the tip properties, images



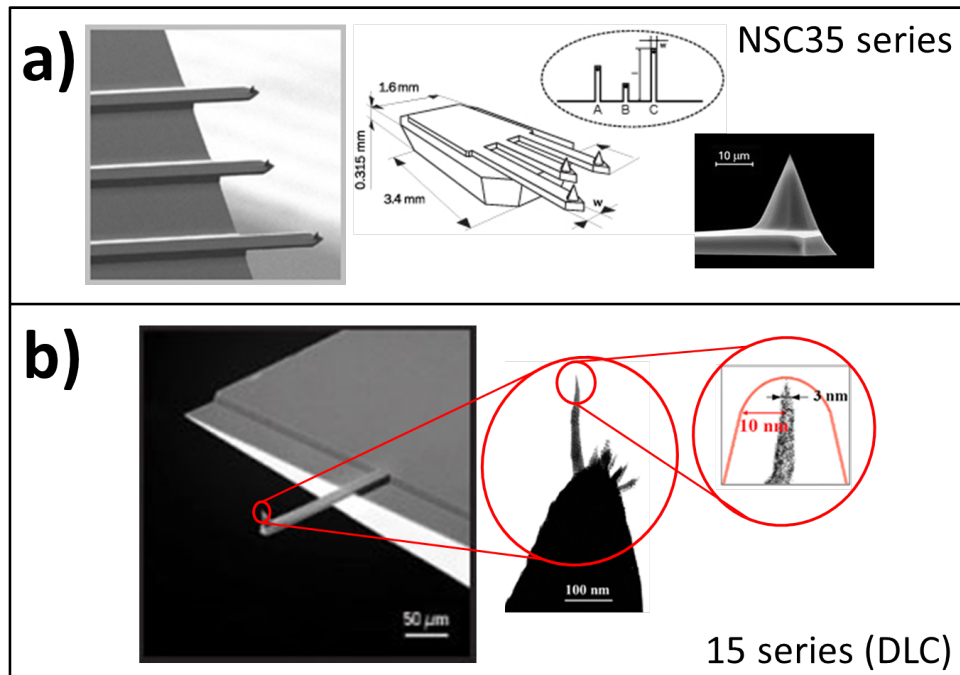


Figure 2.6: Electron microscopy images of **a)** Mikromasch NSC35 series and **b)** Mikromasch 15 Series (DLC) cantilevers and tips.

at high resolution were mostly made using DLC tips, while spectroscopy experiments and measurements of DNA height were performed both with DLC and Mikromasch NSC35 tips, in order to compare the behavior of tips with different radii.

## 2.2 Commercial electronics and software

A brief description of the electronics will be given in this section. Signals coming from the photodiodes are sent to a preamplifier which is screwed directly on an electrical connector UHV throughput on the top of the main vacuum chamber (fig. 2.7 a)). The amplified signals are processed by a device (LVS box) which outputs the sum of the laser beam intensity on the four photodiodes and the vertical/horizontal deflection of the laser spot. Both the preamplifier and the LVS box (figs. 2.7 a) and b)) have been manufactured by A.P.E. Research (Trieste, [16]). The vertical deflection signal is then sent to the Oscillation Controller (OC4, Nanonis). The OC4 basically allows communicating with an Interface Card (FPGA card NIPCI-7833R, National Instruments) which is placed in a dedicated case on the bottom of the electronics rack (see fig. 2.7). Here a Phase Locked Loop (PLL) system is used to keep the phase difference constant and to calculate the actual oscillation frequency of the cantilever. Also the oscillation amplitude can be kept fixed and equal to a certain user defined value. All the feedback gain parameters are set through the Nanonis software, as it will be shown later. The cantilever

## Chapter 2. Experimental setup

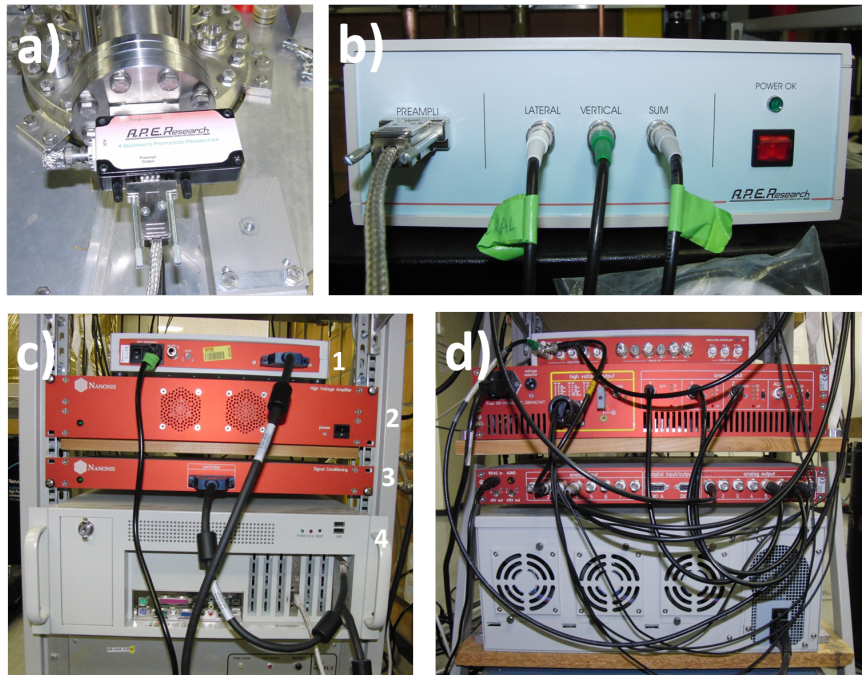


Figure 2.7: **a)** Preamplifier for signals coming from photodiodes, placed on the top of the cryostats, screwed directly on an electrical connector UHV throughput on the main vacuum chamber. **b)** The LVS box that calculates horizontal and vertical deflections and the total intensity. **c)** Front view of several elements of the electronics: Oscillation Controller (1), High Voltage Amplifier (2), Signal Conditioning (3) and case for the Interface Card (4). **d)** rear view of the same devices.

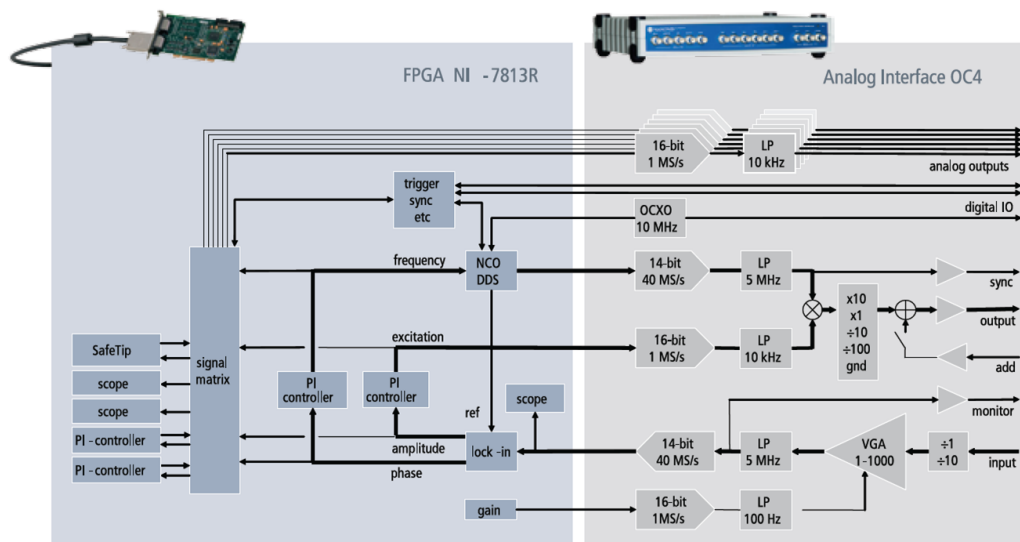


Figure 2.8: Circuitual scheme of the OC4 Controller and the FPGA card NIPCI-7833R. Readapted from [17].

excitation signal is then produced and sent out of the OC4 to the microscope. A circuitual scheme of the OC4/Interface Card system is shown in fig. 2.8.

The Signal Conditioning Box (SCCB-2, Nanonis) receives as inputs all the signals from the LVS box and communicates with the Interface Card. Main outputs of this unit are the scanner x, y and z signals and the bias voltage. The scanner driving signals are amplified through the High Voltage Amplifier box (HVAMP-220-3, Nanonis) before being sent to the scanner.

### 2.2.1 Software

The microscope is managed by means of the software released by Nanonis with the electronics and here I will list its main functions. When placing a new tip on the microscope, it is necessary to move the photodetector by means of its slider to place the laser spot in the middle of the

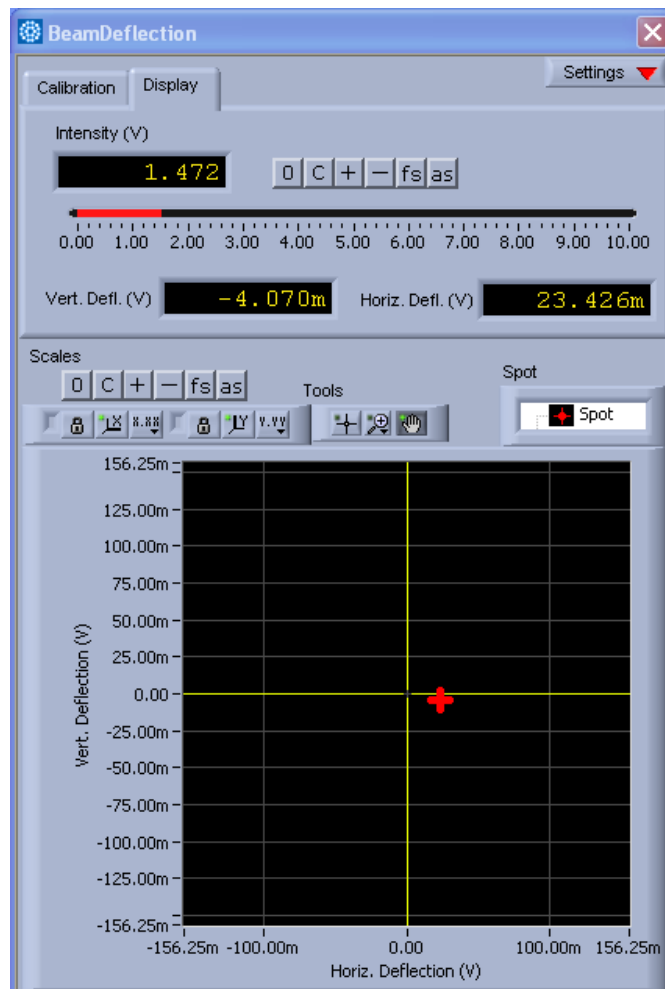


Figure 2.9: **a)** Beam Deflection window; the red cross indicates the position of laser spot on the detector.

## Chapter 2. Experimental setup

four quadrants. The Beam Deflection window displays the position of the laser spot on a Cartesian plane where the two coordinates are the horizontal and vertical deflection signals. After this operation, the new oscillator has to be characterized. For all experiments described in this thesis, the cantilever has been excited at its fundamental eigenfrequency.

The Frequency Sweep window (fig. 2.10) allows finding the resonant frequency, the Q factor and the amplitude over excitation factor. This is done exciting the lever over a range of frequencies and recording the amplitude vs. frequency and phase vs. frequency curves. These parameters are used by the software to set automatically optimal feedback gains on the amplitude and the phase. The user can modify these feedback gains through the Oscillation Control window (fig. 2.11 a)), which allows also switching on and off the two feedback systems independently. In the Oscillation Control window calibration of the cantilever deflection (measured in meters per Volts) and the oscillation amplitude can be set. I always worked at constant amplitude and so the feedback on amplitude was always used. The excitation is

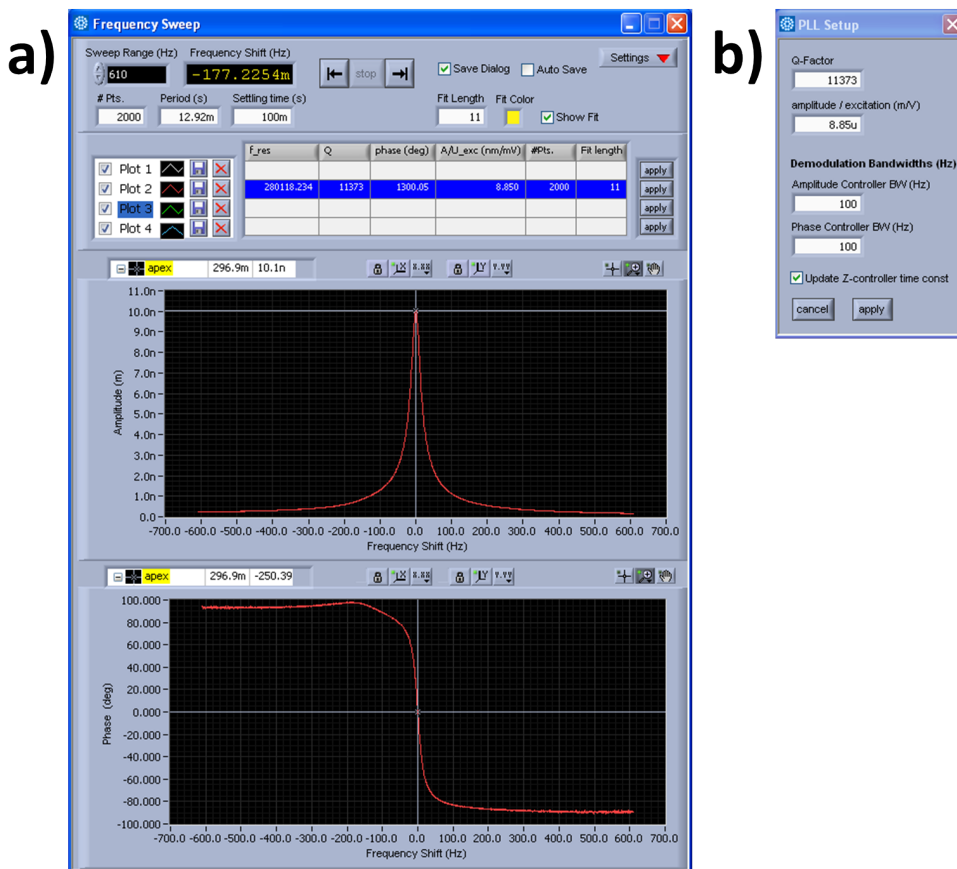


Figure 2.10: **a)** Frequency Sweep window: amplitude vs. frequency and phase vs. frequency curves can be made to find the cantilever resonance. **b)** PLL Setup window: the Q factor and the amplitude over excitation factor are automatically updated once the resonance is found through the Frequency Sweep window; amplitude and phase bandwidths can be set here.

the sinusoidal voltage signal sent to the dither piezo which is placed in the microscope body behind the cantilever holder. When the tip interacts with the sample, the excitation amplitude has to be instantaneously readapted in order to keep the cantilever oscillation amplitude constant.

After approaching the sample in the way described in section 2.1, the contact potential difference can be compensated through the CPD Compensation window (fig. 2.11 c)). The tip is placed at 100 nm circa with respect to the sample surface and frequency shift vs. bias voltage curves are measured. It is known that these curves have a parabolic behavior [18] and that the vertex of the parabola corresponds to the contact potential difference, therefore a tip-sample

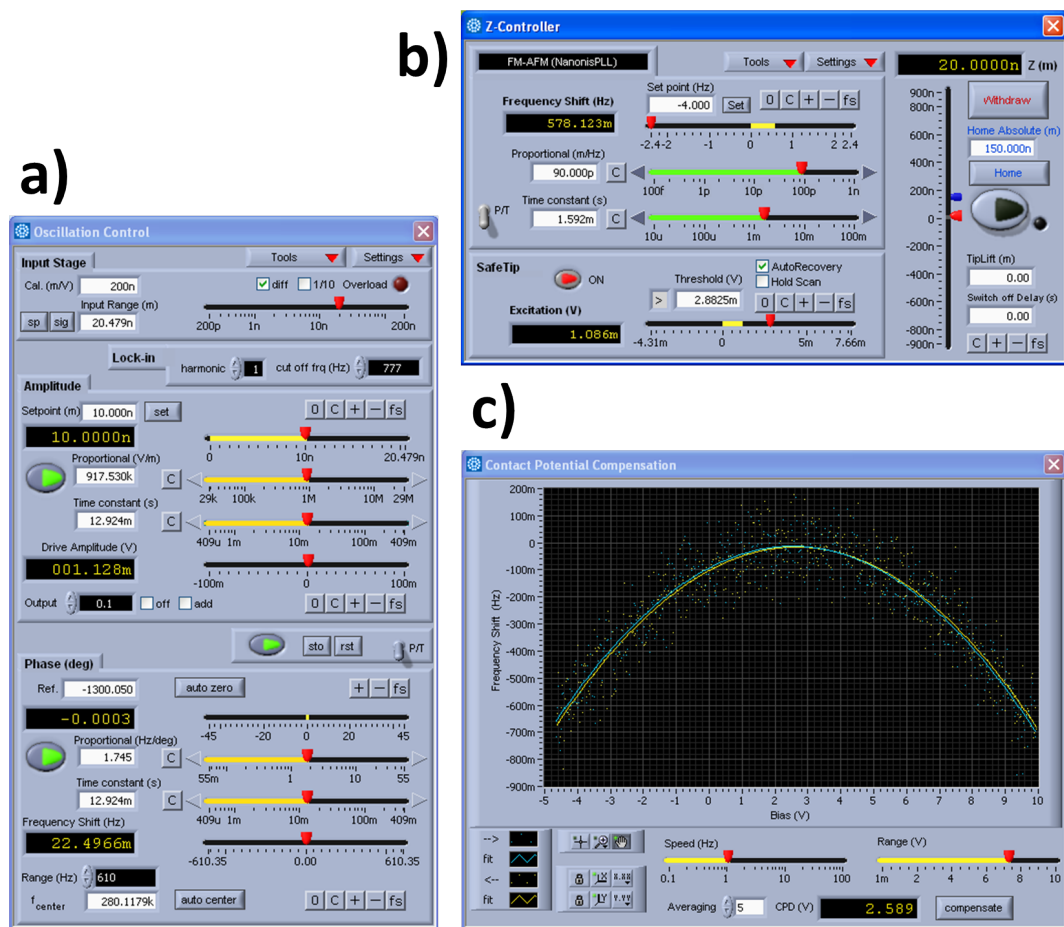


Figure 2.11: **a)** Oscillation Control window: the amplitude calibration factor can be set on the top; commands for amplitude and phase feedbacks are present in this window. **b)** Z-Controller window: the feedback mode, the set point value and the feedback gains are managed in this window; on the right, the bar indicating the tip position; on the bottom, the safe tip condition option. **c)** Contact Potential Compensation window: applying a bias voltage in a certain range (max.  $-10 \div +10$  V) it is possible to determine the contact potential difference as the apex of the frequency shift vs. bias voltage curve and to compensate it.

## Chapter 2. Experimental setup

bias voltage equal to the value of voltage at the parabola vertex is applied. This operation has been done for all measurements presented in this thesis.

The Z-Controller window (fig. 2.11 b)) allows setting the feedback variable (the frequency shift in this thesis) and feedback gains on the scanner vertical elongation. The red cursor on the vertical bar on the right of the window marks the vertical elongation of the scanner in nanometers. In this bar, the zero value represents the position at which the scanner is half elongated. The scanner mounted on the microscope can range from +900 nm (scanner completely contracted) to -900 nm (scanner completely elongated). The “Safe Tip” condition is an option of this window that allows retracting the tip to a safe position (Home position, indicated with a blue cursor on the vertical bar) when the tip-sample interaction becomes too strong, in order to prevent tip breaking. I always used the excitation as signal for this function. I set a critical value of the excitation typically at the two or three times the value of the excitation at free oscillation (order of several millivolts).

A special window has been inserted in the Nanonis software (home-written in Labview) in order to move all the slip-stick sliders (fig. 2.12). A home made generator produces the high

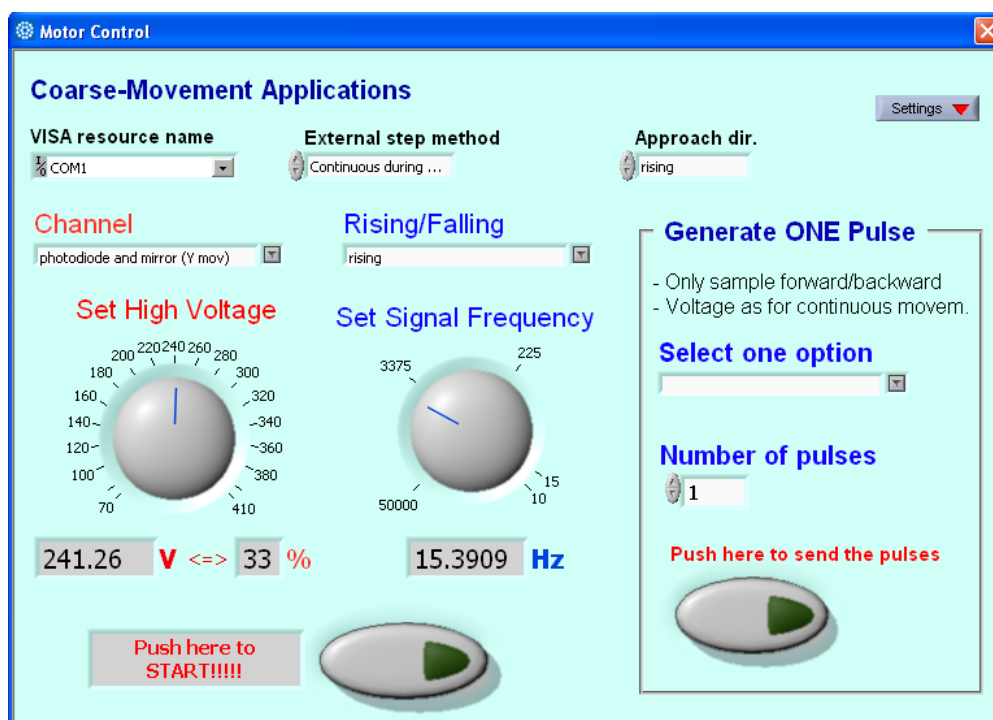


Figure 2.12: The Motor Control window allows moving all the sliders on the AFM head. The voltage and the frequency of the sawtooth signal sent to the sliders can be set here. The slider to activate is chosen through the Channel menu, while the direction of movement is selected in the Rising/Falling menu. The panel on the right of this window allows making a determined number of steps to the selected slider; this option is mainly used to precisely adjust the position of the sample in close proximity to the tip.

voltage sawtooth signals which are sent to the microscope to perform these movements [11].

### 2.2.2 Amplitude calibration

A periodic electric signal is produced by the detector when the cantilever oscillates. This signal is converted in nanometers of oscillation amplitude by means of an appropriate calibration factor. Here I will describe the method I use to evaluate the calibration factor. First of all the tip is placed close to the sample, at a range of distances where an appreciable frequency shift is observed (typically, at the same value of frequency shift used as set point). The amplitude set value that I use is generally  $A_0 = 10$  nm. If the frequency shift is left unchanged but the amplitude is suddenly reduced to 9 nm, a consequent jump in the  $z$  (scanner vertical elongation) signal is seen, due to the fact that the scanner has to approach the sample covering a distance proportional to the amplitude change. The amount of this jump depends on an ensemble of parameters. To simulate this event, I built a model of the tip-sample interaction. The tip is modeled by a sphere representing its apex, while the sample is assumed to be a medium filling half of the space and bound by a flat surface. Both the tip and the sample are homogeneous and they interact only through van der Waals forces. In this case, the potential energy is given by [19]:

$$U(s) = -\frac{A_H}{6} \left[ \frac{r}{s} + \frac{r}{2r+s} + \ln\left(\frac{s}{2r+s}\right) \right] \quad (2.1)$$

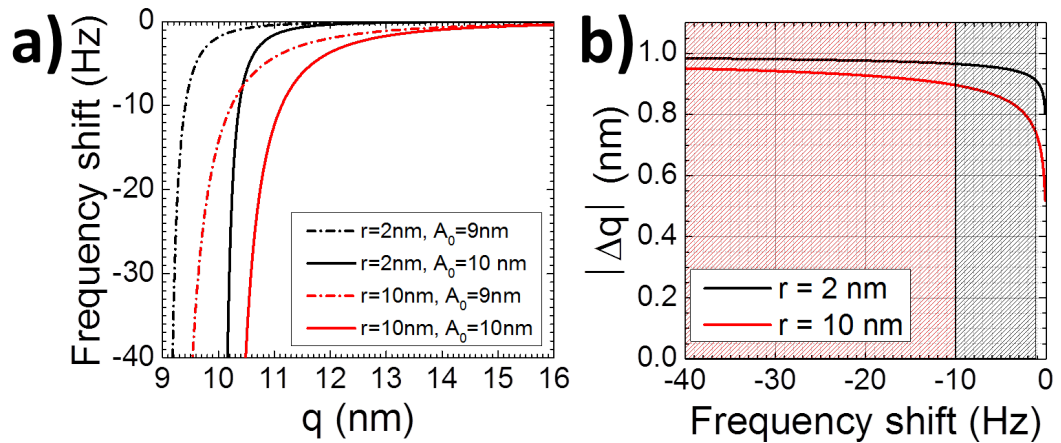


Figure 2.13: **a)** Frequency shift vs. separation curves at different tip radii (2 and 10 nm) and oscillation amplitudes (9 and 10 nm). **b)** The expected jump in the vertical position of the scanner when the amplitude changes from 10 to 9 nm, for each of the two tip radii, as a function of the frequency shift; the black area represents the typical range of frequency shift set points I used in experiments in this thesis with very sharp 2 nm radius DLC tips, while the red area the typical values at larger tip radii of approximately 10 nm of Mikromasch tips.

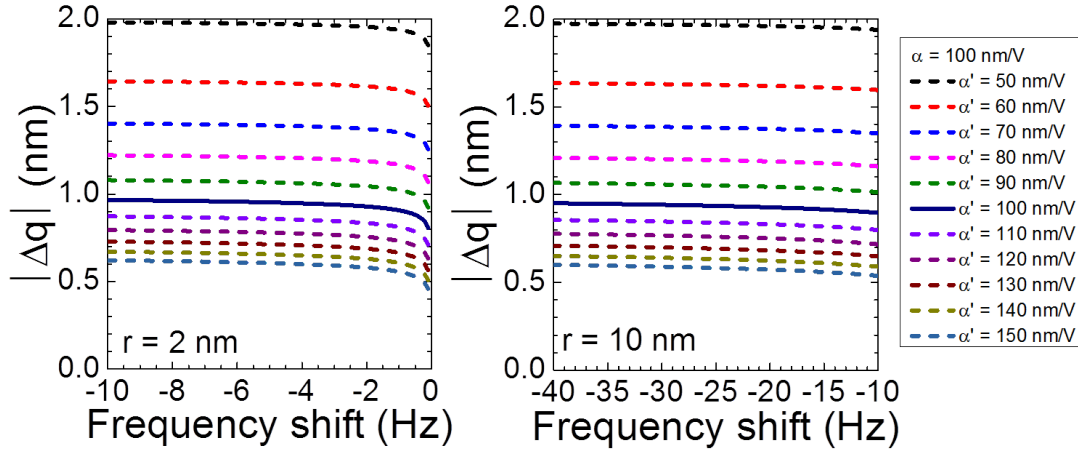


Figure 2.14: Expected jump in the vertical position of the scanner when the amplitude changes from 10 to 9 nm, for each of the two tip radii and at different calibrations, as a function of the frequency shift. The correct calibration is supposed to be  $\alpha = 100$  nm/V.

where  $s$  represents the separation between the bottom of the sphere and the surface,  $A_H$  is the Hamaker constant and  $r$  is the radius of the sphere. Tip-sample force is calculated deriving the potential energy, that is  $F(s) = -\partial_s U(s)$ , and then eq. 1.36 allows obtaining the frequency shift  $\Delta f(d)$  as a function of the minimal separation  $d$  during one oscillation cycle. Using the same notation as in fig. 1.7, the variable  $q = d + A_0$  can be defined. Plotting  $\Delta f(q)$  curves for  $A_0 = 10$  and 9 nm, it is possible to calculate the difference  $\Delta q$  between the positions in which the given  $\Delta f$  value is reached in the two curves. It is easy to verify that  $\Delta q$  corresponds in absolute value to the jump  $\Delta z$  made by the scanner in the real experiment, when the amplitude is reduced from 10 to 9 nm leaving the same  $\Delta f$  value. Calculations have been done supposing to have a sharp DLC tip ( $r = 2$  nm) and a larger Mikromasch tip ( $r = 10$  nm). The Hamaker constant  $A_H$  has been fixed to  $10^{-19}$  J, which is its typical order of magnitude. The resonant frequency and the spring constant have been set to  $f_0 = 325$  kHz and  $k = 40$  N/m respectively, simulating the standard values for the above-mentioned cantilevers I used. In fig. 2.13 a)  $\Delta f(q)$  curves obtained with the two radii at  $A_0 = 9$  and 10 nm are plotted. Fig. 2.13 b) shows the expected jump in  $z$  of the scanner. Particularly, the usual ranges of the frequency shift for sharp (black area) and large (red area) tips are displayed, showing that the jump is near to 1 nm in both cases.

The value  $|\Delta q|$  depends on a series of parameters, such as the  $\Delta f$  value, the two values of  $A_0$ , the radius of the tip and the amplitude calibration  $\alpha$ . If the calibration is correct, the electric signal  $V_A$  produced by the detector is exactly transformed in the desired value of oscillation amplitude  $A_0$  and the relation  $A_0 = \alpha V_A$  holds. If the calibration is wrong, the amplitude feedback excites the cantilever with a different intensity leading the detector to produce a signal  $V_A' = \frac{A_0}{\alpha'}$ , where the incorrect calibration have been indicated with  $\alpha'$ . Therefore, the real oscillation amplitude is  $A_{real} = \alpha V_A' = \frac{\alpha}{\alpha'} A_0$ . In fig. 2.14 I plotted calculated  $|\Delta q|$  vs.  $\Delta f$



at different calibrations  $\alpha'$ .

The conclusion is that the correct cantilever amplitude calibration can be found in a quite accurate way by changing the calibration factor until a  $z$  jump of circa 1 nm is observed, when all the other parameters are coherent with the previous calculations. The main advantage of this method is its simplicity, which allows an immediate check of the calibration also in presence of a significant vertical drift of the scanner. Obviously, this method relies on the fact that the scanner is precisely calibrated. I regularly checked the scanner  $z$ -calibration using single atomic steps on HOPG graphite surfaces.

A most accurate method is based on the fact that  $\Delta f(d) = A_0^{-3/2}g(d)$  as stated in [8], where  $g(d)$  represents a specific function of the separation  $d$  independent from  $A_0$ . Therefore, when changing the amplitude from  $A_1$  to  $A_2$ , it is easy to find that the new value of the frequency shift at the separation  $d$  is  $\Delta f_2(d) = \left(\frac{A_2}{A_1}\right)^{3/2} \Delta f_1(d)$ . When changing the amplitude, if also the frequency shift is modified according to this relation, as a result the minimal tip-sample separation remains constant and the difference  $|\Delta q|$  must correspond to the amplitude variation. This check allows to see if the amplitude calibration is correct. However, given the calculations that I performed and showed in this paragraph, the error on the calibration using our slightly simpler method is sufficiently small considering also all the other possible sources of noise.



## 3 Revealing the sub-molecular structure of DNA

In this chapter I will give a brief introduction about some of DNA properties and discuss the DNA importance not only in biology, but also for applications in nanotechnology, underscoring the importance of studying DNA also in non-physiological environments. I will show FM AFM measurements on DNA, demonstrating the ability of this technique to obtain images with sub-molecular resolution. I will discuss different FM AFM-based approaches to reveal DNA structure. One consists of performing a series of spectroscopy curves along the molecular axis, in order to correlate the variation of forces with the underlying structure. The second is based on the acquisition of data scanning the sample at constant height, that is with the feedback on the vertical position of the scanner switched off. This method allows obtaining frequency shift maps on the top of the molecules that show a better level of lateral resolution than the classical FM AFM scanning. The periodicity of the observed features, that range from 3 to 5 nm, as well as calculations of van der Waals AFM tip-DNA interactions, indicate that the features correspond to DNA helix grooves. To my knowledge this is the first time an AFM has successfully revealed the structure of dehydrated DNA, which is significant for DNA nanotechnology use.

### 3.1 DNA and its polymorphisms

DNA stands for Deoxyribonucleic Acid and it is a fundamental molecule for all living organisms. DNA consists of a double helix in which a core and two backbones can be distinguished. The core is made of four organic molecules called nucleobases, which are adenine (A), guanine (G), cytosine (C) and thymine (T). Nucleobases are coupled along the DNA molecular axis, giving origin to the so called base pairs. The pairing is well determined, in the sense that only AT and CG base pairs can be found in a stable DNA structure. This is due to the number of hydrogen bonds that the single nucleobase can form, that is two hydrogen bonds for the AT pair and three for the CG pair. Uracil (U) substitutes thymine in ribonucleic acid (RNA).

The base pairs are sustained by two backbones which are placed in the outer part of the

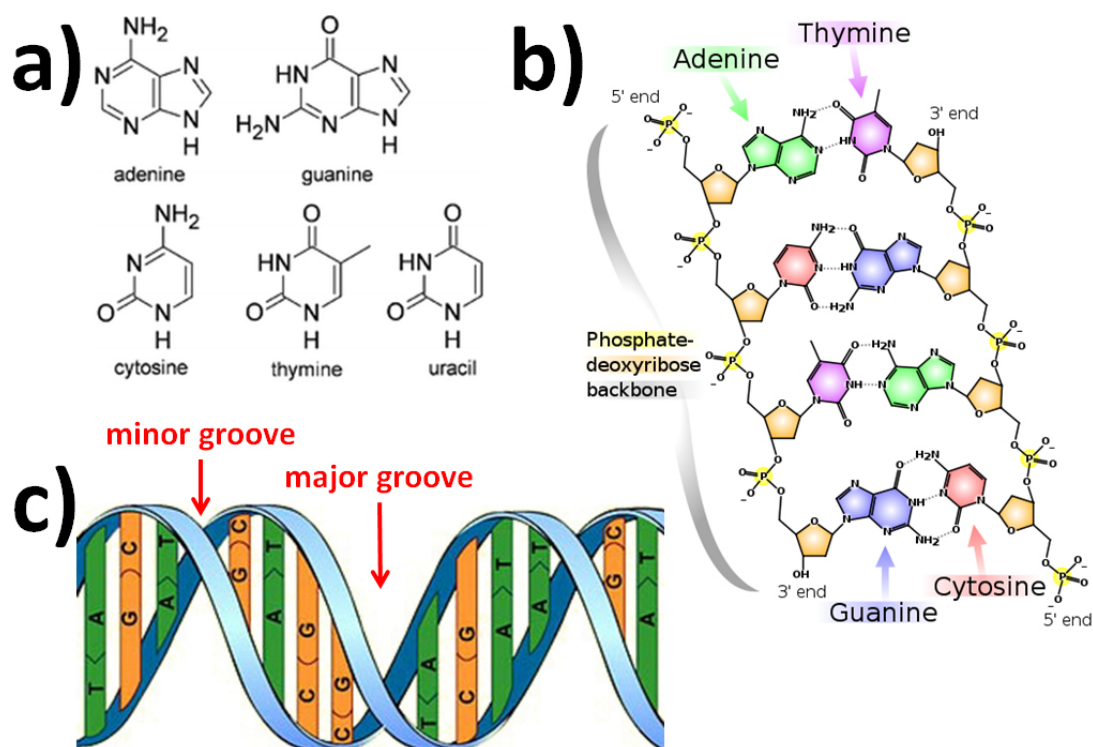


Figure 3.1: **a)** Representations of the nucleobases [20]. **b)** A sketch representing the coupling of the nucleobases (with the number of hydrogen bonds for each base pair) and the two backbones containing phosphate groups and deoxyribose sugars [21]. **c)** A schematic view of the DNA double helix, showing major and minor DNA grooves [22].

molecule. Each backbone is made by a chain in which deoxyribose sugars and phosphate groups alternate. Each nucleobase is linked to one deoxyribose and this complex is called nucleoside. The phosphate group bridges two consecutive nucleosides. The stable DNA configuration is a consequence of the interplay of several factors, which are not only the interactions of DNA components in the core and along the backbones but also the environmental conditions in which the molecule is placed. Taking all the factors into account, DNA generally assumes a double helical conformation, where the two helices are represented by the two backbones. This means that the base pairs rotate along the molecular axis. As it will be pointed out later, several possible double helical DNA forms have been found. Due to the complexity of the structure, it is common that the two helices have a relative shift along the molecular axis. As a consequence, the space between the backbones is alternatively wider and narrower, allowing to distinguish among major and minor DNA grooves.

From a historical point of view, the determination of the DNA structure has been achieved at the beginning of 1950's through X-Ray diffraction studies on DNA fibers and their theoretical interpretation. Decisive measurements were performed by Franklin and Gosling on calf thymus DNA at different humidities, finding separate diffraction patterns for the dry and wet fibers, to which they referred as A-form and B-form DNA. As it is well known, Watson and Crick developed their double helical model of DNA after observing the diffraction photography of the B-form and submitted their work in the famous Nature article [23] in 1953, before Franklin

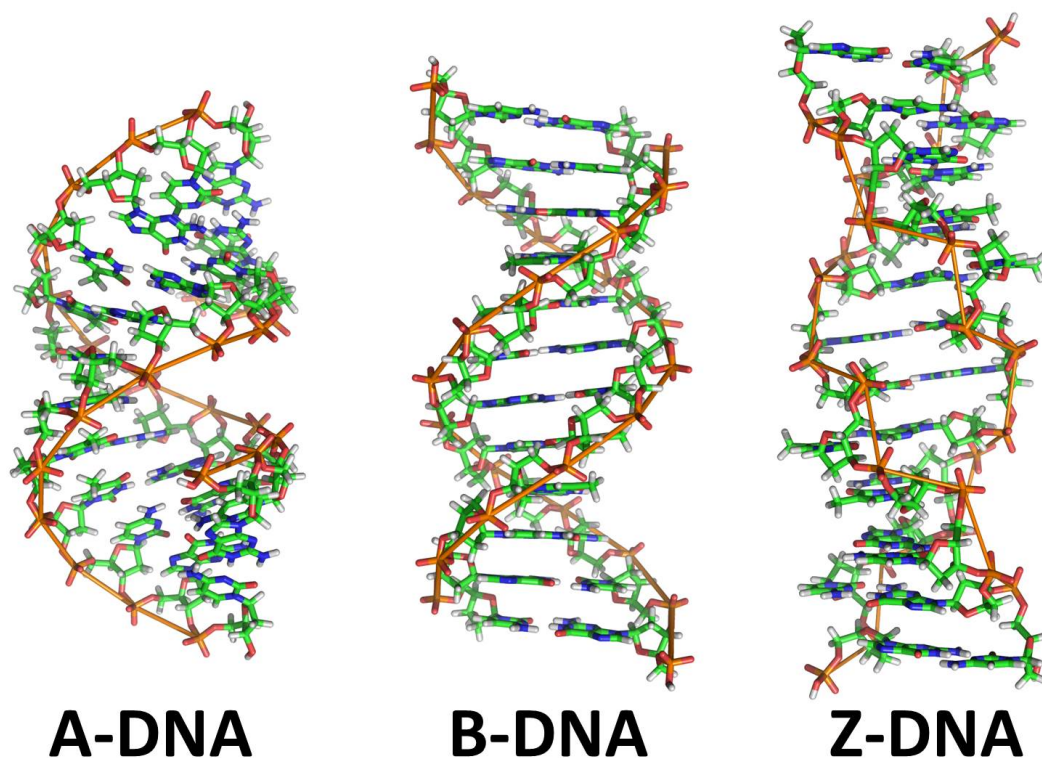


Figure 3.2: Representation of the A, B and Z forms of DNA [29].

and coworkers were able to reach any conclusions concerning the DNA structure. In the same issue, Watson and Crick published a second article concerning the possible implications of the DNA structure on its mechanism of replication [24]. Experimental results by Franklin and Gosling on the A and B-form DNA were published in the same year [25, 26].

Table 3.1: Main structural parameters for A, B and Z-DNA [30].

	A-DNA	B-DNA	Z-DNA
chirality	right-handed	right-handed	left-handed
base pairs per turn	10.7	10	12
rise per base pair (Å)	2.3	3.32	3.8
helix pitch (Å)	24.6	33.2	45.6

It was already clear from these seminal studies that DNA structure is not unique but it depends on several environmental parameters, a property which makes DNA a polymorphic molecule. Until now circa thirty different polymorphisms have been found [27]. The relative humidity, the composition of the solution in which DNA is and also the DNA base pairs content play a fundamental role in determining the final DNA form. Among them, the so-called A, B and Z forms have been recognized as the configurations which are relevant in biology. B-DNA is supposed to be the most probable form in which the DNA is present in living organisms, while A-DNA represents the configuration obtained from B-DNA when dehydrated. Both

## Chapter 3. Revealing the sub-molecular structure of DNA

of these forms are right-handed double helices, while interestingly Z-DNA appears to be left-handed. The biological role of Z-DNA is still under discussion, but it seems that this configuration facilitates the binding of certain classes of proteins to DNA [28]. The main structural parameters for these three DNA forms are listed in tab. 3.1. The diameter of DNA is reported to range between 18 and 23 Å, with the B-DNA diameter being circa 2 nm [31].

### 3.2 DNA in biology and DNA in nanotechnology

DNA encodes the fundamental information for the life of a cell and of an organism in general. The code consists of the arrangement of the nucleobases on sections along the two DNA strands, called genes. A mechanism involving several enzymes allows copying this information and transmitting it to produce proteins. Basically, the two DNA strands are unwinded and separated by helicase enzymes; the RNA polymerase enzyme then couples the exposed nucleobases with complementary bases and link the latter with a ribose-phosphate chain, forming the RNA. As pointed out in section 3.1, in RNA thymine is substituted by uracil.

DNA replication, which is necessary during the cell division, occurs in a similar fashion as

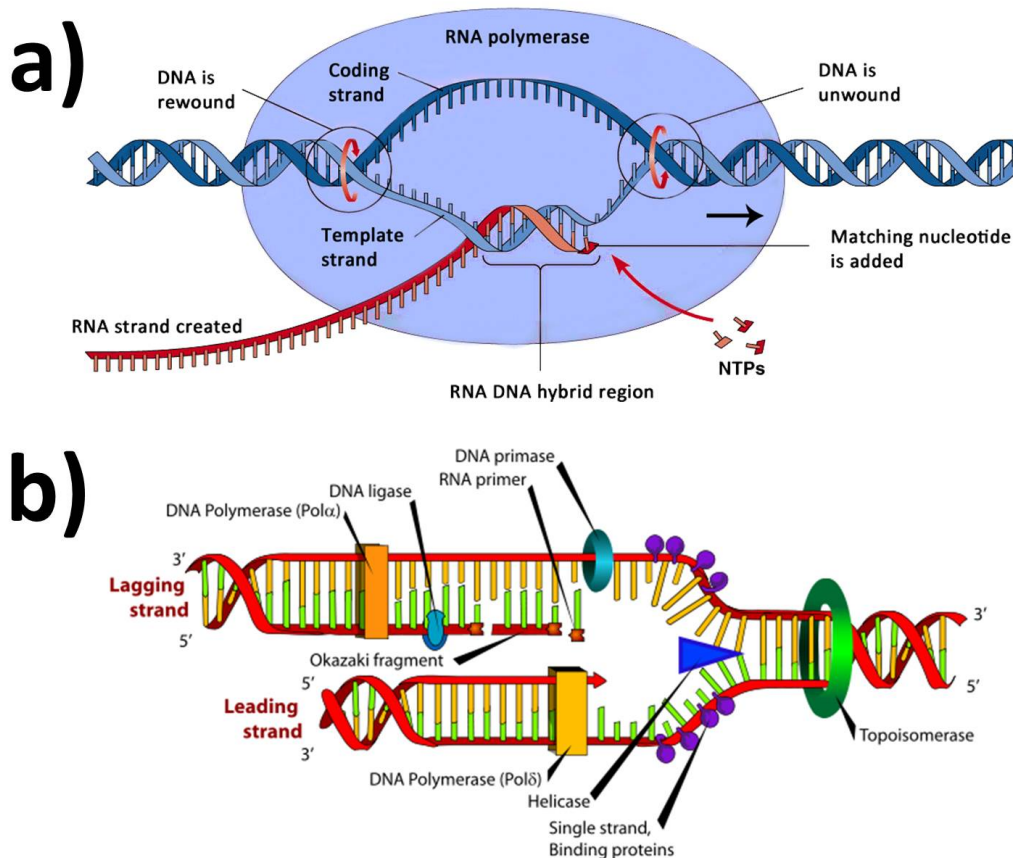


Figure 3.3: Sketches of the **a)** DNA transcription [32] and **b)** DNA replication [33].

transcription. It is known that not all the DNA sequence encodes genetical information and just a few percent actually accomplishes this task. It has been calculated that 98% of human genome is made by noncoding DNA [34]. Among this large percentage, sequences preceding and following a gene act as markers to initiate and stop the transcription. Some biological roles of the remaining DNA have been studied but this subject is still under discussion. Without entering into the details of this complex debate, it is evident that the double helical DNA structure is a way to minimize the volume occupied by the code inside the cell and to protect it from information loss.

In recent years DNA is creating more and more interest for applications in fields of research not necessarily connected to biology. Part of this interest is due to its self-assembling properties and to the possibility of forming a wide variety of both 2D and 3D nanostructures [35, 36]. One interesting application is the so-called DNA origami. It consists of a structure in which a long single DNA strand is bound to several short single stranded segments which are used to “staple” it in a chosen shape. The nucleobase content of each short strand is carefully chosen in order to match the longer strand in specific positions and to force the whole structure to fold in a desired 2D shape. Rothemund [37] was the first to develop this concept, elaborating the method for creating DNA octahedrons introduced in the Joyce’s group [38]. Several possible applications have been reported [39]. DNA origami has been used for the detection of single molecules such as RNA [40], to study bond formation and cleavage between DNA and biomolecules [41] or as a template for protein [42] and carbon nanotube [43] assembly. Moreover, the capacity of energy transfer through fluorophores arranged on a DNA origami structure has been demonstrated [44].

A considerable amount of literature has been published concerning the DNA conduction properties. It is supposed that a charge can move along DNA through a hopping mechanism between G sites and consequently the distance between them, and in general the DNA sequence, influence the charge transfer rate [45]. The importance not only of the base content, but also of the DNA structure has been pointed out in [46]. Conductivity measurements on double-stranded poly(G)-poly(C) DNA molecules were performed, showing the presence of a band gap in the current-voltage curves and allowing to state a semiconductor behavior of DNA [47]. Interestingly, the same measurements made in vacuum showed similar results and this can be taken as a confirmation that the charge transfer takes place along the DNA molecule and it is not mediated by the water surrounding molecules in liquid environment. However, different studies affirmed that the DNA has conductive [48, 49] or insulating [50] behavior. Kasumov and coauthors [51] also reported superconductive properties of DNA at low temperature. The variety of observed behaviors can be related to the sample preparation, including the possible substrate mediated conduction, and to the working environment. On the other hand, the question of the actual DNA conformation in these studies have never been addressed with sufficient specificity, due among other things to the difficulty of obtaining highly resolved information about DNA structure. As an example, a recent publication shows a theoretical conductivity dependence on DNA stretching [52].

This brief review shows how DNA can be used as a versatile building block for applications in various fields of nanotechnology. Some of its possible uses will most likely to be implemented in non-physiological environments. Therefore it becomes obvious that DNA structure has to be somehow assessed in non-physiological environments such as air or UHV. Moreover,

it is clear that DNA properties for applications in nanoelectronics crucially depend on the conformation that DNA assumes in the working environment. The measurements presented here are meant to be a characterization of the DNA structure once it is firmly attached to a substrate and put in a highly dehydrated environment.

### 3.3 AFM imaging of DNA

AFM has been used to image single DNA molecules for several purposes, which include the study of DNA topology and the observation of the interaction of DNA with proteins and enzymes. However, high resolution imaging of DNA at sub molecular level has always been a difficult task. First positive results were obtained in 1995. DNA deposited on mica was imaged in propanol by Hansma's group [53] with AM AFM, obtaining the best resolved DNA images ever made at that time. DNA in propanol was earlier found in the B form through measurements of the molecule contour length [54], although according to the same authors the most probable conformation in alcohols should have been the A form with a smaller helix pitch (2.5 nm circa). Also, the periodicity along DNA is reported to be similar to the B-DNA value, but an evaluation of the observed pitch is missing from the article. In the same year, B-DNA double helix periodicity (3.4 nm circa) was observed in closely packed DNA molecules [55]. They used a substrate of mica covered with a cationic lipid bilayer. DNA was imaged in a buffer containing ethylenediaminetetraacetic acid (EDTA) in contact mode AFM. Here, a statistical analysis of the DNA pitch showed a pronounced peak at 3.4 nm, which nicely corresponds to the B-DNA value. Authors also asserted that the right handedness of B-DNA and sometimes minor DNA grooves were visible in these measurements.

After these results, resolving DNA at sub molecular scale with AFM did not seem to be a fundamental subject of interest for a long time, if we take into account the scarce literature on the issue. This fact can be explained by several reasons. First, there is an intrinsic difficulty in imaging DNA at such a small scale with AFM. Second, the great majority of the structural information that we have on DNA has been already obtained through spectroscopic techniques, such as X-Ray diffraction or Nuclear Magnetic Resonance [27].

Only recently a renewed interest in this subject arose. In particular, two works have to be considered as fundamental progresses. Hoogenboom et al. [56] studied DNA plasmids in aqueous solution using a technique similar to FM AFM, in which the phase is tracked instead of the frequency; this is motivated by the fact that the frequency shift in liquid is smaller if compared to the width of the resonance peak. They used small cantilevers to decrease noise, which were photothermally activated. Moreover they used an interferometric detection system instead of the classical one. They observed both right and left handed DNA segments along the same plasmid, showing in some points a corrugation that can be interpreted as a sequence of major and minor grooves. Even more detailed images were obtained in Yamada's group [57]. In this case FM AFM imaging was performed on DNA plasmids, kept in aqueous solution. In this case, the fact of maintaining the oscillation amplitude to values similar to the typical decay length of the interaction forces has been recognized as a fundamental technical advantage, as suggested in [6]. In addition to major and minor grooves, a corrugation which recalls the position of phosphate groups is visible in their images. The observation is in agreement with simple simulations of the DNA imaging made by the same authors.



The results discussed until now have all been obtained in liquid. To my knowledge, no convincing and meaningful sub molecular double stranded DNA images were ever acquired in dehydrated environment.

### 3.4 DNA imaging in vacuum

In this section I will present images of DNA molecules deposited onto flat solid surfaces and studied using the AFM microscope in my experiments. Methods of deposition are based on the fact that the DNA backbone is negatively charged in water, with a charge of  $-e$  for each phosphate group. Mica is a mineral that is easy to cleave leading to surfaces flat at sub-nanometer scale. When the cleaved surface is covered by water, the surface releases ions and becomes negatively charged. To deposit DNA on mica, a certain percentage of  $\text{MgCl}_2$  is added to the DNA solution in order to obtain  $\text{Mg}^{2+}$  ions. These ions bridge the negative charge of both the molecules and of the surface and thus mediate the DNA deposition. Another commonly used way to deposit DNA is to functionalize the mica surface with a layer of (3-Aminopropyl)triethoxysilane (APTES) molecules [58]. When an APTES solution is deposited over the mica cleaved surface, these molecules attach to mica through a silanization process, while the amino group on the other side of the molecule becomes positively charged. These two methods of DNA deposition are the most common ones but both lead to a relatively rough surface with approximately 0.1 to 0.3 nm tall bumps on the substrate.

However, there is an important difference between the two methods.  $\text{Mg}^{2+}$  ions force the molecules to stick on the mica surface, but at the common concentrations the interaction is relatively weaker and allows molecules to relax on the surface, that is to further readapt their topology. On the contrary, deposition with APTES binds DNA strongly and can be considered as the projection of the DNA polymers from 3D (solution) to 2D (surface): once that the molecule is in contact with the APTES/mica substrate, the interaction is strong enough to avoid any relaxation.

In both cases, DNA molecules deposited with the two methods and measured in aqueous solution or in air have been reported to have a contour length compatible with the B-DNA length. In order to characterize the behavior of DNA molecules in vacuum, I prepared DNA

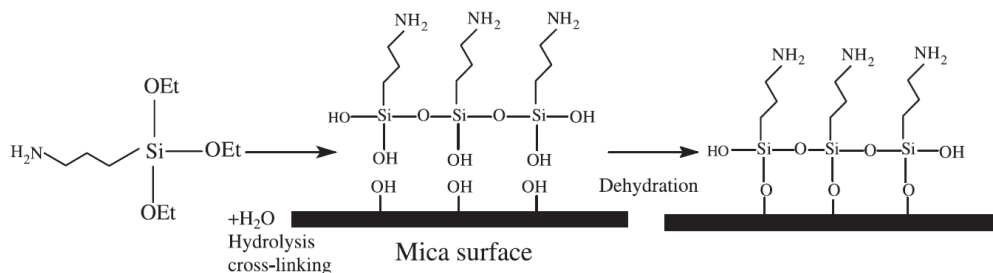


Figure 3.4: A sketch representing the water mediated silanization of the mica surface and the formation of an APTES monolayer (adapted from [59]). The process schematized here is the theoretical one, while the actual APTES deposition is supposed to be less regular [60], leading to an intrinsic surface roughness as the one observed in my measurements.

samples using both methods.

### 3.4.1 $Mg^{2+}$ and APTES deposition protocols

Here, the protocols to deposit DNA using  $Mg^{2+}$  ions or APTES are described. The two methods allow obtaining roughly the same DNA molecule density per unit of mica surface.

The DNA solution prepared for  $Mg^{2+}$  deposition is typically a 10  $\mu$ L droplet containing 1  $\div$  5 ng/ $\mu$ L of dsDNA, 2 mM of  $Mg^{2+}$  and buffer solution, used to reproduce physiological conditions. The buffer solution contains 1 mM Tris, 4  $\div$  5 mM of  $MgCl_2$  and has a pH equal to 7.5  $\div$  7.8. A disk of mica (bought from Ted Pella Inc., with diameter of 10 or 12 mm) is attached on the sample holder with conductive glue. The surface is cleaned cleaving the upper mica layers by means of scotch-tape. A droplet of solution with a volume of 10  $\mu$ L is deposited on freshly cleaved mica just few seconds after cleavage, to prevent the contamination of the charged surface from the atmosphere. The deposition time is 5 minutes circa and during deposition the sample is kept in a covered Petri dish to avoid contamination. Then the deposition is stopped by rinsing the surface three times with 1 mL of ultrapure (18 M $\Omega$ -cm resistivity at room temperature) water and gently drying the sample with a compressed nitrogen flow. The amount of DNA or  $Mg^{2+}$  and the deposition time can be slightly changed to increase or decrease the density of DNA molecules over the surface.

The deposition with APTES follows a similar protocol, but the mica surface is functionalized with APTES prior to DNA deposition. To do this, a freshly prepared APTES solution with a concentration of 0.05  $\div$  0.1% of volume is used. At this concentration, due to the amount of water, APTES molecules tend to polymerize strongly increasing the sample roughness once deposited on mica. As a rule, an APTES solution at low concentration is only used during the same day when it is prepared. Pure APTES (99%) is purchased from Sigma-Aldrich (Switzerland). 10  $\mu$ L of APTES solution are deposited on freshly cleaved mica for one minute, rinsed three times with 1 mL of ultrapure water and dried as already described. The DNA solution used in this case does not contain the extra amount of  $Mg^{2+}$  ions. As before, a 10  $\mu$ L droplet of DNA solution is deposited on the APTES/mica for a shorter time which is 1 minute circa. The time is shortened with respect to  $Mg^{2+}$  deposition due to the stronger interaction of DNA with APTES and the consequent overcrowding of the surface if longer time is used. The sample is again rinsed and dried according to the previously described procedure. For both methods, the sample quality is often rapidly checked in air using a Nanoscope III AFM microscope and then the sample is introduced in vacuum after several minutes at the most.

### 3.4.2 Statistical analysis of DNA

Double stranded DNA with 251 base pairs (bp) is prepared in the following way. Negative supercoiled pBR322 plasmid DNA (4361 bp) is purchased from Fermentas (Switzerland). Linear DNA fragments (251 bp) are amplified from pBR322 by PCR using 2 primers (5' CGGATTCACCACTCCAAGAA 3' and 5' TTCACGTTTCGCTCGCGTAT 3'), subsequently separated on 2.5% agarose gels, purified using a QIAprep Spin MiniPrep Kit (Qiagen) and extracted using phenol : chloroform : isoamyl alcohol 25 : 24 : 1 (Sigma). The expected length of a 251 bp DNA molecule in the three conformations illustrated in tab. 3.1 is 57.73 nm for A-DNA, 83.33 nm for

B-DNA and 95.38 nm for Z-DNA. The choice of this range of lengths allows observing a discrete number of complete molecules in a relatively small frame (typically 300 nm × 300 nm). The advantage in this choice is that effects due to scanner non-linearity and to thermal drift are minimized. The shortness of this sample with respect to more conventional DNA molecules (thousands of bp) makes it possible to increase the number of lines/pixels of acquisition and lower the scan speed, reducing noise and the chance of tip/sample getting damaged, without extending the acquisition time (always in the order of several minutes).

Fig. 3.6 shows several FM AFM images taken in vacuum on DNA deposited with Mg<sup>2+</sup> ions. The contact potential difference was compensated before all measurements. Each image has been flattened and single DNA molecules have been tracked using the software “DNA Trace” developed by Andrey Mikhaylov, a Ph. D. student working in the same laboratory as me. All the molecules entirely contained in the frame have been tracked. Evidently damaged molecules have been discarded from the analysis, as well as single stranded molecules (recognizable by their smaller height with respect to dsDNA). In the same way, 251 bp dsDNA molecules on APTES/mica have been imaged (fig. 3.7). In both cases, diamond-like carbon (DLC) whiskers ultrasharp AFM tips shown in fig. 2.6 (produced by Dmitry Klinov, Shemyakin-Ovchinnikov

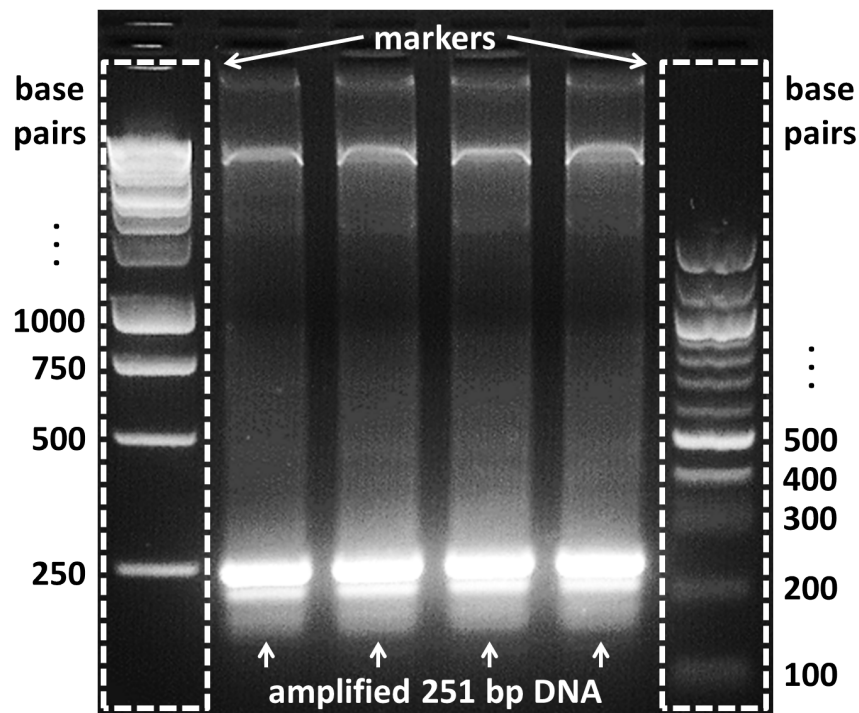


Figure 3.5: Gel electrophoresis image of 251 bp DNA molecules. After DNA amplification, this process allowed separating the DNA fragments with the desired length from the other biological material in solution. Markers (1 kb DNA Ladder on the left, 100 bp DNA Ladder on the right, both purchased from Promega AG, Dübendorf, Switzerland) are run in parallel with the amplified DNA solution (four columns in the center) in order to verify the accuracy of the amplification process. After electrophoresis DNA separation, the bands relative to 251 bp DNA were carefully cut from their columns and purified.

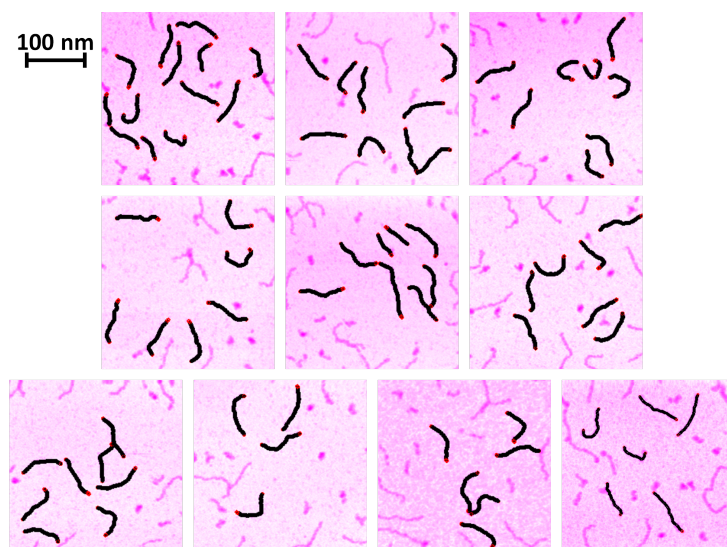


Figure 3.6: DNA molecules (251 bp) deposited on mica with  $Mg^{2+}$  and imaged in vacuum. Each frame has dimensions of  $300\text{ nm} \times 300\text{ nm}$  and  $256\text{ lines} \times 256\text{ pixels}$ . Only the last image (the first one on the right in the lower row) has  $352\text{ lines} \times 352\text{ pixels}$ . 76 molecules have been tracked.

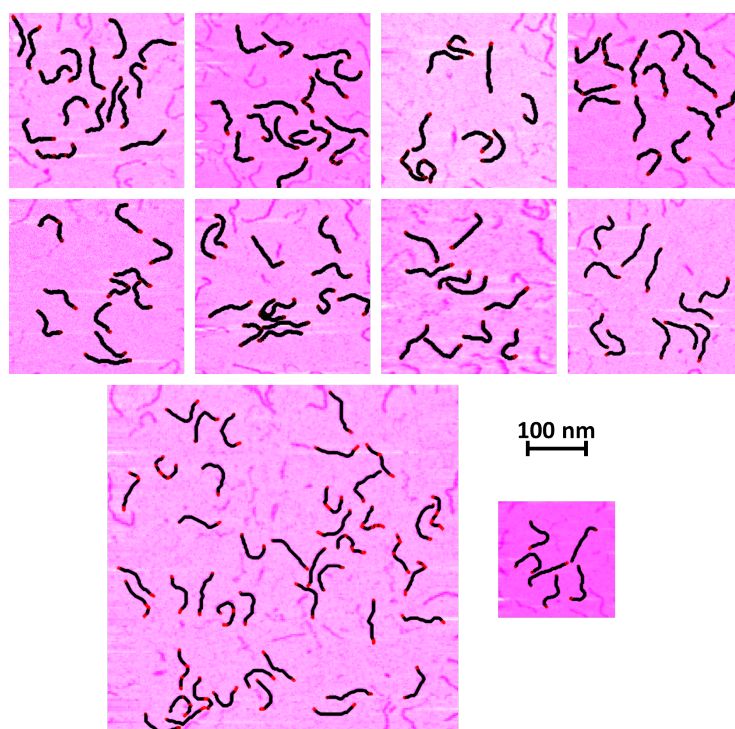


Figure 3.7: DNA molecules (251 bp) deposited on APTES modified mica and imaged in vacuum. The eight images on the top have dimensions of  $300\text{ nm} \times 300\text{ nm}$  and  $256\text{ lines} \times 256\text{ pixels}$ , apart from the first image on the right of the second row which has  $304\text{ lines} \times 304\text{ pixels}$ . On the bottom, the left image is a  $600\text{ nm} \times 600\text{ nm}$  ( $208\text{ lines} \times 208\text{ pixels}$ ) frame, while the right image is a  $200\text{ nm} \times 200\text{ nm}$  ( $208\text{ lines} \times 208\text{ pixels}$ ) frame. 149 molecules have been tracked.

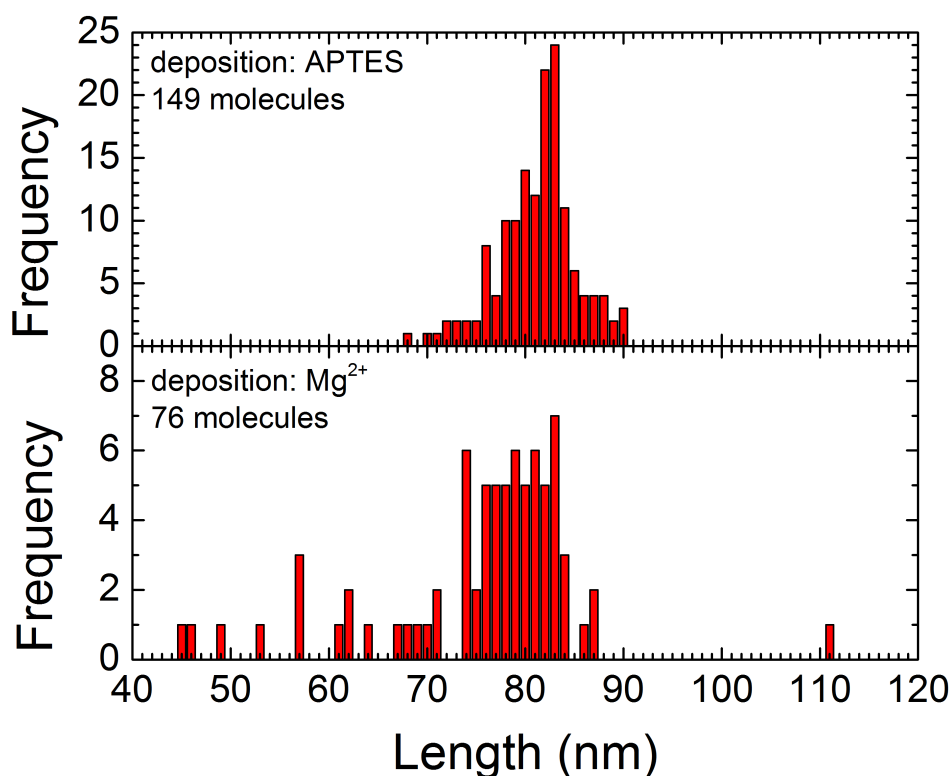


Figure 3.8: Comparison of histograms of the molecule contour length obtained with the two different methods of deposition (bin width = 1 nm). With APTES deposition, a sharp peak appears at circa 83 nm, in excellent agreement with the predicted length of a 251 bp B-form DNA molecule. A broader peak at circa 80 nm is observed with the Mg<sup>2+</sup> deposition method.

Institute of Bioorganic Chemistry, Russian Academy of Sciences, Moscow, Russia) were used to image samples. In fig. 3.8 the comparison between the contour length of DNA molecules deposited with the two methods can be seen. A clear peak at 83 nm circa is visible in the histogram relative to the APTES deposition method, in excellent agreement with the expected length of B-DNA molecules. Moreover, any evidence of populations of A-DNA and Z-DNA molecules cannot be seen in the histogram.

The contour length histogram relative to the Mg<sup>2+</sup> deposition method shows a broader peak at 80 nm circa. Some molecules are observed in a range of lengths which is significantly lower than the B-DNA theoretical length. As a matter of fact a transition from B form to A form is expected in dehydrated samples. However a significant sub-population of molecules in the A form, which should be peaking at a length equal to 57.73 nm, is not observed. The more significant number of molecules at shorter contour lengths deposited with Mg<sup>2+</sup> could be due to the conformational transition from B-form to A-form DNA which is more likely to happen with looser attachment on Mg<sup>2+</sup> upon dehydration.

The most important difference between the two histograms is the position and the width of the main peak. While the one obtained with APTES deposition is perfectly in agreement with the B-DNA length, it could be argued that a modification of the length distribution takes place

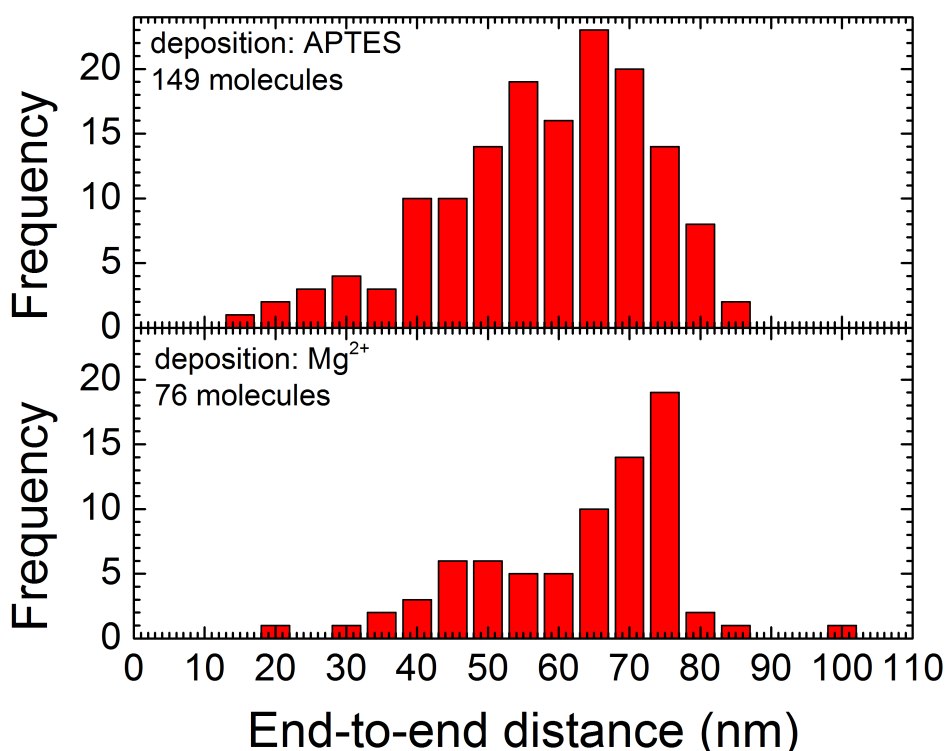


Figure 3.9: Comparison of histograms of the end-to-end distance obtained with the two different methods of deposition (bin width = 5 nm). The deposition with Mg<sup>2+</sup> produces a peak at 75 nm circa, while APTES deposition histogram has a more spread distribution, in qualitative agreement with the DNA molecules not being able to relax on the surface.

with the other method due to both the dehydration and the weaker DNA-mica Mg<sup>2+</sup> mediated interaction. The shift of the mean value of the length seems to suggest a partial conformational change from B to A form. On the other hand, the peak seems equally distributed at higher and lower values of the length. The most probable hypothesis is that the molecules slightly modify their structure because of the interaction with the substrate, being allowed to more freely relax on the surface with Mg<sup>2+</sup> deposition.

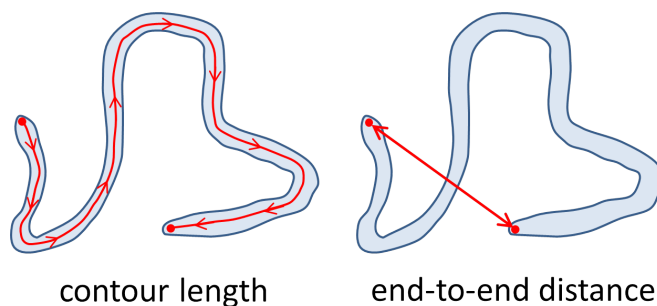


Figure 3.10: Representations of the contour length (on the left) and of the end-to-end distance (on the right) of a polymer.

The effect of the different deposition methods is evident with an analysis of the end-to-end distance of the single molecules, as in fig. 3.9. The histogram relative to the  $\text{Mg}^{2+}$  deposition shows a pronounced peak at  $70 \pm 75$  nm, while the end-to-end distance distribution appears to be more spread for molecules on APTES/mica. This is consistent with  $\text{Mg}^{2+}$  being able to relax on the surface and adopt a similar shape with less bending.

### 3.4.3 Substrate roughness

As a last criterion of comparison of the two DNA deposition methods, an analysis of the substrate roughness can be performed. To do this, two  $300 \text{ nm} \times 300 \text{ nm}$  frames with both  $256$

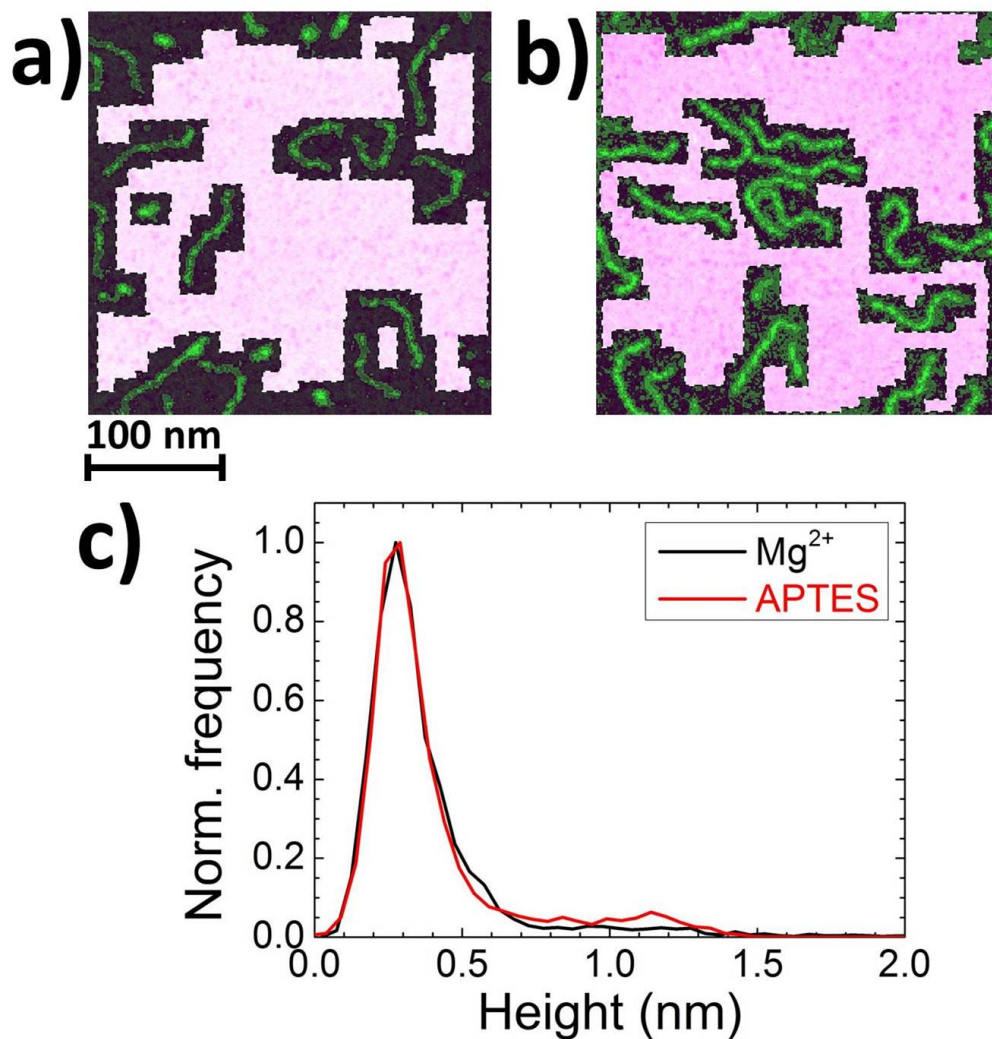


Figure 3.11: The two images on the top show the selection of the substrate in order to evaluate the surface roughness. Both images are  $300 \text{ nm} \times 300 \text{ nm}$  frames with  $256$  lines  $\times$   $256$  pixels. **a)** Substrate for  $\text{Mg}^{2+}$  deposition. **b)** Substrate for APTES deposition. **c)** Comparison of the two normalized height distributions.

lines  $\times$  256 pixels have been chosen. DNA trace software allows selecting manually areas on the molecule's substrates to produce their height distribution. For this analysis, DNA molecules and higher protrusions have not been selected. Images have been flattened subtracting a third order polynomial background to eliminate image deformations induced by the vertical thermal drift. Both distributions have been normalized with respect to their peak value to make them more easily comparable. Moreover, an offset on the abscissa has been applied in order to shift the peaks in the same position. Both distributions show a similar behavior, with a quasi-Gaussian major peak indicating the average substrate height and an elongated shoulder taking place at higher values of height. The two normalized height peaks appear to be almost identical. While a slightly more intense corrugation is visible in the range outside the mean peak for the APTES deposition distribution if compared to the  $Mg^{2+}$  distribution, no substantial differences between the shoulder obtained with the two deposition methods can be stated.

Roughness can be evaluated statistically as the arithmetic deviation from the mean value of height:

$$R_a = \frac{1}{N} \sum_{i=1}^N |z_i - \bar{z}| \quad (3.1)$$

where  $N$  is the total number of measured pixels and  $\bar{z}$  is the arithmetic average of the height. Another way is to define it as the root mean square of the sum of the quadratic deviations:

$$R_{rms} = \sqrt{\frac{1}{N} \sum_{i=1}^N (z_i - \bar{z})^2} \quad (3.2)$$

Alternatively, the mean peak can be fitted with a Gaussian curve and the fit will restitute a value for the standard deviation. The three evaluations are compared in tab. 3.2:

deposition	$R_a$ (nm)	$R_{rms}$ (nm)	$\sigma$ (nm)
$Mg^{2+}$	0.155871	0.253675	0.095195
APTES	0.176047	0.258207	0.087955

Table 3.2: Arithmetic roughness, root mean squared roughness and Gaussian standard deviation for the mean peak for distributions shown in fig. 3.11.

### 3.4.4 High resolution images

As a next step, I performed AFM images of single DNA molecules at lower scale with DLC tips in order to test if it was possible to resolve any fine sub molecular DNA structure with FM AFM. Tests were made preferentially on DNA molecules deposited on APTES/mica substrates, with the hypothesis that a minor relaxation of the DNA structure is expectable applying this deposition method, in accordance with the length measurements shown in section 3.4.2. Two main properties of DNA molecules were studied: the height of the single DNA molecule and



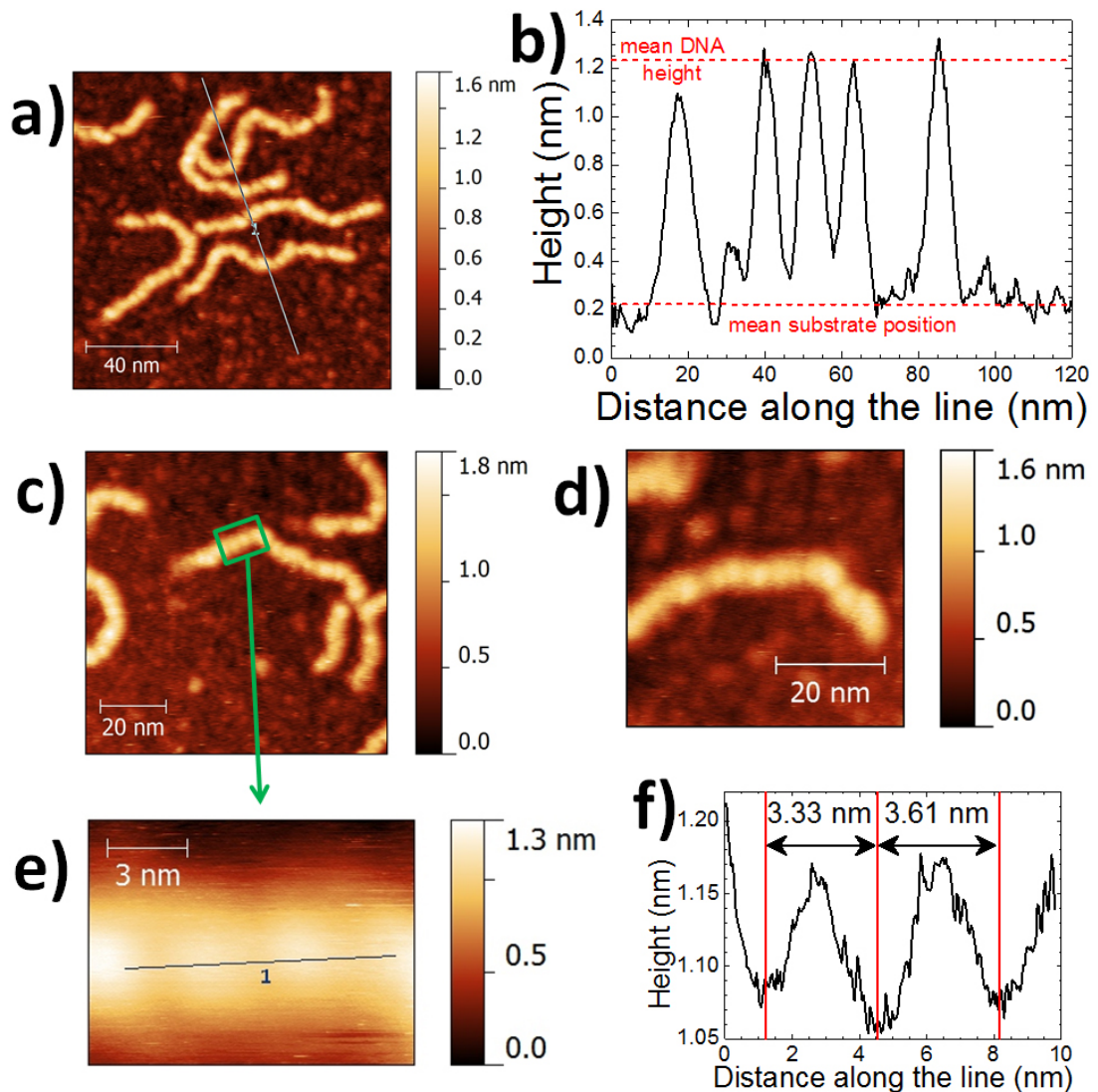


Figure 3.12: **a)** 251 bp DNA molecules deposited on APTES/mica; a height profile has been extracted along the blue line. **b)** Height profile corresponding to the blue line in image a); the mean height of the substrate and of the DNA molecules are marked with red lines, showing an average DNA height of 1 nm circa. **c)** and **d)** are images of DNA molecules on APTES(mica at smaller frames, where the corrugation on the top of the molecules is more apparent. **e)** Magnification of the portion of a DNA molecule in c) highlighted with a green rectangle. **f)** Profile tracked on the top of the DNA molecule in e), showing an average periodicity of circa 3.4 nm.

the corrugation on the top of the molecules. Basic operations on images (such as subtraction of polynomial background and profile tracking) have been done with Gwyddion 2.26 open source software [63]. As reported in section 3.1, the theoretical DNA diameter is approximately 2 nm for the three major polymorphisms. As a first observation, I noticed that the experimental height of DNA molecules with respect to the mean height of the substrate was significantly lower than the expected value, ranging roughly from 0.5 to 1 nm. Figs. 3.12 a) and b) show DNA molecules with an average height of 1 nm circa. This behavior has been already observed when performing DNA imaging in air [61, 62] and the next chapter will be dedicated to explaining this phenomenon.

In figs. 3.12 a), c) and d) several DNA molecules on APTES/mica are shown. A corrugation at nanometer scale is visible along the molecules and perpendicularly to the molecular axis. It becomes more evident in the direction of the fast scan axis, which is the horizontal axis in all the figures. This corrugation does not appear to be directly correlated with the roughness of the underlying substrate. It must be said that the periodicity of the corrugation is not constant all along a single molecule. Nevertheless, fig. 3.12 e) and f) show that it was possible to find several molecule portions having a corrugation compatible with the expected double helix periodicity of B-DNA, which is approximately 3.4 nm (see tab. 3.1).

In the recent most relevant publications about high resolution imaging of DNA [56, 57] molecules were deposited using  $\text{Ni}^{2+}$  ions. In a similar way, I made small-frame images of DNA in vacuum with DLC tips using  $\text{Mg}^{2+}$  ions (fig. 3.13), but no quality improvement concerning the detection of the periodicity over DNA was obtained. Measured height of molecules is still 1 nm circa when using the same kind of tip and the same range of  $\Delta f$  feedback set point. It does not seem that the stronger interaction of APTES with DNA causes a different compression or deformation of molecules, when comparing FM AFM images of samples prepared with the two methods. In both cases, the layer of water on DNA molecules and on the substrate is expected to be strongly reduced in vacuum. However, due to the fact that samples are not annealed once they are put in vacuum, it is possible that some structural water molecules may still be present over DNA molecules and the substrate.

All images were acquired imposing small values of  $\Delta f$  set point in the attractive range of tip-sample force (see fig. 3.14 for an example), that is relatively far from the sample. The main advantage of doing imaging in this way is that the tip is not compressing the molecules. However, the forces acting on the tip, which are basically van der Waals forces once that the contact potential difference was compensated, could be not specific enough to give the necessary level of contrast along the molecules, preventing a clear detection of the fine structural details such as major and minor grooves. In substance, the most reasonable hypothesis that explains why fine structural details (grooves) are not seen in my non-contact AFM images is probably the fact that the range of van der Waals forces is so long (a couple of nm) that when the tip is positioned at approximately 1 nm above DNA it interacts not only with the part of the molecule directly under the tip, but also with several nm of the molecule around this part. This leads to an averaged interaction which, in a way, dilutes the contrast due to the grooves.

Not being able to reliably obtain fine structural details of DNA with non-contact FM AFM imaging, I applied two alternative methods to probe DNA molecules. The first one consists of the acquiring of constant height  $\Delta f$  maps over the sample at different separations, while the

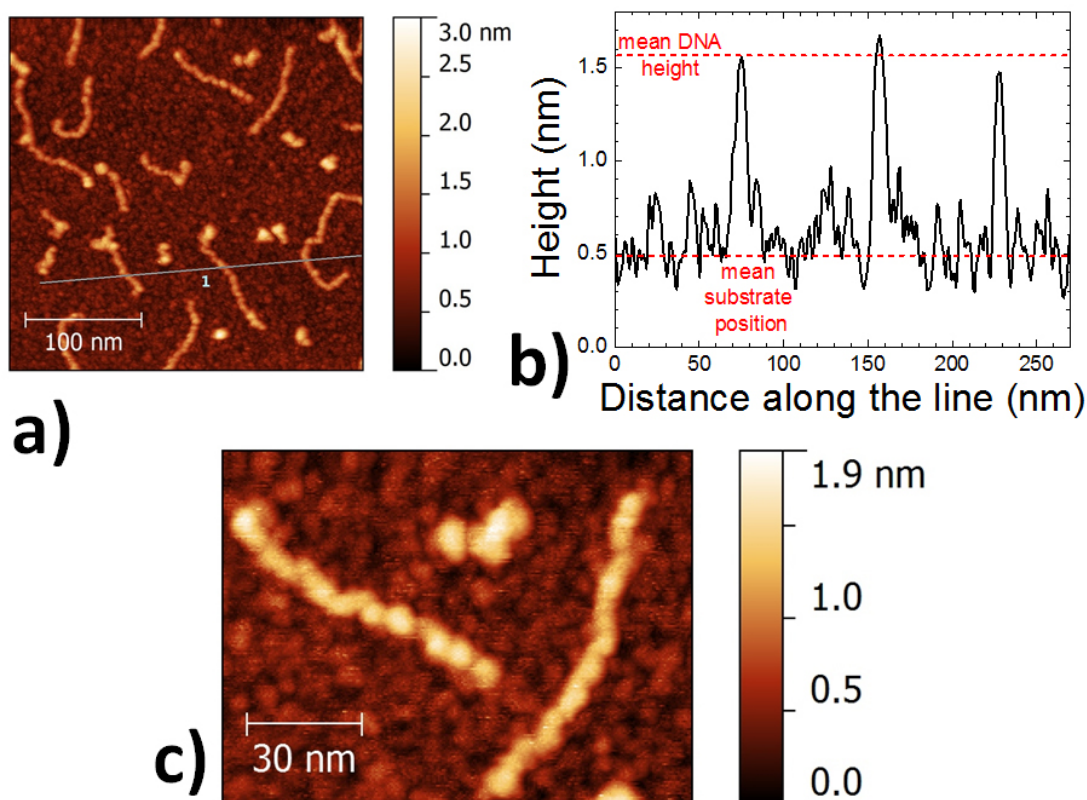


Figure 3.13: **a)** 251 bp DNA molecules deposited on mica using  $Mg^{2+}$  ions. Height profile along the blue line in a), where an average DNA height of close to 1 nm is visible. **c)** Image of DNA molecules deposited on mica using  $Mg^{2+}$  ions at higher magnification.

second consist of performing a series of spectroscopy curves along the molecular axis. The two techniques and the relative results are presented in the next sections.

### 3.5 Constant height imaging

In FM AFM the separation between the tip and the sample is controlled during the scan by means of a feedback system in order to keep the frequency shift at its set point value. In other words, FM AFM imaging can be described as a mapping of the sample surface at constant frequency shift. Frequency shift and tip-sample force are linked through eq. (1.36) and eq. (1.37) as pointed out in section 1.5. As an example, a measured frequency shift vs. distance curve and the relative calculated force vs. distance curve are shown in fig. 3.14. The quality of the image depends on the range of forces the tip experiences during the scan. If the value of the frequency detuning is too small, the separation is large and only long range contributions to tip-sample forces are probed. In this case the influence of the substrate bulk on the tip oscillation is roughly the same or dominant with respect to the influence of the substrate top layer or with respect to the DNA molecules deposited on it. This fact, combined with the lower signal-to-noise ratio, leads to a loss of contrast on the corrugation both over the substrate and over DNA molecules.

The interaction becomes more localized at shorter distances where short range forces such as Pauli repulsion are felt by the tip, and theoretically the level of resolution should increase. The problem is the high chance to deform or damage the tip and the sample, in particular when imaging soft biological molecules. Tip damaging has two important drawbacks. The first is that the image resolution depends on the tip apex radius and it is fundamental to keep the probe sharp. The second is that the continuous modification and contamination of the tip does not allow obtaining quantitatively comparable result, especially when spectroscopy experiments are performed. It turns out that in FM AFM the frequency shift set point must be chosen making a compromise between resolution and tip/sample quality.

A problem resulting from the use of a feedback is that it intrinsically introduces noise on imaging via the continuous readjustment of the scanner elongation. An optimized setting of the feedback gains and of the scan speed can minimize this noise, but it can still be the limiting factor when very small corrugation has to be observed.

Fig. 3.14 shows the non monotonic trend of the frequency shift vs. distance curve. In order to choose a set point on the left (decreasing) or on the right (increasing) side of the curve, respectively a positive or a negative value of the proportional gain constant  $K_P$  must be chosen (see eq. (1.1)). This means that either a “positive” or a “negative” feedback has to be imposed to obtain stable imaging, supposing that only small variations of  $\Delta f(t)$  around the set point value take place. Consequently, a stable feedback that allows to scan with a set point too close to the bottom of the frequency shift curve, where the monotonicity inversion is observed is

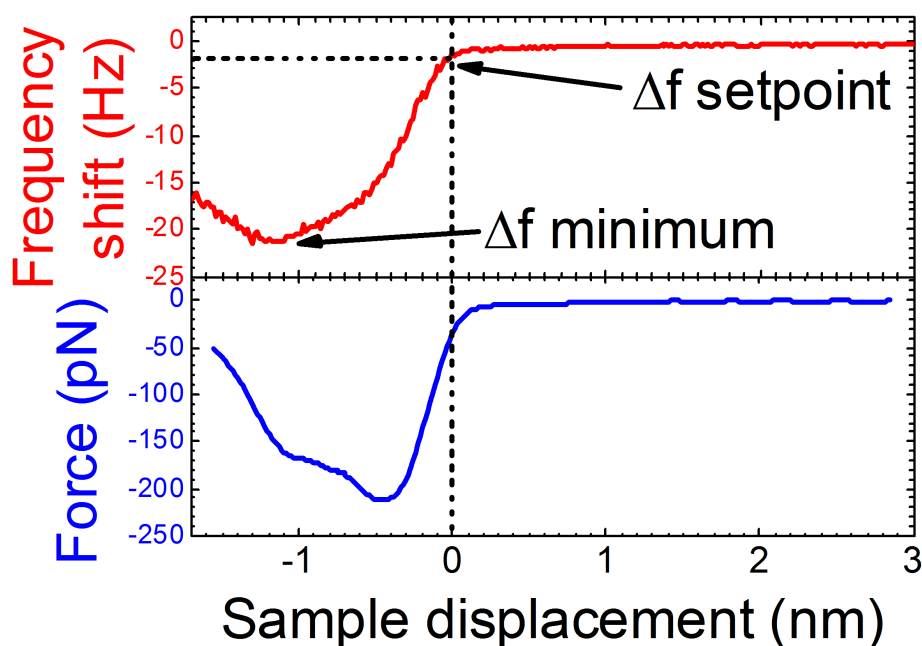


Figure 3.14: Upper graph:  $\Delta f$  curve measured on APTES in the spot marked by a cross in fig. 3.16 a). The curve is plotted as a function of the vertical piezo elongation, as the exact position of the substrate is unknown. The dashed lines indicate the  $\Delta f$  set point used in fig. 3.16 a). Lower graph: force vs. vertical piezo elongation curve, calculated from the upper  $\Delta f$  curve.

not possible. As a result, the sample can be scanned either at relatively high separation or in strong contact with the sample. In the first case, as discussed previously, the contrast may not be sufficient to resolve the sample corrugation. In the second case, all problems deriving from the tip-sample contact such as sample and/or tip deformation or alteration are likely to be observed.

The limiting effects on the resolution related to the feedback based topographic imaging have been mentioned by Gross and coworkers in their work about pentacene imaging with AFM [64]. They obtained the first atomically resolved AFM image of a single molecule. In their work, images were acquired in ultra-high vacuum at a temperature of 5 K. The tip apex was functionalized with different molecules, among which CO molecules gave the best performance in terms of contrast. Their strategy was to switch off the feedback loop and just record constant height frequency shift maps. Although this method does not give any vertical topographical information, the lateral contrast on frequency shift maps is strongly related to the structure of the underlying molecule. The use of this strategy was recognized to be critical in order to reach the range of tip-sample distance where the best level of resolution was achieved.

I attempted to apply the same strategy to my work, acquiring constant height frequency shift maps in order to improve resolution on DNA molecules. Images on the same areas of DNA molecules were made with the feedback on the scanner switched on and off. In the next paragraphs I will give details about the technique and I will show the results collected.

#### 3.5.1 Experimental details

In order to perform the constant height imaging, the tip is brought close to the sample surface and moved horizontally with respect to the substrate plane over the area to scan, with the z-feedback switched off. The tip-sample distance can be varied step by step manually after each map acquisition. This allows collecting a series of  $\Delta f$  maps and monitoring the change of contrast at different separations. A sketch of this procedure is shown in fig. 3.15 a). A limitation of this technique arises when the experiment is done at room temperature. In fact, small changes in temperature can cause thermal drift of the microscope, inducing a significant shift of the tip position with respect to the sample. An air conditioning system has been mounted in the laboratory to keep the temperature as stable as possible. This made possible to reduce the observed drift, but not completely eliminate it. The vertical piezo elongation is recorded during experiments to quantify this drift. It turns out that  $\Delta f$  maps are acquired along planes which are slightly tilted with respect to the substrate plane, as represented in fig. 3.15 b). For this reason it is more correct to define the procedure as a “no-z-feedback” instead of “constant height” mapping. The typical time scale for recording a series of  $\Delta f$  maps is of several minutes and fig. 3.15 c) shows that the drift can be assumed to be linear over a time window of about 30 minutes. The graph refers to the experiment illustrated in fig. 3.16 in the series of maps from h) to k).

The time per map, the step in z between maps and their total number are carefully chosen to minimize the drift effect on the experiment. One possibility is also to exploit the drift in order to change automatically the tip-sample separation, without making steps between one map and the other. It is possible to get a higher density of maps in this way, but the

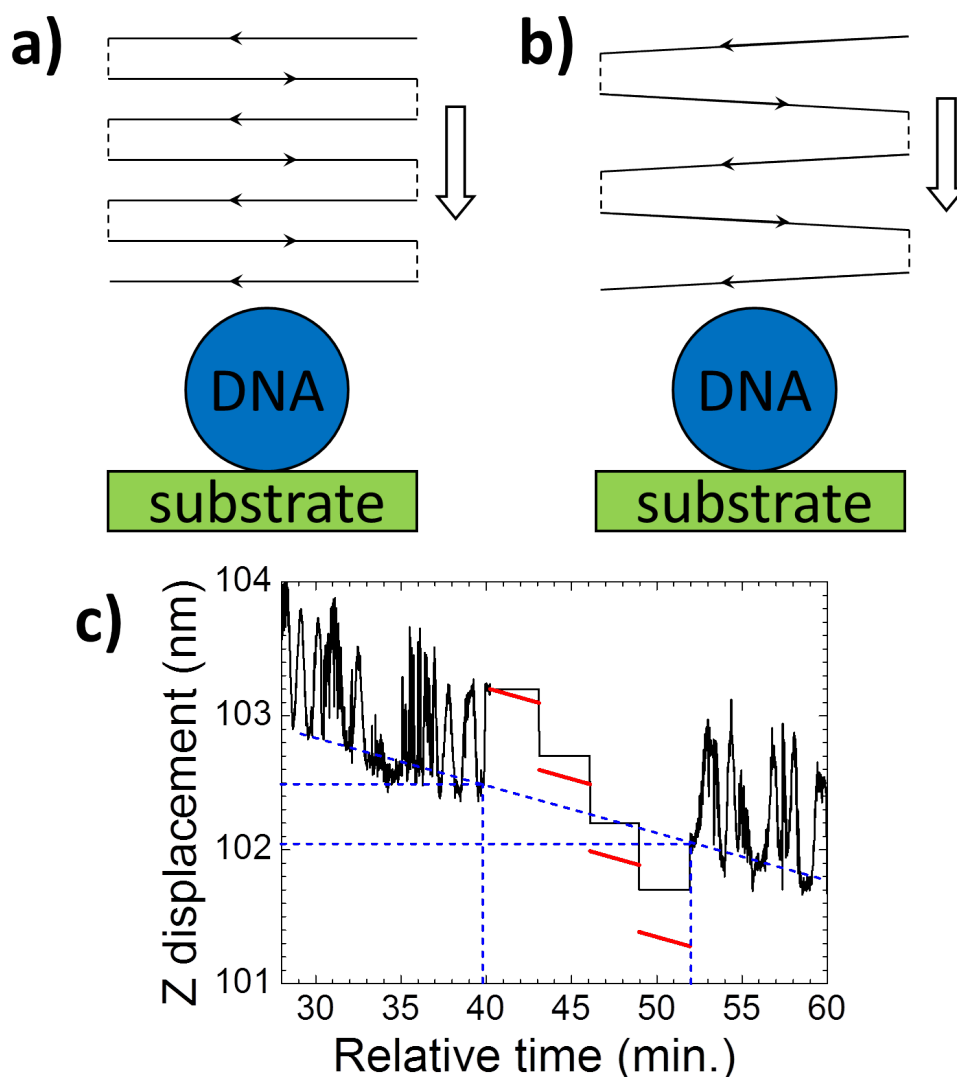


Figure 3.15: **a)** Representation of constant height imaging at different tip-sample separation. **b)** Representation of “no-z-feedback” imaging, where the plane of acquisition of each map is tilted due to the thermal drift. **c)** The graph shows the vertical movements of the piezo as a function of time (black line). The z-feedback has been switched off during the interval corresponding to the four steps, each one representing a  $\Delta f$  map. The real planes of acquisition have been determined taking into account the linear drift (red lines).

acquisition time becomes larger and the interval during which the tip is very close to the sample increases accordingly. In this way the chance to damage the tip apex is high and it is more practical to perform the experiment with discrete steps in order to keep the tip intact for several experiments.

### 3.5.2 Frequency shift maps on DNA and APTES

In all experiments the contact potential difference was compensated through the application of a bias voltage. Further, the sample and the tip have no particular magnetic properties and there is no experimental evidence of any long range magnetic forces. The remaining forces are van der Waals forces that should dominate the interaction at separations of a nanometer or more, and Pauli and chemical forces which should be taken into account at small separations of less than half a nanometer roughly. For images acquired with feedback on frequency shift in the NC AFM mode, the negative feedback and small (-1 to -2 Hz) setpoint values of  $\Delta f$  were chosen. Fig. 3.14 shows that these settings allow to maintain the AFM tip at a relatively high (> 1 nm) separation with respect to the sample. In these conditions the assumption that there is neither compression nor adhesion of the tip on the sample is reasonable. The only forces with a long enough range of interaction in this true non-contact regime are van der Waals forces.

All the images shown are the original data without any additional processing. Images were made on the same areas of DNA samples with the z-feedback switched on and off, in order to compare the resolution obtained in the two cases (figs. 3.16 and 3.17). In all the experiments presented there was constantly a feedback on the oscillation amplitude maintaining it fixed at 10 nm, a value comparable to the ones used in [65]. In fig. 3.14 the frequency shift vs. distance curve in the position marked with an X in fig. 3.16 a) is shown. The force vs. distance curve can be calculated from the frequency shift curve (see eq. (1.37)) and is shown in the bottom of fig. 3.14. In all the presented experiments where topography is measured, that is in figs. 3.16 a) and 3.16 g), the frequency shift setpoint value was fixed to -2 Hz, resulting in very small attractive tip-sample force of roughly -30 pN, as can be seen in fig. 3.14. This force value corresponds to the maximum interaction force when the tip is at its nearest distance to the sample in any oscillation cycle. The negative force value indicates that the force between the sample and the oscillating tip is attractive, i.e. the sample is being attracted to the tip and not compressed by it during the topographic scans.

In fig. 3.16 two examples are shown where topographical NC-AFM images are compared to frequency shift maps at different tip-molecule average distances. The topography images show dsDNA as a cylindrical shape molecule where no fine molecular structure such as helix's grooves can be resolved. Figs. 3.16 b)-f) and h)-k) show an increasing contrast when the tip approaches the molecule. In particular, structural details which were not visualized in the topographic image are now evident as alternating darker and brighter lines along and perpendicularly to the molecular axis.

As a control experiment, similar measurements were done on the APTES/mica substrate surface, in areas where there were few or no deposited molecules. One of these tests is shown in fig. 3.17, and it shows no similar periodic alternating lines when performing frequency shift maps at close distance. This result strongly suggests that the details observed on the top of the molecules are related to the sub molecular structure, are independent of the substrate and are not due to periodic noise or any other imaging artifact.

Frequency shift maps acquired with the z-feedback switched off show a resolution level that is not reproduced in conventional AFM topographic images. This result is partly explained by the fact that the feedback acts as a source of noise on images, as was already suggested in [64] where atomically resolved images of pentacene were obtained at low temperature

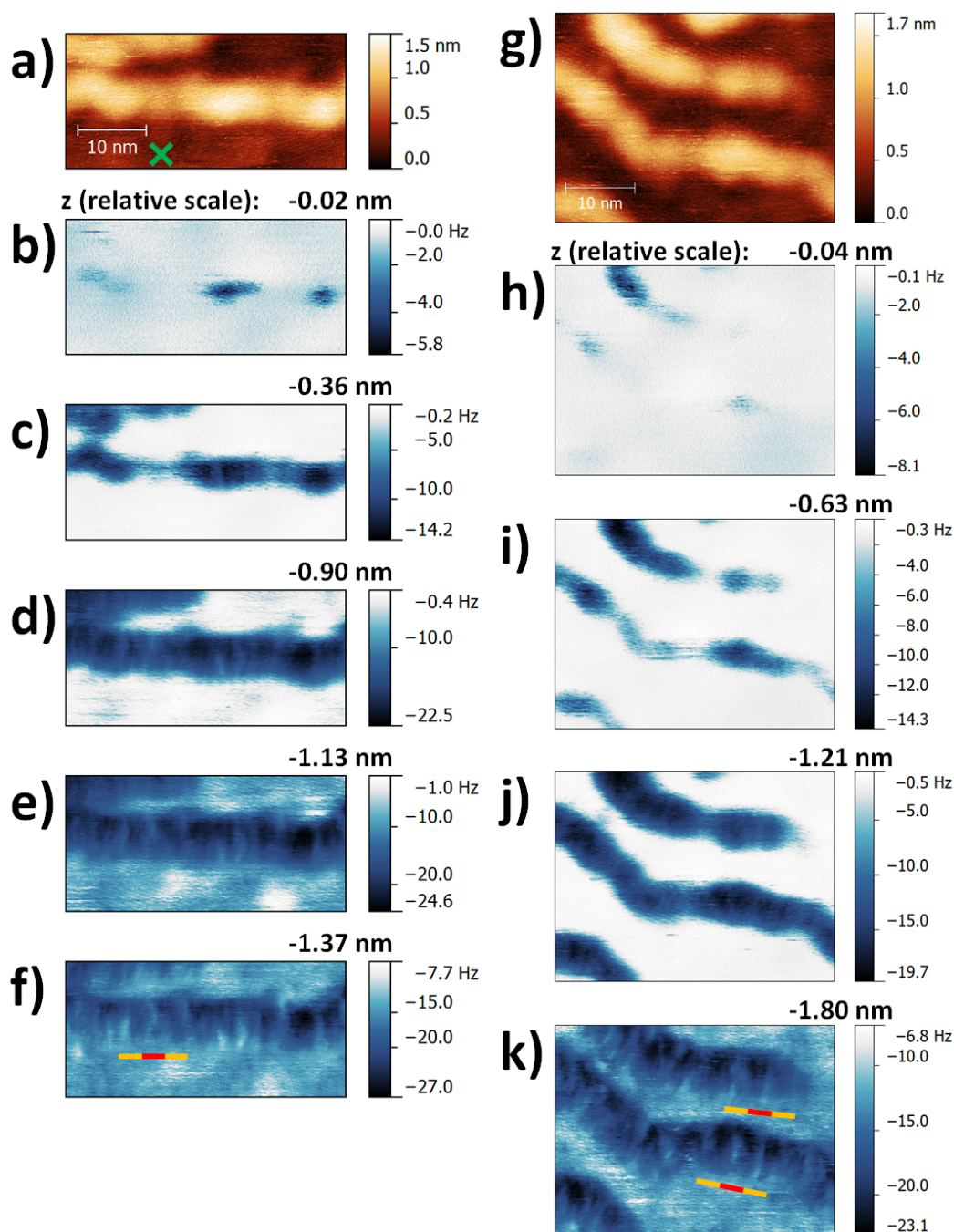


Figure 3.16: **a)** Topographic image of DNA molecules in FM AFM mode ( $\Delta f$  set point = -2 Hz). From **b)** to **f)**: frequency shift maps recorded over the same area of the sample with the  $z$ -feedback switched off (the values on the top of each map represent the average position with respect to the setpoint position). **g)** Topographic image of another area of the sample ( $\Delta f$  set point = -2 Hz). From **h)** to **k)**: as before, frequency shift maps in the same area. Colored lines are shown in **f)** and **k)** where each yellow or red portion has a length of 3.4 nm, a value that corresponds to the groove periodicity of B-form DNA helix (the total length is 10.2 nm).



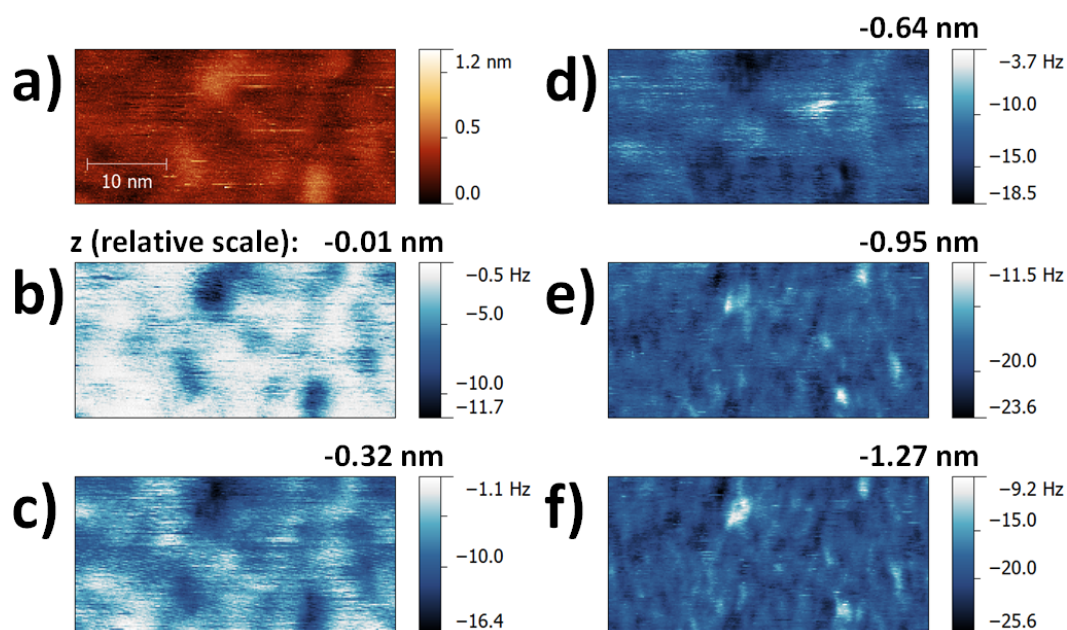


Figure 3.17: Experiment similar to the ones shown in fig. 3.16, but directly on the APTES/mica substrate surface; **a)** is the topography and **b)-f)** the frequency shift maps.

performing similar experiments. However, the major reason for the improved resolution of frequency shift maps with respect to topography images is most likely that the problem of the non-monotonicity of the frequency shift curve can be overcome. Fig. 3.16 shows that the best contrast in maps is observed at the onset of the contrast inversion. It is not possible to have a stable frequency shift feedback for FM AFM images in the same range of distances, forcing the user to set the setpoint in order to be farther in the attractive regime or nearer in the range of strong repulsive forces.

The sub molecular features along the DNA molecules are most visible in figs. 3.16 f) and 3.16 k). They appear as periodic lines along the molecule. I have added a three segment (yellow-red-yellow) lines in these two figures where each of the segments has a length of 3.4 nm which is near to the predicted B-DNA helix grooves periodicity. Thus it becomes evident that the periodicity of the lines measured in frequency shift contrast along DNA is in the same range as the expected grooves. However, there is a lot of variability in this periodicity value: the distance between lines varies between 3 and 5 nm. While these values do not always agree with the B-form DNA period, they are in good agreement with the grooves periodicity of the other two major DNA conformations, namely the A-form and the Z-form DNA (see tab. 3.1). The lines appear to be either right handed or perpendicular to the molecule and this also suggest that very heterogeneous molecules (A and B-DNA being right handed while Z-DNA is left handed) are probably observed. Generally, DNA is expected to exhibit A-form when dehydrated. However, according to the sample preparation protocol, DNA was deposited on APTES modified mica in solution, while it is still in its B and/or Z forms, and only subsequently dried. DNA strongly binds to APTES, and so it is likely that it can only partially change its conformation upon drying, which could explain the observed heterogeneity. The shape of the AFM tip, the base pair sequence of the DNA, and the way the DNA is deposited could all

influence observations, but were not yet studied systematically.

I have already developed a similar experimental approach and results have been presented in [66], but the quality of the constant height frequency shift maps there did not allow drawing any reasonable conclusions regarding the structure of DNA. Here, I have reduced the thermal drift by a factor of 2 by establishing a better temperature control in the laboratory and by doing experiments at room temperature with the copper shield closed. The quality and sharpness of the tips used in constant height experiments also appears to be essential as I observe that upon a significant damage to DLC tips, when the tip radius exceeds at least 10 nm, the regular groove like contrast is no longer observed. Finally, I built on that initial effort not only experimentally but also by building a simple model to understand the observed features in the constant height images.

To further investigate the origin of the contrast observed in the frequency shift maps shown in fig. 3.16 and verify whether it is likely that it is caused by DNA grooves I undertook a calculation of van der Waals interaction between an AFM tip (approximated by a sphere having a radius of 5 nm, similar to the radius of the AFM tip used in these experiments) and a chain of contiguous 2 nm diameter spheres (the simplest model for a molecule having the same diameter as DNA and that has grooves). Approximating an AFM tip as a sphere is a common practice in AFM modeling, e.g. as done in [67]. The 5 nm radius value was chosen as a more realistic value than the nominal 1 nm value for new unused tips because the tip was not new and was used in a dozen of no-z-feedback experiments where its radius is more likely to enlarge. DNA was modeled as a row of contiguous spheres - this is a crude model, but should give a good qualitative idea of how an AFM tip would interact with a molecule that displays grooves. The diameter of the spheres in the chain was set to 2 nm, in good agreement with the diameter of the most common DNA conformations.

In this calculation only van der Waals part of the tip-sample interaction is considered and any repulsive Pauli forces are ignored - this approximation is reasonable because in all the experimental data shown in fig. 3.16 the frequency shift is negative, hence indicating that the dominant interaction is attractive and not repulsive. Any electrostatic forces were also ignored, and this because in my experiments any contact potential difference was always compensated by applying an appropriate bias voltage. All the objects in this calculation are considered homogeneous and continuous in space. The solutions for the sphere-sphere and the sphere-plane van der Waals interactions are known [19]. The sphere-sphere van der Waals potential energy is expressed by:

$$U(s) = -\frac{A_H}{6} \left[ \frac{2r_1 r_2}{s^2 + 2s(r_1 + r_2)} + \frac{2r_1 r_2}{s^2 + 2s(r_1 + r_2) + 4r_1 r_2} + \ln \frac{s^2 + 2s(r_1 + r_2)}{s^2 + 2s(r_1 + r_2) + 4r_1 r_2} \right] \quad (3.3)$$

while eq. (2.1) is the equation of the sphere-plane van der Waals potential energy. The potential energy of the tip interaction with the chain of spheres was calculated as the sum of potential energies of the tip-sphere of radius  $r_1$  with each of the spheres of radius  $r_2$  composing the DNA chain:

$$U_{tip-chain}(x, z) = \sum_{n=1}^{20} U_n(x, z) \quad (3.4)$$

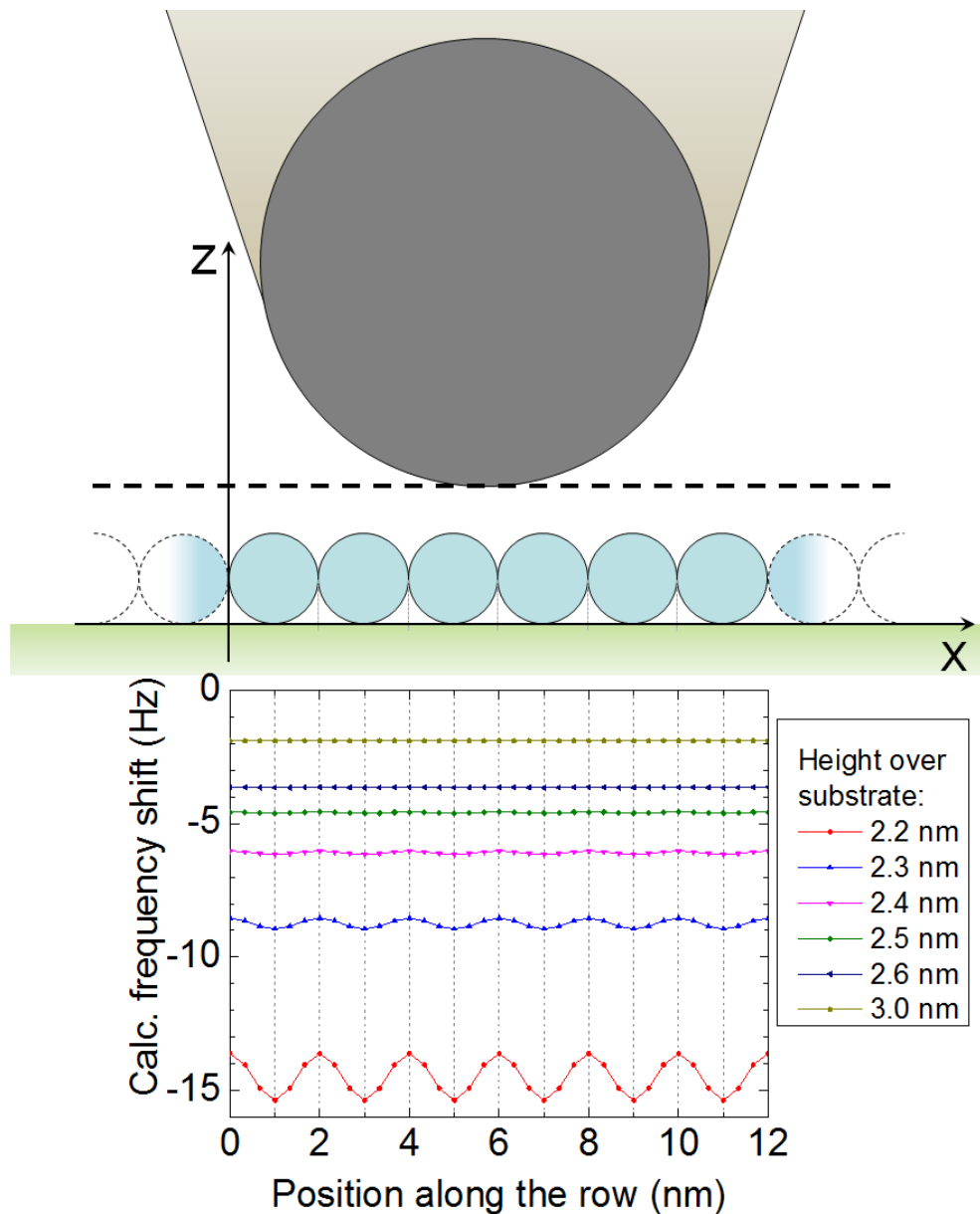


Figure 3.18: Top: sketch of the model used to calculate the frequency shift variation over DNA. The molecule is represented by a row of spheres with 2 nm diameter (20 spheres are taken into account in the calculation, while in the figure only the central ones are shown). The tip is modeled with a sphere representing its apex (tip radius is 5 nm). The values of frequency shift as a function of the tip-substrate separation are calculated from the tip-molecule and tip-substrate van der Waals forces. In the graph below, the frequency shift variation along the row of spheres at constant height (dashed horizontal line) is plotted for several values of tip-substrate separation.

where  $x$  and  $z$  are the horizontal and vertical coordinates of the center of the spherical tip, as represented in fig. 3.18. The  $x$  axis is parallel to the symmetry axis of the linear row of spheres. Each term of the sum of eq. (3.4) corresponds to the  $U(s)$  defined by eq. (3.3), where  $s$  is replaced by  $\sqrt{(z-r_2)^2 + (x-x_n)^2} - r_1 - r_2$ , where  $x_n$  is the horizontal coordinate of the center of the  $n$ -th sphere of the chain. The total potential energy of the tip-chain interaction is the sum of  $U_{tip-chain}(x, z)$  with the tip-plane van der Waals potential energy. The force was numerically derived from the total potential energy with respect to  $z$  (the vertical coordinate) and the frequency shift was then obtained according to eq. (1.36). The calculations were performed using Wolfram Mathematica 8 software. The exact DNA-DLC AFM tip Hamaker constant is unknown and I set it to  $10^{-19}$  J, which is a typical order of magnitude for Hamaker constants. The tip substrate Hamaker constant is assumed to be the diamond-mica constant value given by [68] and equal to  $1.7 \times 10^{-19}$  J.

The bottom of the fig. 3.18 shows the result of this calculation. To avoid boundary effects, frequency shifts shown in fig. 3.18 have been selected near the center of a row of 20 spheres. As can be seen in the bottom of fig. 3.18, even when at constant height above the sample, frequency shift undergoes a variation related to the groove periodicity of the sample. Specifically, there are minima of frequency shift (negative shifts) when the tip is above the bumps on the molecule and there are maxima when the tip passes above grooves. Therefore, if an AFM tip was scanned at a constant height above a molecule displaying grooves it would be expected to see a contrast similar to the one observed in figs. 3.16 f) and k). The calculation also agrees with the fact that this contrast is very weak at larger separations, e.g. figs. 3.16 c) and i), and gets stronger when the tip gets closer to the sample, as in figs. 3.16 e), f) and k). Further, despite the crudeness and simplicity of the model, the bottom of the fig. 3.18 shows that at the smallest separation of 0.2 nm there is a frequency shift baseline of about -14.5 Hz and a groove related variation of several Hz around it, which is in reasonable agreement with the experimental data in figs. 3.16 f) and k).

### 3.6 Spectroscopy measurements on DNA

In the previous section an improvement of the resolution over DNA molecules performing no- $z$ -feedback  $\Delta f$  maps has been demonstrated. The success of this method basically depends on the possibility to explore freely a larger range of tip-sample separations, without problems of feedback instability deriving from the non monotonicity of the  $\Delta f$  vs. separation curves. Coupled with this, the absence of instrumental noise caused by the feedback itself should be considered as a crucial enhancement too. Series of constant height  $\Delta f$  maps are useful in order to observe how tip-sample interaction changes at different separations. Theoretically, in absence of drift, a great number of  $\Delta f$  maps could even allow reconstructing the force profile pixel by pixel through eq. (1.37), as it has been done in [64] and [69]. Both horizontal and vertical drift of the microscope limit the applicability of this kind of method. As a technique complementary to the constant height imaging, I performed series of frequency shift vs. separation curves along the DNA molecules. This technique gives a detailed information of how the interaction varies when moving the tip vertically, while there are limitations in the lateral resolution, again due to the lateral drift. In this section, I will give some details about the way the series of frequency shift curves have been made, how data have been elaborated and I will show the results of these experiments.

## 3.6.1 Drift correction

I verified experimentally that drifts along  $x$ ,  $y$  and  $z$  can typically be assumed constant at time scales of less than 30 minutes. To calculate drifts along  $x$  ( $\Delta x/\Delta t$ ) and  $y$  ( $\Delta y/\Delta t$ ), the position of one recognizable reference spot is chosen in two images at same scale taken before and after the acquisition of the series of  $\Delta f(z)$  curves. The position of the spot is defined as  $(x_1, y_1)$  for the image before the  $\Delta f(z)$  curves and  $(x_2, y_2)$  for the image after. The time lapse between the two passages of the tip on the same spot is called  $\Delta t$  and is measured within the 2% error. I routinely recorded the  $z$  position as a function of time. The plot of  $z$  vs. time allows to evaluate the drift along  $z$  ( $\Delta z/\Delta t$ ). I called  $\Delta t_0$  the time lapse between the passage of the tip over the reference spot in the image before and the first  $\Delta f(z)$  curve. It allows to determine the exact coordinates  $(x, y)$  where the spectroscopy experiments were done and thus correct eventual drift errors. Fig. 3.19 illustrates the selection of the reference spot and the evaluation of the temporal parameters previously defined. It is worth mentioning that the scan of the same frame can be done in the “down” direction (that is, from the top of the frame to the bottom) or in the “up” direction (from the bottom to the top). To minimize problems deriving from

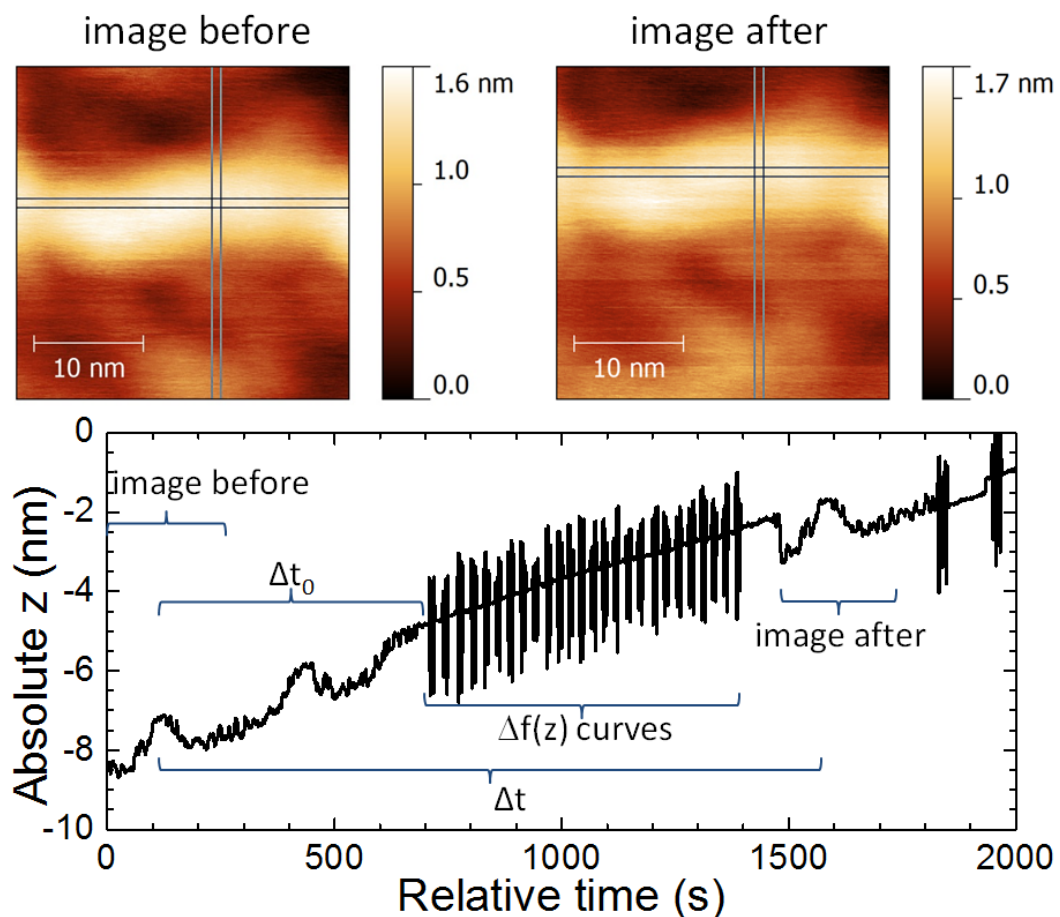


Figure 3.19: On the top, two images acquired before and after a series of spectroscopy curves showing drift in the  $xy$  plane; on the bottom, the drift in  $z$  recorded during the experiment.

piezo hysteresis, the position of the reference spot was measured on images acquired in the same direction. From the graph in fig. 3.19, it can be seen that another image was scanned lies between the “image before” and the series of curves. The image acquired in this scan was not considered for the determination of the reference spot because it was performed in the opposite direction from the “image after”.

The Nanonis software produces a file for each curve acquired, which contains information not only about the piezo  $z$  displacement and the recorded frequency shift, but also about the time and the theoretical position in which the measurement was done. It is possible to perform the series of curves selecting manually the points where to measure. Alternatively, it is possible to select a direction (generally, I preferred to move along the DNA molecule axis), the number of curves to acquire and the (constant) spacing between two consecutive curves. Exported files were analyzed and processed by means of Mathematica 8 software using a specifically written notebook. The shift of the reference spot between the two images was evaluated using the Gwiddion 2.26 software. Once the shifts  $\Delta x$  and  $\Delta y$  determined, the drift speeds  $v_x = \Delta x / \Delta t$  and  $v_y = \Delta y / \Delta t$  can be calculated. Knowing the acquisition time of each curve, it is possible to correct the theoretical  $(x, y)$  position of the measured point according to the drift.

The vertical position assigned to the curve is the position in which the  $\Delta f$  set point used for imaging is reached. In fact, for the acquisition of each curve the tip is initially placed in the set point position  $z_0$  and then lifted to the desired height over the sample  $z_{start}$ . After reaching  $z_{start}$ , the measurement begins and the tip is moved at constant speed (typically 2 nm/s) towards the sample, while the frequency shift is measured and recorded. A forward curve and a backward curve are recorded and the typical range in which the tip travels is approximately 4 nm. When the tip reaches again  $z_{start}$ , the measurement finishes and the tip is moved back to  $z_0$ . The vertical drift can be measured in an analogous way with respect to the drift in the  $x, y$  plane by measuring the  $z$  position of the reference spot before and after the curves and the vertical position attributed to each curve can be modified accordingly.

#### 3.6.2 Grooves in topography vs. grooves in force periodicity along DNA

Series of  $\Delta f$  curves were made on 251 bp DNA samples on APTES/mica. Additionally, several measurements were performed on plasmid DNA (phiX174 RF 1, made by 5386 bp), purchased from Fermentas (Switzerland). Plasmid DNA was diluted to a final concentration of 1  $\mu\text{g}/\text{ml}$  in a buffer solution containing 1 mM Tris (pH 7.8) and after it was deposited on APTES/mica with a procedure similar to the one described in 3.4.1. Both DLC and silicon Mikromasch tips were used for experiments. The oscillation amplitude was kept at 10 nm. In all the experiments an eventual contact potential difference was compensated by applying an appropriate bias voltage.

Fig. 3.20 a) shows an NC-AFM image centered on a DNA molecule. There are no topographic features that can be assigned to the fine structure of DNA such as grooves. Then  $\Delta f$  vs. distance curves following the DNA axis have been done along the red dots shown in fig. 3.20 a). The dots are not perfectly aligned with the molecular axis because we corrected their positions based on the drift, as described previously. The  $\Delta f$  curves were converted into force curves according to eq. 1.37 and plotted in fig. 3.20 b). The figure shows a tridimensional plot of the force curves, where the position along the DNA, the tip-sample distance and the force

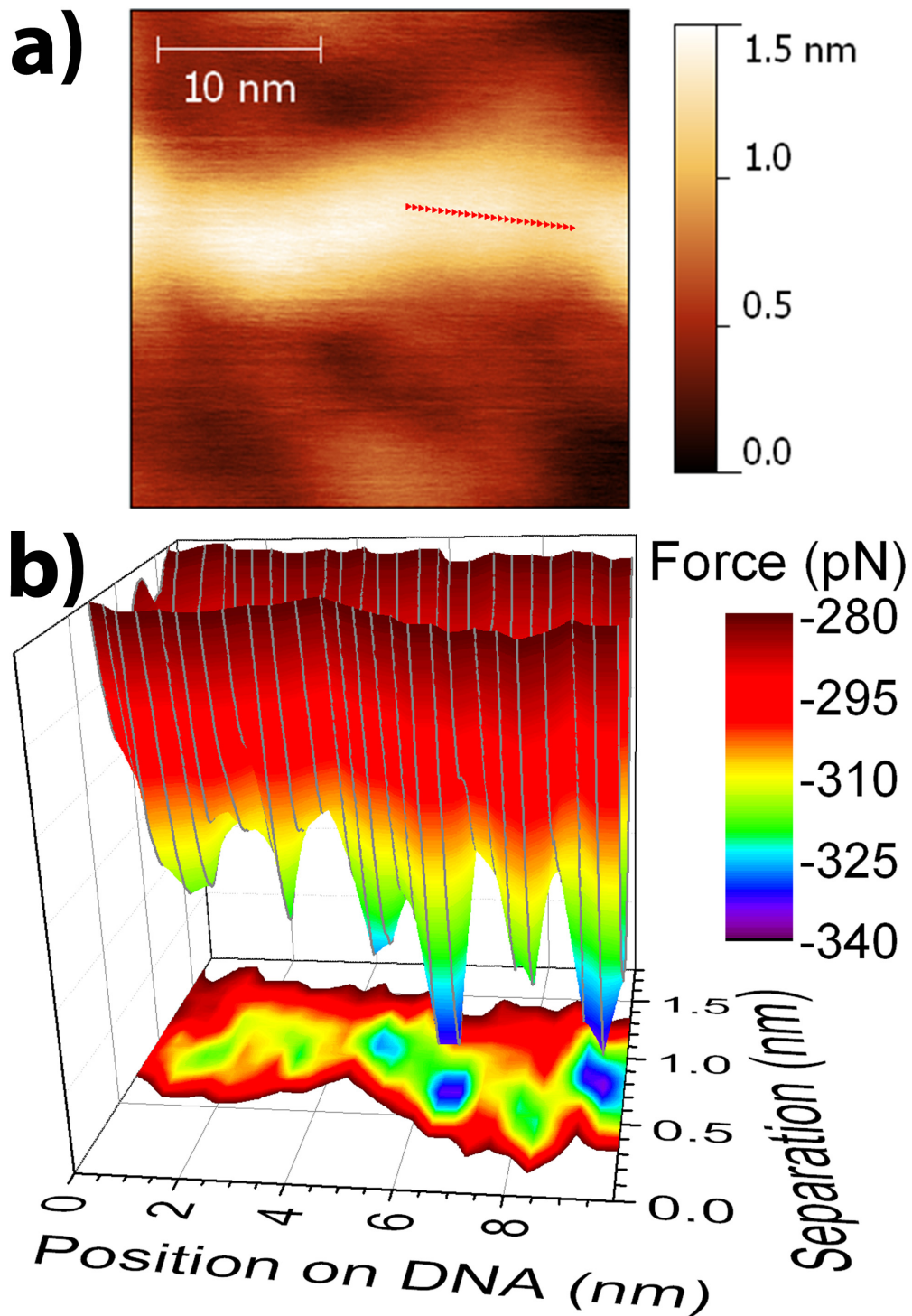


Figure 3.20: a) Topography image of a part of a DNA molecule deposited on APTES-mica: red dots show where  $\Delta f(z)$  curves were measured. b) Force curves corresponding to red dots in a); the maxima of the attractive force are plotted and reveal the positions of major and minor grooves. Grey lines are the actual force curves. The color coded force envelope and the base projection were added for better visualization of the periodicity.

### Chapter 3. Revealing the sub-molecular structure of DNA

intensity represent the x, y and z axis respectively. Due to the fact that the exact position of the substrate is not known, the zero value of tip-sample distance is arbitrary. The grey lines correspond to the force curves and the color envelope was added to code for the force value. Curves have been shifted along the tip-sample distance according to the local topography and to the vertical drift, both extracted from the data files relative to each curve and from the analysis of the z position vs. time graph in the way explained in 3.6.1. The resulting topography relative to the red dots in fig. 3.20 is shown in fig. 3.21 b).

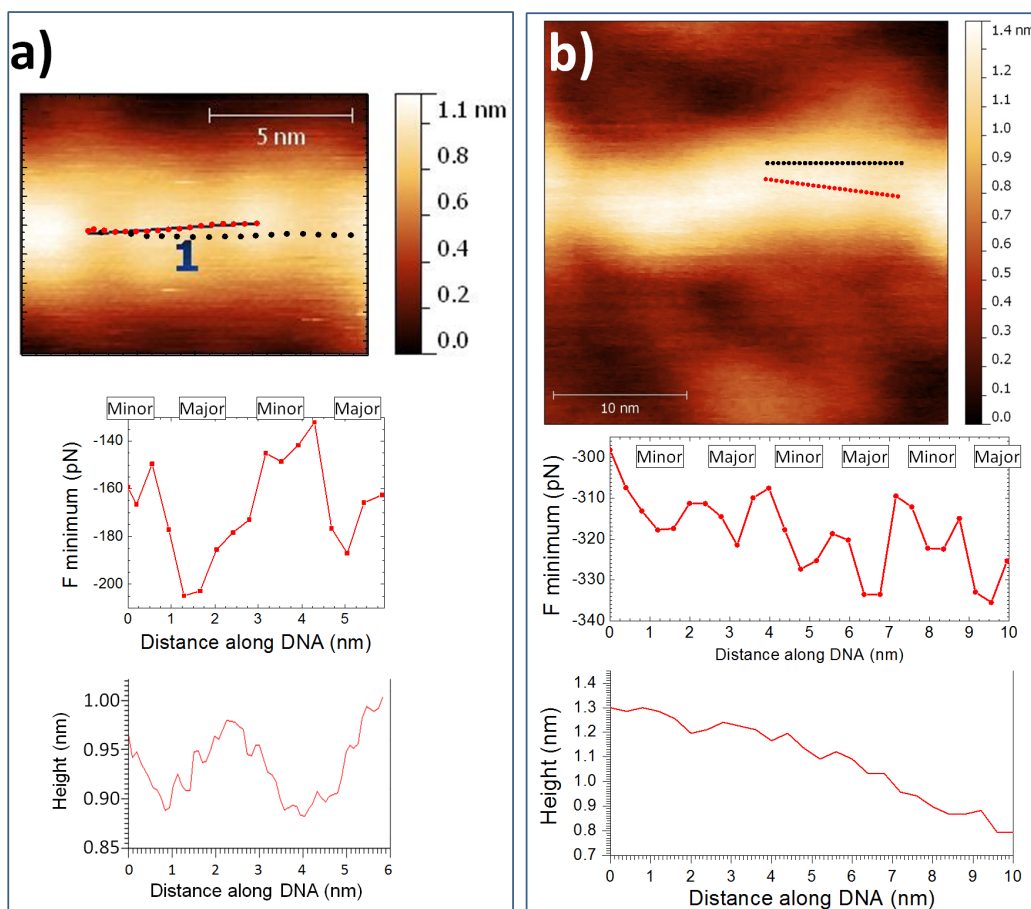


Figure 3.21: Different examples of groove-like behavior of the maximum attractive force are given in **a)** and **b)**. Images on the top have been made in FM AFM with DLC tips. Double helix periodicity has been observed in the image a), while image b) shows a pseudo-cylindrical DNA shape where any sub molecular details appear. The black dots in topographic images represent the theoretical points where curves were done, while red dots are the real position determined taking into account the drift. In the middle of the figure, the force minima are plotted as a function of the position along the molecule (by convention, attractive forces are defined as negative pointing in the inverse direction with respect to the vertical coordinate axis). In the bottom, the topography relative to the probed points reconstructed using the data files of the curves and studying the vertical drift.



In this plot there are clearly distinguishable periodic peaks in the force value with a periodicity of 3.4 nm, in excellent agreement with the B-DNA grooves periodicity. Further, between any two 3.4 nm distanced larger peaks there is always a smaller one corresponding to a minor groove. The example in fig. 3.20, where no clear contrast in topography is seen, is the most common one. However, in some cases I observed contrast both in topography (only the major grooves) and in forces (both major and minor grooves), as it can be seen in fig. 3.21.

This visualization of major grooves in topography was possible only when the sharpest tips were used. As shown in fig. 3.21, the major grooves in FM AFM imaging can be seen with the ultra-sharp DLC tips where the maximum attractive force is approximately 205 pN, but are not visible with a similar DLC tip where this force reaches values of 335 pN circa. There is a slight mismatch between the positions of grooves in topography and force curves in 3.21 a), which can probably be attributed either to imperfect drift correction or to some tip apex asymmetry. Most generally, the importance of drift in the x,y plane shown in these examples highlights a major difficulty with this approach which is to stay on top of a 1 nm radius DNA molecule over sufficient lengths and time to observe grooves.

I correlated the size of the tip with the value of the maximum attractive force: it is expectable that larger tips cause larger attractive van der Waals forces. In the same way, a larger tip radius causes a most evident delocalization of the tip-sample interaction, leading to a lower contrast when measuring in the purely non-contact range of distances. A most detailed model of the groove contrast will be shown in the next chapter. On the other side, the visualization of grooves as maxima in force curves along DNA is more reproducible with ultra-sharp tips and occasionally I also obtained grooves contrast with duller 10 nm radius tips as it will be discussed later.

These results indicate that sharp tips allow resolving the double helix DNA periodicity in some areas of DNA molecules. The sharpness of the tip appears to be a critical factor for obtaining such a kind of resolution. Inversely, when probing the DNA structure by means of series of  $\Delta f$  curves, the observation of major grooves is more reproducible and the sharpness of the tip is less crucial. Moreover, secondary maxima of attractive force ascribable to minor grooves' detection are often measured.

#### 3.6.3 Grooves with a blunt 10 nm radius tip

Position of grooves can also be uncovered with a relatively blunt tip. In the example above we used a silicon 10 nm radius tip (Mikromasch) to image and probe grooves on DNA. Top left is the topographic image at constant  $\Delta f$  setpoint equal to -20 Hz, and does not show the expected periodicity. The bumps visible on DNA in the topographic image correspond very likely to the bumps of the APTES substrate with an average size close to 10 nm. The line on DNA made of red triangles shows where the  $\Delta f(z)$  curves were recorded. Top right corner shows the corresponding curves. Stronger attractive interaction of up to 850 pN (typical values with ultra sharp 2 nm radius tips are about 300 pN) is in good agreement with the larger tip size, causing a larger van der Waals interaction. Bottom plot is a zoom-in into maximum attractive force region and shows force maxima positions along DNA with 3.4 nm periodicity in excellent agreement with major and minor grooves of B-DNA.

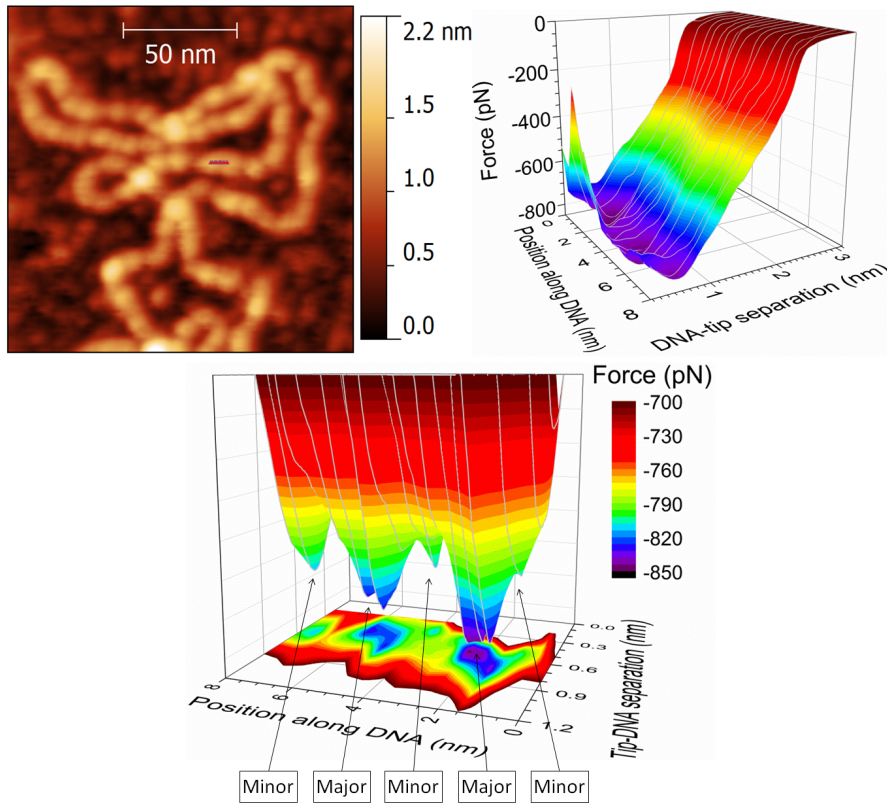


Figure 3.22: 3D representations of the force vs. distance curves acquired on the line indicated in the top left image. Plasmid DNA was imaged using silicon Mikromasch tips, having a nominal radius larger than DLC tips and estimated to be 10 nm circa. The image on the bottom is a magnification of the region near to the force minima of the 3D color plot on the top right.

### 3.6.4 Sphere-chain of spheres: grooves contrast

I made a simple quantitative model for the tip-DNA interaction to explain the contrast observed in force curves in fig. 3.20. The tip is again modeled as a sphere  $S$  representing its apex. The DNA molecule is modeled as a row of contiguous spheres  $s_i$  with radius  $r = 1$  nm. The tip radius was set to  $R = 2$  nm. To avoid boundary effects, forces have been selected near the center of a row of 20 spheres that has its symmetry axis along the  $x$  axis. A sketch of the model and results are shown in fig. 3.23. The solution for the van der Waals interaction is:

$$\begin{aligned}
 U(x, z) = & -\frac{A_H}{6} \sum_{i=1}^{20} \left\{ \frac{2Rr}{d_i^2(x, z) - (R+r)^2} + \right. \\
 & \left. + \frac{2Rr}{d_i^2(x, z) - (R-r)^2} + \ln \left[ \frac{d_i^2(x, z) - (R+r)^2}{d_i^2(x, z) - (R-r)^2} \right] \right\} \quad (3.5)
 \end{aligned}$$

where  $A_H$  is the Hamaker constant which was set to  $10^{-19}$  J, its typical order of magnitude, and  $d_i(x, z)$  is the center-to-center distance between S and  $s_i$ . If  $x_i$  is the horizontal position of the  $i^{\text{th}}$  sphere in the row, then, in the reference frame,  $x_i = (2i - 1)r$  and  $z_i = 0$ , it is possible to obtain  $d_i(x, z) = \sqrt{(x - x_i)^2 + z^2}$ . For each point forces are calculated knowing that  $F_z(x, z) = -\partial_z U(x, z)$ . The forces were derived from the potential energy numerically. I defined a constant separation  $\xi$  along which the forces were calculated in such a way that  $d_i = r + R + \xi = \text{const.}$  where  $d_i$  is the distance with respect to the  $i^{\text{th}}$  sphere. If the probe is in the interval  $2(i - 1)r < x < 2ir$ , the position of the center of the probe is set in order to maintain the same distance  $d_i$  from the center of the  $i^{\text{th}}$  sphere. The probe center trajectory is defined by  $z(x) = \sqrt{(r + R + \xi)^2 - (x - x_i)^2}$ , where  $2(i - 1)r < x < 2ir$  and  $i = 1, \dots, 20$  and is shown with the dashed line.

Fig. 3.23 shows that van der Waals forces maxima occur over the grooves between the spheres for all the tip separations. Since Pauli repulsive forces have several orders of magnitude smaller range than van der Waals attractive forces, we can approximate that when they start acting

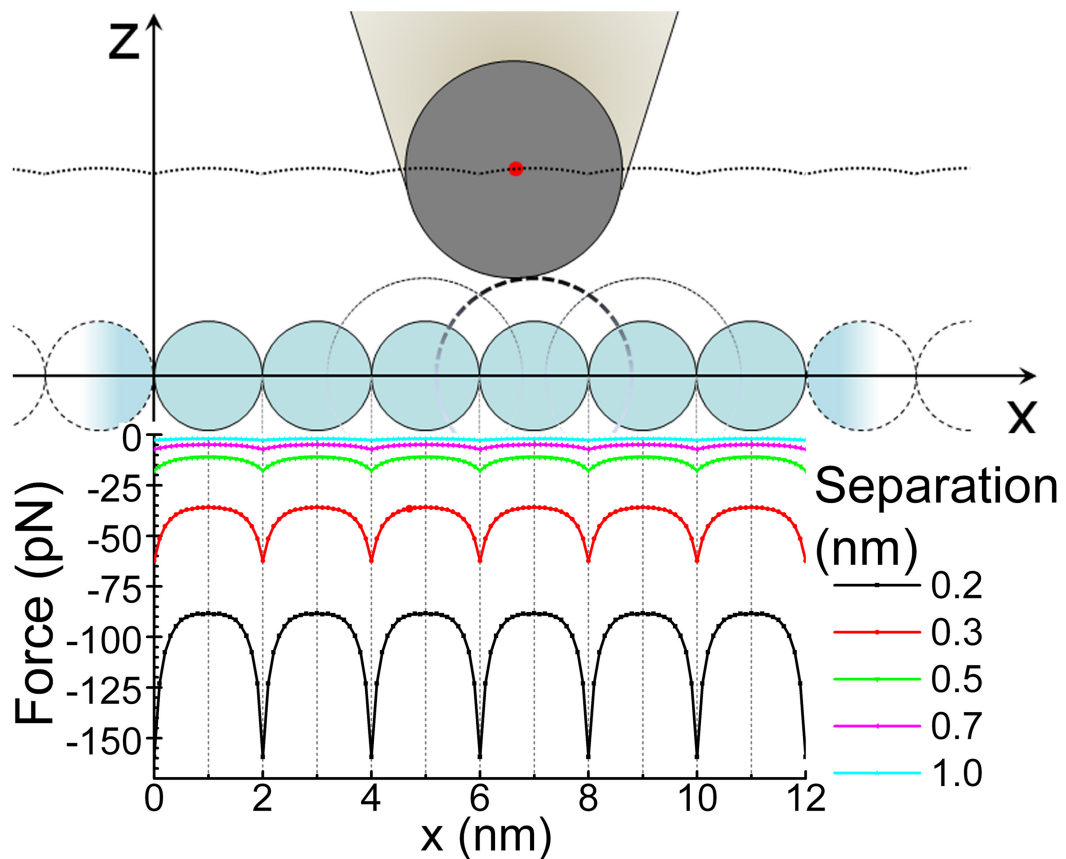


Figure 3.23: Top: A scheme showing the tip (approximated with the darker sphere in the calculations) and DNA (approximated as a chain of 20 2 nm diameter spheres). Bottom: calculated van der Waals tip-spheres interaction at different tip-sample separations. Maxima in van der Waals interaction force correspond to grooves between the spheres.

the maximum attractive force is dominated by the value of the van der Waals interaction. In fig. 3.23 van der Waals forces are plotted as a function of the tip position along the DNA chain and for several separation values. This simple, yet quantitative model uncovers the contrast origin in force plot along DNA in fig. 3.20. The tip-DNA separations given in fig. 3.23 are absolute, while the one in fig. 3.20 is relative since the true distance between tip and DNA cannot be elicited from the experiments. At separation values of more than 0.5 nm there is a sharp decrease in contrast, which appears in good agreement with experimental data and could explain why we rarely observe grooves in topographic images. From the above considerations and fig. 3.23 one might conclude that topography images should be taken with much bigger negative frequency shifts where the contrast along the DNA chain should be more pronounced. However, experiments have evidenced that the very sharp tips are rapidly damaged during scanning in these conditions. Moreover, the discussion presented in section 3.5 showed that a real improvement of resolution is obtained near to the minimum of  $\Delta f$  curves, where the FM feedback is actually instable. The mode that demonstrated in fig. 3.20 of taking successive force curves along the DNA molecule has proven to be viable and to give the highest level of lateral resolution if compared with the normal FM AFM imaging and with the constant height mapping.

## 4 Quantitative AFM height measurements

The height of DNA molecules measured in vacuum with FM AFM appears to be smaller than the value of circa 2 nm determined by diffraction measurements, as anticipated in section 3.4.4. Similar results have been obtained also for AFM measurements in air in literature. In this chapter, I will give an explanation of how this mismatch between experimental data and theory can be due to the different van der Waals interaction between tip and DNA and between tip and substrate. I will present height measurements made on DNA molecules with DLC and silicon tips. I will simulate a FM AFM experiment determining what is the vertical position of the tip during the scan at constant  $\Delta f$ . The calculated DNA height will then be defined as the difference between the tip vertical position when the tip is over the DNA and when it is over the bare substrate. Mathematical models for the van der Waals tip-DNA and tip-substrate interaction have to be assumed in order to perform these calculations. Descriptions of the models and details about the height calculations will be presented here.

### 4.1 Measured DNA height with DLC and silicon tips

In this section I will show a statistical study of the height of DNA molecules measured with FM AFM in vacuum and I will compare results obtained using DLC and silicon tips. Images showing the height of DNA molecules have been already presented in section 3.4.4. In figs. 3.12 and 3.13 profiles have been tracked along frames containing DNA molecules and the DNA height was estimated as the average height of the top of the DNA molecules with respect to average position of the substrate. A more statistical analysis of the height is presented in this section and it was made using the DNA Trace software, already cited in section 3.4.2.

For each image, areas of the substrate have been chosen and the height relative to each selected pixel was extracted in order to generate a histogram. As a criterion, areas containing DNA molecules or any protuberance not consistent with the substrate roughness were not included in this analysis. A separated histogram to determine the mean position of the top of DNA molecules was made. The DNA Trace software allows tracking paths along single molecules, asking the user to select the “starting point” and the “last point” of each molecule. Other parameters set by the user are the step between points along the path and a height threshold. This threshold allows to distinguish between “molecule” and “background”, forcing the algorithm used by the software to choose a path which remains over the molecule. The

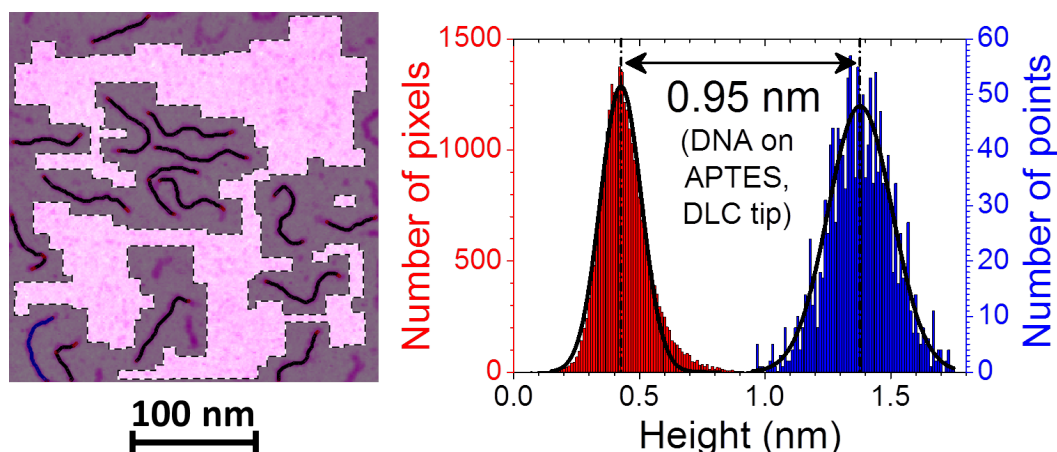


Figure 4.1: On the left, an image of 251 bp DNA molecules on APTES/mica ( $300 \text{ nm} \times 300 \text{ nm}$ ,  $256 \text{ pixels} \times 256 \text{ pixels}$ ). A DLC tip was used for imaging. The cantilever resonant frequency was  $f_0 = 336245 \text{ Hz}$  and the set point was  $\Delta f = -1.5 \text{ Hz}$ . On the right, height histograms of the substrate (in red) and of the DNA molecules (in blue), with the relative Gaussian fits.

software automatically tracks a path between the two points. The path is selected maximizing the height of each point along it and minimizing the total length of the path. For each image, the heights of the points along all the tracked molecules were collected to make a single histogram. The measured DNA height was then defined as the distance between the peaks of the two histograms.

DNA samples were prepared using the procedures described in section 3.4.1. I compared the

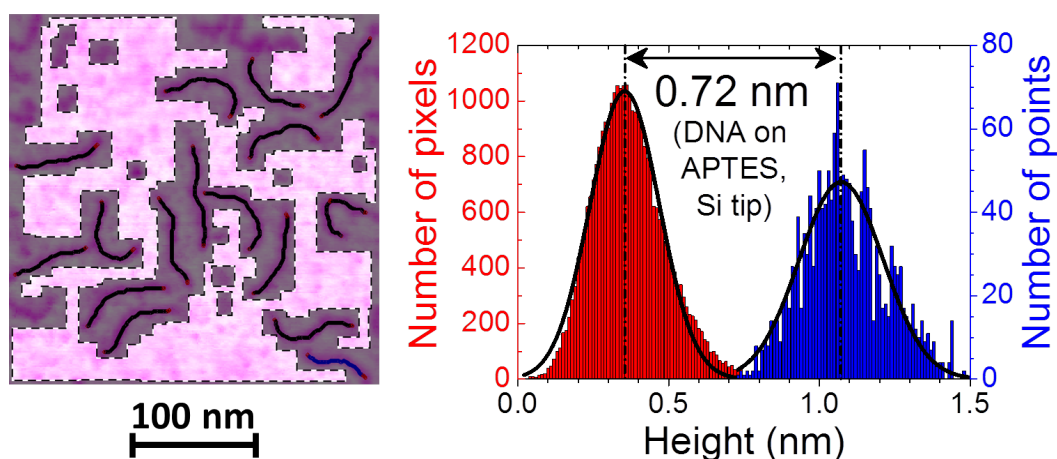


Figure 4.2: On the left, an image of 251 bp DNA molecules on APTES/mica ( $300 \text{ nm} \times 300 \text{ nm}$ ,  $256 \text{ pixels} \times 256 \text{ pixels}$ ). A silicon tip (Mikromasch NSC35 B) was used for imaging. The cantilever resonant frequency was  $f_0 = 356157 \text{ Hz}$  and the set point was  $\Delta f = -20 \text{ Hz}$ . On the right, height histograms of the substrate (in red) and of the DNA molecules (in blue), with the relative Gaussian fits.

#### 4.1. Measured DNA height with DLC and silicon tips

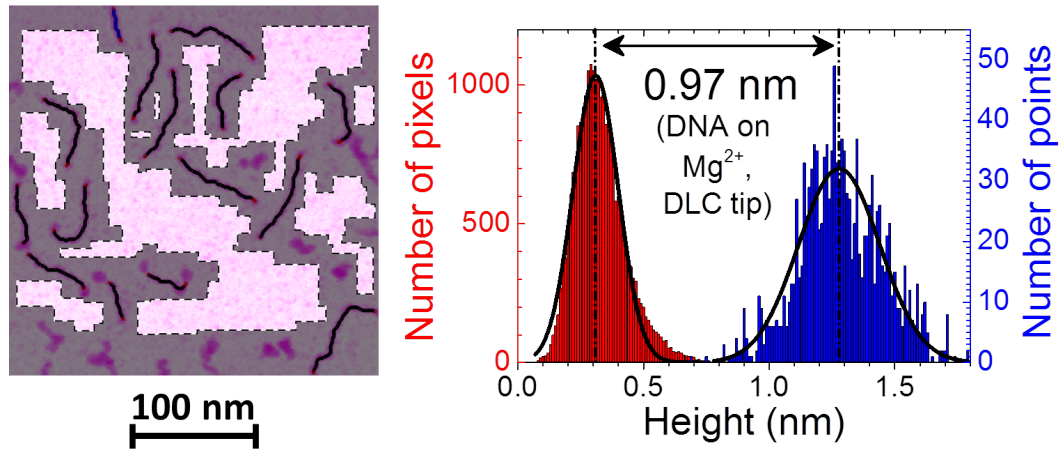


Figure 4.3: Image of 251 bp DNA molecules on mica deposited with  $Mg^{2+}$  ( $300 \text{ nm} \times 300 \text{ nm}$ ,  $256 \text{ pixels} \times 256 \text{ pixels}$ ) and relative histograms of the height distributions of the substrate and of the molecules. The sample was measured with a DLC tip. The resonant frequency was  $f_0 = 326603 \text{ Hz}$  and the set point was  $\Delta f = -2 \text{ Hz}$ .

measured height of 251 bp DNA molecules imaged both with DLC and silicon tips by FM AFM in vacuum. A DNA sample deposited on APTES/mica and measured with a DLC tip is shown on the left side of fig. 4.1. The bright areas correspond to the portions of the substrate taken into account for the determination of the average substrate height. DNA molecules were also tracked and on the right side of fig. 4.1 histograms relative to the substrate (red) and to the molecules (blue) are shown. Both the histograms were fitted with Gaussian curves. As it can be seen in fig. 4.1, the histogram relative to the substrate is slightly asymmetric, being the right tail of the distribution more pronounced than the left one. This can be due to the presence of small clusters of polymerized APTES molecules, of salts contained in the DNA solution or air contaminants. Nevertheless, the peak of the Gaussian curve corresponds quite well to the peak value of the histogram. The histogram relative to the height of DNA molecules appears to be more symmetric. The same behaviors have been observed for the Gaussian fits presented in figs. 4.2 and 4.3. The distance between the peaks of the two Gaussian curves is 0.95 nm. The peak values and the standard deviations of the two histograms are shown in table 4.1.

The same method of analysis was applied to DNA samples scanned with silicon tips. An example is shown in fig. 4.2, where a Mikromasch NSC35 B cantilever was used as probe to image 251 bp DNA molecules on APTES/mica. The measured DNA height, again evaluated as the distance between the two Gaussian peaks, is equal to 0.72 nm in this case. There is an

Table 4.1: The peak values  $h$  and the standard deviations  $\sigma$  of the Gaussian fits shown in figs. 4.1, 4.2 and 4.3 are reported here.

	$h_{sub}$ (nm)	$\sigma_{sub}$ (nm)	$h_{DNA}$ (nm)	$\sigma_{DNA}$ (nm)	$h_{DNA} - h_{sub}$ (nm)
DLC, APTES	0.4263	0.08167	1.3784	0.12797	0.9521
Silicon, APTES	0.35432	0.115	1.07229	0.13943	0.71797
DLC, $Mg^{2+}$	0.30977	0.09006	1.27864	0.16229	0.96887

evident reduction of the measured height when using a silicon tip with respect to the result obtained with a DLC tip (fig. 4.1). The main differences between the two experiments is the material of the two tips and their nominal apex radii (see table 2.1). These differences have an impact also on the typical  $\Delta f$  set point values to use in order to obtain well contrasted images. As an example, a  $\Delta f = -1.5$  Hz was set in the experiment when the a DLC tip was used (the resonant frequency of the cantilever was  $f_0 = 336245$  Hz), while a  $\Delta f = -20$  Hz was set in the experiment with the silicon tip (here  $f_0 = 356157$  Hz).

I performed the same kind of measurement on samples prepared with the  $\text{Mg}^{2+}$  in order to check the dependence on the deposition method of the DNA height when imaging using FM AFM. In fig. 4.3, 251 bp DNA molecules deposited with  $\text{Mg}^{2+}$  are shown. I used a DLC tip for this measurement. The resonant frequency of the cantilever was  $f_0 = 326603$  Hz and I set  $\Delta f = -2$  Hz. The DNA height measured in this case was 0.97 nm circa, in good agreement with the result obtained using a DLC tip to image DNA molecules on APTES/mica and shown in fig. 4.1.

In conclusion, the height of DNA molecules measured by FM AFM in vacuum is smaller than the predicted value of approximately 2 nm for DNA samples prepared both with the APTES and with the  $\text{Mg}^{2+}$  deposition method. Moreover, experiments showed that the tip material and its dimensions have an influence on the value of the measured height. Inversely, the sample preparation method (APTES or  $\text{Mg}^{2+}$ ) does not vary significantly the DNA height, when samples prepared using the two methods are imaged with the same kind of tip. The next sections of this chapter will be dedicated to the explanation of these observations.

### 4.2 Tip and DNA models for the AFM height calculations

When imaging in non-contact FM AFM, the separation between the tip and the sample is typically of the order of few nanometers. Within this range of distances and once that the contact potential difference has been compensated, attractive van der Waals forces can be reasonably assumed as the major contribution to the total tip-sample interaction. All discussions and calculations in this chapter are based on the simplifying assumption that only van der Waals forces acted on the tip when it is at close separation with respect to the sample. I also assumed that the tip and the sample were homogeneous and continuous bodies and that tip-sample attractive forces did not deform the shape of both the tip and the sample. The AFM tip was modeled as a sphere and relatively simple geometries to describe the DNA shape were used, such as an infinite cylinder and a linear row of spheres.

All the hypotheses I made led to a strong simplification of the tip-DNA interaction. The real double helical DNA structure, with two sugar-phosphate backbones and base pairs in the center, was extremely approximated and as an example my calculations did not depend on the real base pair content of DNA. The Hamaker constant of the van der Waals tip-DNA interaction was assumed to be an averaged value over all the DNA volume, where differences depending on the different nature of the backbones and the nucleobases are expectable. The DNA molecules, their substrate and the tip were supposed to be continuous bodies also when the tip-DNA or the tip-substrate separation was relatively small (order of 1 nm).

Nevertheless it will be shown that my hypotheses, in spite of their simplicity, allowed calcu-



lating the FM AFM height of a DNA molecule in both qualitative and quantitative agreement with the measured values. My results show that it is possible to explain the DNA height loss in dry environments without assuming a modification of the original B-form DNA structure due to the non-physiological environmental conditions.

### 4.2.1 Van der Waals potential energy for simple geometries

Contributions of different nature are included under the definition of van der Waals interactions. They comprehend the interaction between permanent electric dipoles, the one between permanent and induced electric dipoles and the one between instantaneously induced electric dipoles. When considering two point-like objects interacting at a distance  $r$ , all these contributions have the same  $r^{-6}$  dependence on the distance. The van der Waals potential energy can be generically written as:

$$u(r) = -\frac{\beta}{r^6} \quad (4.1)$$

where  $\beta$  is a factor depending on the nature of the two point-like objects. When two extended discrete bodies are interacting, potential energies relative to each couple of components of the two bodies have to be summed in order to obtain the total van der Waals interaction. For all the calculations presented here, I always assumed the interacting objects to be homogeneous and continuous objects. The hypothesis of homogeneity allows taking the factor  $\beta$  as a constant for the interaction of two specific bodies, while sums over energies can be replaced by integrals imposing the continuity. Additionally, I supposed that the potentials are simply additive and

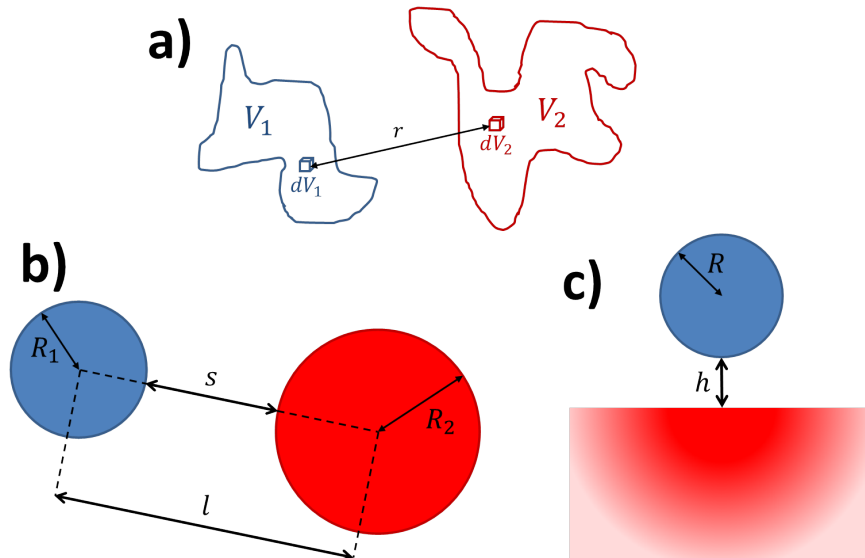


Figure 4.4: **a)** Representation of two bodies of generic shape, indicating the distance  $r$  between two random infinitesimal volumes  $dV_1$  and  $dV_2$ . **b)** Scheme for the sphere-sphere interaction. **c)** Scheme for the sphere-surface interaction.

## Chapter 4. Quantitative AFM height measurements

---

that retarded potential effects could be ignored. Therefore, the total van der Waals potential energy can be calculated as:

$$U_{1,2} = -\beta \int_{V_1} dV_1 \int_{V_2} dV_2 \frac{Q_1 Q_2}{r^6} \quad (4.2)$$

where  $Q_1$  and  $Q_2$  are the density of interacting elements in the volumes  $dV_1$  and  $dV_2$  respectively, while  $V_1$  and  $V_2$  are the total volumes of the two objects (see fig. 4.4 a)). By definition, the Hamaker constant  $A_H$  of the interaction is:

$$A_H = \pi^2 \beta Q_1 Q_2 \quad (4.3)$$

where the factor  $\pi^2$  is included in the definition for historical reasons. Hamaker [19] found analytical solutions for sphere-sphere van der Waals interaction, making the same hypotheses I made in this discussion. Sphere-sphere van der Waals potential energy is:

$$U_{sph,sph}(s) = -\frac{A_H}{6} \left[ \frac{2R_1 R_2}{s^2 + 2s(R_1 + R_2)} + \frac{2R_1 R_2}{s^2 + 2s(R_1 + R_2) + 4R_1 R_2} + \ln \left( \frac{s^2 + 2s(R_1 + R_2)}{s^2 + 2s(R_1 + R_2) + 4R_1 R_2} \right) \right] \quad (4.4)$$

where  $R_1$  and  $R_2$  are the two radii and  $s$  is the separation between the two spheres, whose centers are at a distance  $l = s + R_1 + R_2$  as shown in fig. 4.4 b). If one of the two spheres is much bigger than the other, eq. (4.4) can be simplified assuming  $R_2 \gg R_1$  and it becomes:

$$U_{sph,surf}(h) = -\frac{A_H}{6} \left[ \frac{R}{h} + \frac{R}{2R+h} + \ln \left( \frac{h}{2R+h} \right) \right] \quad (4.5)$$

which describes the interaction between a sphere and a medium filling half of the space and bound by a plane (in this chapter, I will usually refer to this semi-infinite medium calling it simply "surface"). Here  $R$  is the radius of the small sphere and  $h$  is the separation between the sphere and the flat surface (fig. 4.4 c)).

### 4.2.2 Modeling the tip as a sphere

Tips used as probe in AFM have different geometries and dimensions, depending on the experiment to realize. Tips for high resolution need a sharp apex to limit convolution effects on images. Conical and pyramidal tips are the most used geometries. Mikromasch silicon tips that I used in my experiments have a conical shape, with a full cone angle equal to  $40^\circ$ .

## 4.2. Tip and DNA models for the AFM height calculations

DLC tips consist in carbon whiskers grown on the apex of conventional tips and as a first approximation they can be interpreted as cones with a very small full cone angle (see fig. 2.6). In principle, the calculation of the total tip-sample interaction must include contributions from all the volume of the tip. Giessibl [8] reported mathematical formulas for calculating the van der Waals potential energy between various kinds of tips (including conical, pyramidal and parabolic tips) with a flat surface. Argento and French [70] found an analytical solution for the van der Waals force between a conical tip with a spherical apex and a sphere. To my knowledge, analytical solutions for the van der Waals interaction of objects with these geometries and spheres or cylinders have never been reported. Also numerical integrations to calculate these interactions appear difficult to realize. Several authors [18, 62, 71] modeled the tip as a simple sphere representing the tip apex. The rationale for this choice is the fact that van der Waals forces have a  $r^{-6}$  decay as shown in eq. (4.1) and contributions of parts of the tip far from the sample are negligible to a large extent.

For all the work presented in this chapter I assumed the spherical model for the tip. This assumption allowed me to easily calculate van der Waals interactions with surfaces and with the two different DNA models (infinite cylinder and linear row of spheres). The sphere-cylinder interaction was determined making numerical integrations (see section 4.2.3 for details). In this section I will analyze the accuracy of this tip modeling, comparing it with the model of the conical tip with spherical apex.

According to [70], the van der Waals force between a surface and a cone with spherical apex (see fig. 4.5) is:

$$F_{c/s,surf}(s) = A_H \left\{ \frac{r^2 [1 - \sin(\gamma)] [r \sin(\gamma) - s \sin(\gamma) - r - s]}{6s^2 [r + s - r \sin(\gamma)]^2} + \frac{\tan(\gamma) [s \sin(\gamma) + r \sin(\gamma) + r \cos(2\gamma)]}{6 \cos(\gamma) [s + r - r \sin(\gamma)]^2} \right\} \quad (4.6)$$

where  $s$  is the separation with respect to the surface,  $r$  is the radius of the spherical apex and  $\gamma$  is the half cone angle. The sphere-surface force can be obtained from eq. (4.5) in this way:

$$F_{sph,surf}(s) = -\partial_s U_{sph,surf}(s) \quad (4.7)$$

The two models have to be quantitatively compared in order to check the validity of the spherical approximation. For the comparison, I assumed the same radius  $r$  for the cone apex and the sphere. Calculations were done for the two types of tips (silicon and DLC) that I used in this thesis. I set  $r = 10$  nm,  $\gamma = 20^\circ$  for the silicon tip and  $r = 2$  nm,  $\gamma = 5^\circ$  for DLC tips. The sphere-surface force and the cone with spherical apex-surface force have been plotted as a function of the separation in fig. 4.6. Forces were normalized with respect to the Hamaker constant  $A_H$  in order to show a trend depending only on the geometry of the interacting bodies. In both cases the curves relative to the two models are almost exactly superposed.

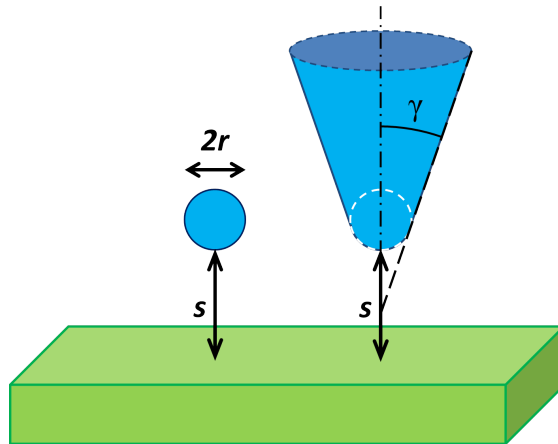


Figure 4.5: Representation of a sphere and of a cone with spherical apex at separation  $s$  from a surface.

Frequency shift vs. separation curves were calculated from forces using eq. (1.36). The resonant frequency  $f_0$  and the spring constant  $k$  of the cantilever had to be set to calculate the frequency shift. Nominal values of these parameters are shown in tab. 2.1 and they are different for the DLC and silicon tips. I assumed  $f_0 = 325$  kHz and  $k = 40$  N/m for the DLC tip cantilever. I chose the parameters of the Mikromasch NSC35 B cantilever (see fig. 2.6) for calculations concerning the silicon tip and I set  $f_0 = 315$  kHz and  $k = 14$  N/m. Results shown

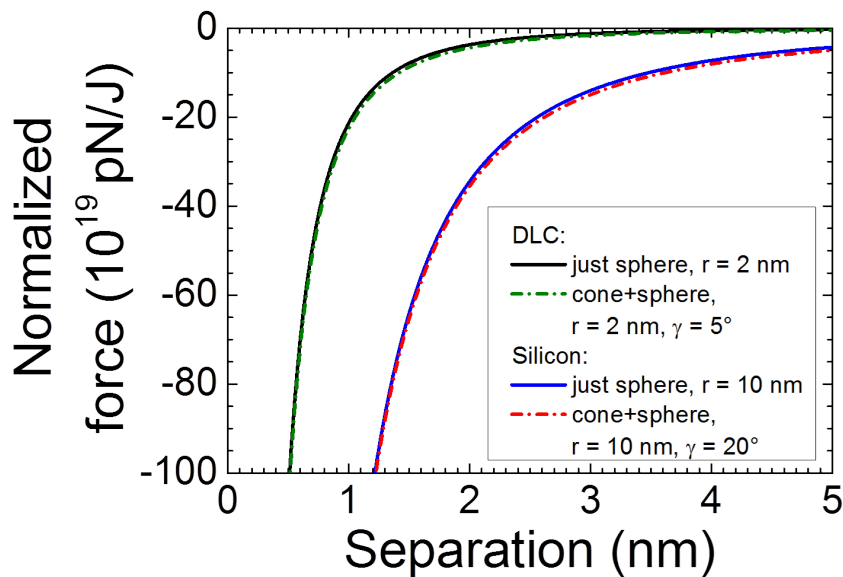


Figure 4.6: Normalized force vs. separation curves are plotted. Continuous lines represent the sphere model and dot-dashed lines the cone with spherical apex model. The sphere and the spherical apex have the same radius  $r$ . The black and the green line simulate a DLC tip, while the blue and the red line simulate a silicon tip.

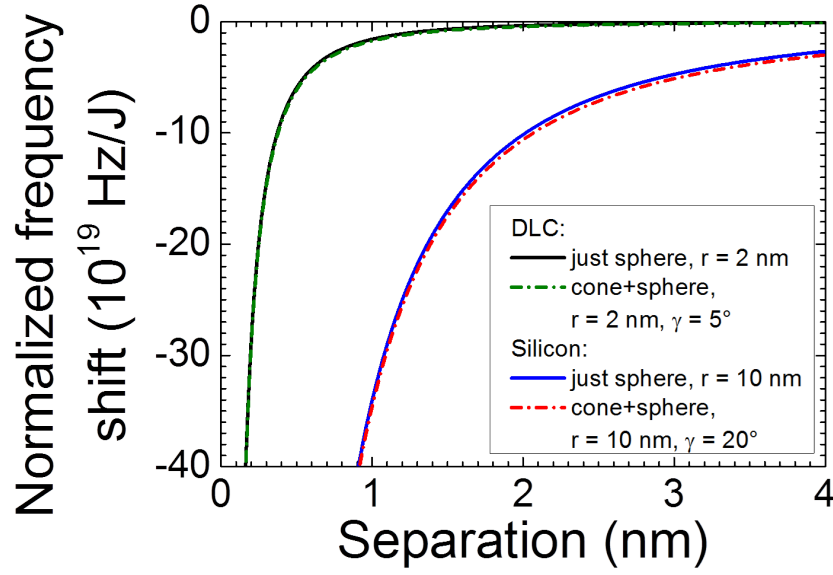


Figure 4.7: Normalized frequency shift vs. separation curves are plotted. The color code and the line style are identical to fig. 4.6. I set  $f_0 = 325$  kHz and  $k = 40$  N/m for the DLC tip,  $f_0 = 315$  kHz and  $k = 14$  N/m for the silicon tip.

in fig. 4.7 again confirm the validity of the spherical approximation of the tip.

The main topic of this chapter is the explanation of the DNA height measured in FM AFM, which is smaller than the predicted value of 2 nm circa, as an effect of the different interaction of the tip with DNA and with the substrate. As it will be explained later in more detail, the calculation of the “apparent” height was made fixing a  $\Delta f$  value and evaluating the tip separation from the substrate plane when the tip is over the DNA molecule and over the bare substrate. The apparent height was then determined as the difference between these two values. Therefore, it is important to quantify the error in the prediction of the separation made assuming the simplified spherical model and to compare it with the calculated apparent DNA height.

First of all, I evaluated the tip separation from the surface for both the models and for both the types of tips I used in experiments (DLC and silicon tips). It was necessary to introduce at this point the Hamaker constant  $A_H$  in the calculations in order to make a quantitative comparison. I assumed the value  $A_H = 1.35 \times 10^{-19}$  J reported by [62] for the silicon-mica van der Waals interaction, while for the DLC-mica interaction I set  $A_H = 1.7 \times 10^{-19}$  J which is the diamond-mica Hamaker constant in vacuum reported by [68].

The frequency shift curve  $\Delta f(s)$  was calculated for both models and tips taking into account the proper  $A_H$ . Then the inverse function  $s(\Delta f)$  was determined for each  $\Delta f(s)$  curve. The difference  $s_{c/s,surf}(\Delta f) - s_{sph,surf}(\Delta f)$  is plotted both for DLC and silicon tips as a function of the frequency shift in fig. 4.8. For each of two plots shown in this figure, the frequency shift range was adapted to the typical set point values used for the two different tips, that is between -1 and -10 Hz for DLC tips and between -10 and -40 Hz for silicon tips. In both the

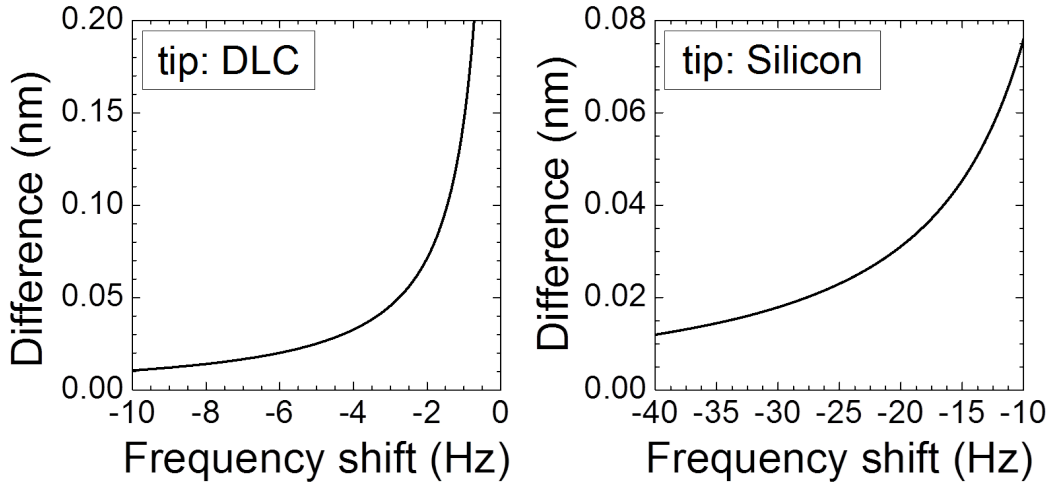


Figure 4.8: Difference between the tip-surface separation  $s(\Delta f)$  calculated with the two tip models. DLC tip parameters:  $A_H = 1.7 \times 10^{-19}$  J,  $f_0 = 325$  kHz,  $k = 40$  N/m,  $r = 2$  nm,  $\gamma = 5^\circ$ . Silicon tip parameters:  $A_H = 1.35 \times 10^{-19}$  J,  $f_0 = 315$  kHz,  $k = 14$  N/m,  $r = 10$  nm,  $\gamma = 20^\circ$ .

plots, the difference becomes smaller at lower values of  $\Delta f$ . This is expectable because the tip-surface distance is smaller when the frequency detuning increases, and therefore the part of the tip nearer to the surface becomes more and more dominant on the total interaction. The difference between the separation calculated with the different models was less than 0.1 nm in all the considered  $\Delta f$  range for the silicon tip, while this difference was less than 0.1 nm for the DLC tip when  $\Delta f < -1.5$  Hz.

As a next step, I tried to make a similar evaluation for the error in the calculation of the tip-DNA separation when using the spherical model. Unfortunately, there are not models for the van der Waals interaction between a cone with spherical apex and any object which would represent a simplified DNA shape, such as a cylinder or a row of sphere. Moreover, there is not an extensive literature on the DNA Hamaker constant of interaction with different tips. To my knowledge, the only evaluation in this sense was done by Santos and coworkers [62] who reported a value of  $A_H$  for the DNA-silicon tip van der Waals interaction equal to  $0.3 \div 0.4 \times 10^{-19}$  J, measured through AM AFM experiments in air.

For these reasons, I decided to perform a rough evaluation of this error in the following way. I considered two situations:

1. the interaction of a given tip with a DNA molecule;
2. the interaction of a given tip with an infinite surface having a surface-tip Hamaker constant equal to the DNA's one.

Due to geometrical reasons, the separation at a given  $\Delta f$  between the tip and the DNA will be smaller than the separation at the same  $\Delta f$  between the same tip and the surface. This is valid for both the models of tip and for all the  $A_H$  values. It is reasonable to think that the

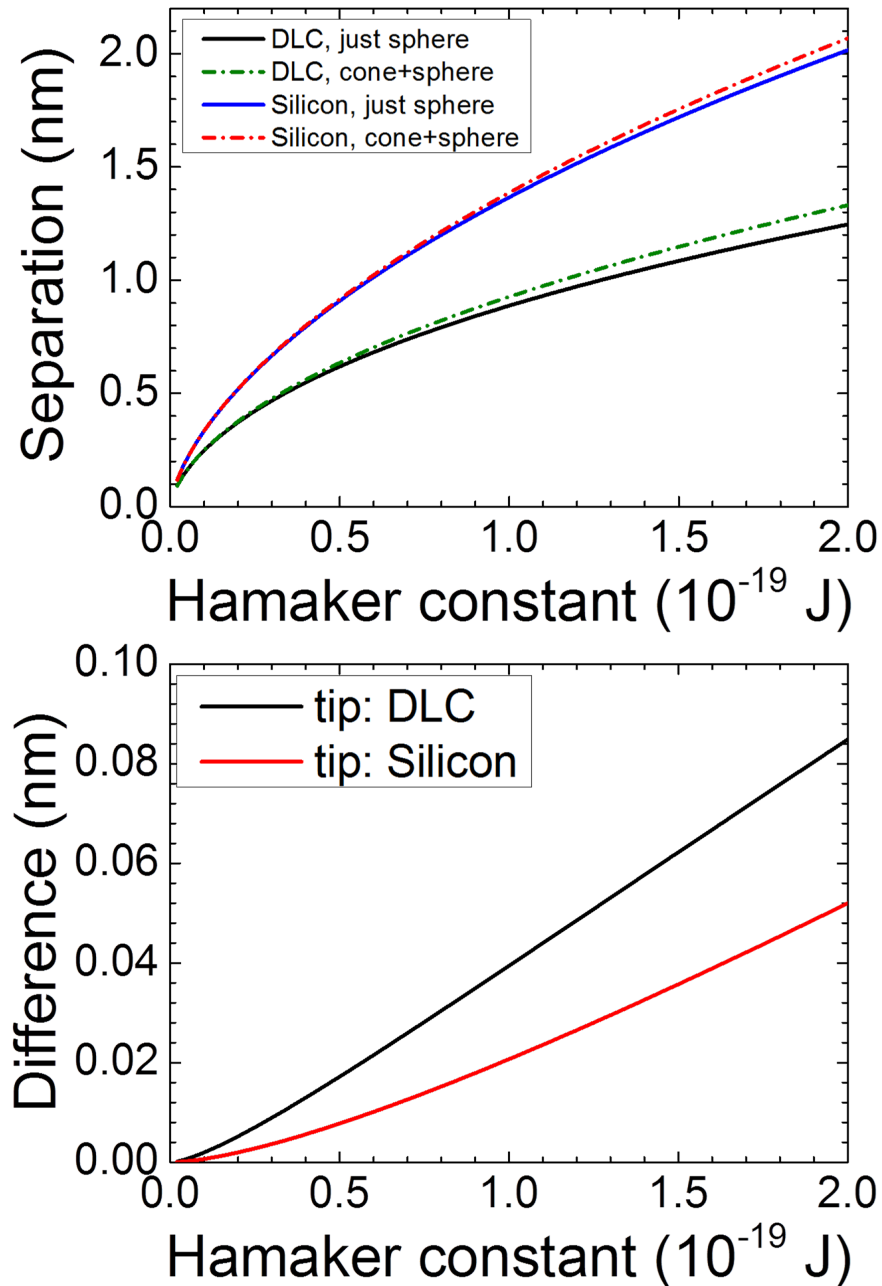


Figure 4.9: On the top, tip-surface separation curves as a function of  $A_H$  are shown. The tip-surface separations for a modeled DLC tip are represented in black (sphere model) and green (cone with spherical apex model); parameters:  $r = 2$  nm,  $\gamma = 5^\circ$ ,  $f_0 = 325$  kHz,  $k = 40$  N/m,  $\Delta f = -2$  Hz. The separations for a modeled silicon tip are represented in blue (sphere model) and red (cone with spherical apex model); parameters:  $r = 10$  nm,  $\gamma = 20^\circ$ ,  $f_0 = 315$  kHz,  $k = 14$  N/m,  $\Delta f = -20$  Hz. On the bottom, the differences between the separations obtained with the two tip models are plotted. The black curve is the result for the DLC tip, the red curve the one for the silicon tip. Parameters for both DLC and silicon tips are the same than the ones used for the plot on the top.

difference  $s_{c/s,DNA}(\Delta f) - s_{sph,DNA}(\Delta f)$  (relative to the tip-DNA interaction) would be of the same order of magnitude or smaller than the difference  $s_{c/s,surf}(\Delta f) - s_{sph,surf}(\Delta f)$  (relative to the tip-surface interaction). In this sense, the difference between the tip-surface separations obtained with the two tip models can be considered as an upper limit to the difference which would be obtained with DNA.

Fig. 4.9 shows the separation as a function of  $A_H$  for both the tip models. Calculations were done assuming again  $r = 2$  nm,  $\gamma = 5^\circ$  in order to simulate the shape of a DLC tip and  $r = 10$  nm,  $\gamma = 20^\circ$  for a silicon tip. The frequency shift was set to -2 Hz for the DLC tip and to -20 Hz for the silicon tip. As it can be seen in the bottom of fig. 4.9, the assumption of the spherical model gives an underestimation of the tip-surface separation smaller than 0.1 nm in all the considered range of  $A_H$ , whose typical values are close to  $10^{-19}$  J according to the literature.

In conclusion, it is reasonably correct to approximate the AFM tip as a sphere representing the tip apex in the theoretical framework of my calculations. The spherical approximation gives an underestimation of the tip-surface separation of less than 0.1 nm for both DLC and silicon tips in almost all the typical  $\Delta f$  range of the two tips. In a similar way, an upper limit to the underestimation of tip-DNA separation have been fixed to 0.1 nm too. These values are significantly small with respect to the real DNA diameter and the measured DNA height.

### 4.2.3 Cylinder vs. sphere van der Waals interaction

Here I present a discussion about the calculation of the van der Waals interaction between an infinitely long cylinder and a sphere. I partly based my calculation on the work published by Montgomery and coworkers [72], that to my knowledge is the only work reporting an analytical solution to this problem. I will show the limits related to the applicability of their solution and the details of the numerical calculations that I performed to determine the total van der Waals interaction between the aforementioned bodies.

For the calculation of the van der Waals interaction between a sphere and an infinitely long cylinder, it is convenient to start from the potential energy  $du_{P,cyl}$  between one point  $P$  of the sphere with an infinitesimal volume of cylinder  $dV_{cyl}$ . Accordingly with [72], I chose a cylindrical system of coordinates  $(r, z, \phi)$  centered in  $P$ . This potential energy can be written as:

$$du_{P,cyl} = -\frac{Q_{cyl}\beta}{(r^2 + z^2)^3} dV_{cyl} = -\frac{Q_{cyl}\beta}{(r^2 + z^2)^3} r dr d\phi dz \quad (4.8)$$

where  $Q_{cyl}$  is the density of elements in  $dV_{cyl}$  (see fig. 4.10 for the meaning of all the other variables). Eq. (4.8) can be integrated without approximations both in  $\phi$  and  $z$ , obtaining [72]:

$$dU_{P,cyl} = -\frac{3}{4} \pi Q_{cyl}\beta \frac{1}{r^4} \arccos\left(\frac{r^2 + H^2 - R_{cyl}^2}{2rH}\right) dr \quad (4.9)$$

where  $H$  is the distance between  $P$  and the cylinder axis. The infinitesimal potential energy  $dU_{P,cyl}$  represents the interaction between  $P$  and a cylindrical surface with radius  $r$  and



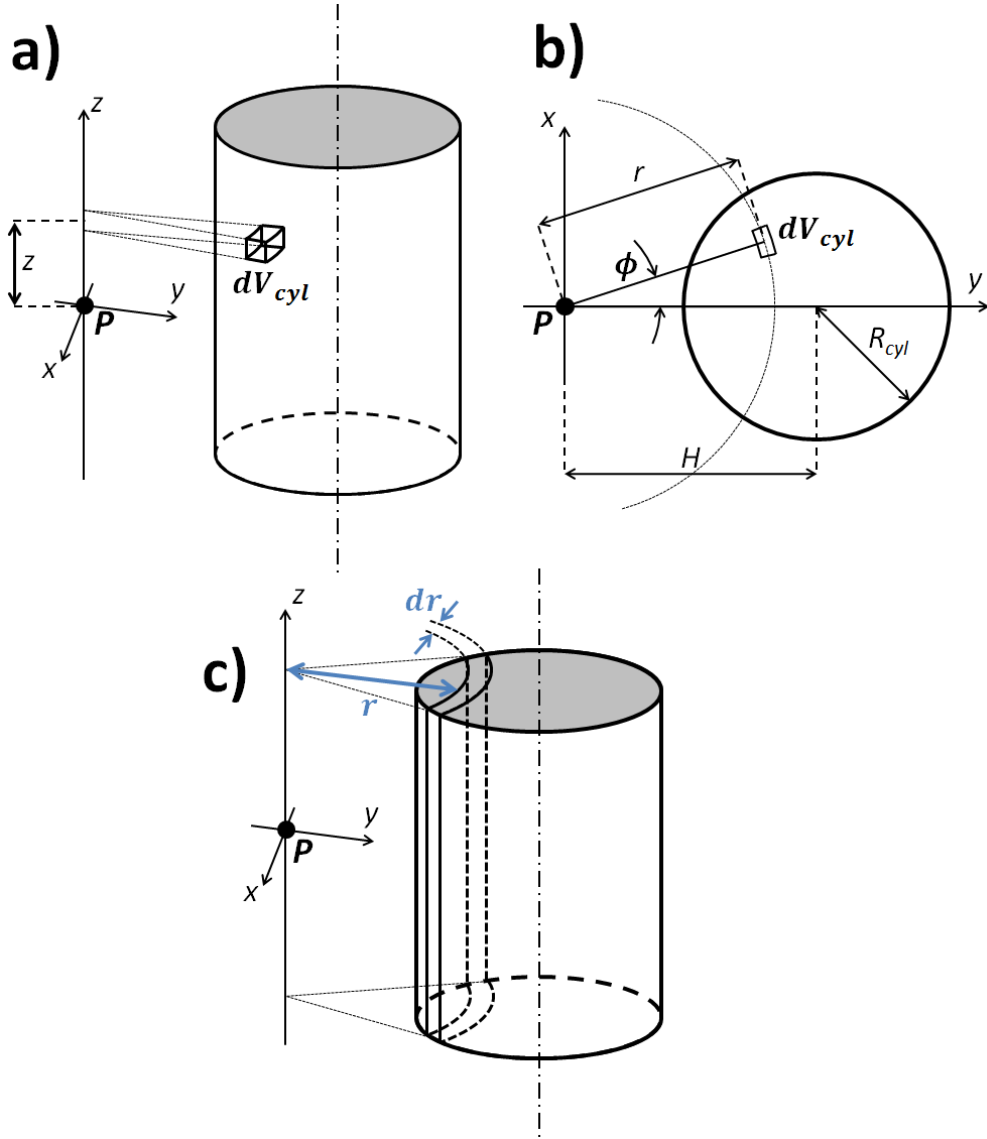


Figure 4.10: **a)** Lateral view of the (infinitely long) cylinder interacting with the point  $P$ . **b)** View of a section of the same cylinder. **c)** Representation of the cylindrical cut whose interaction with the point  $P$  is described by eq. (4.9).

thickness  $dr$ , concentric with the  $z$  axis, that cuts the cylinder volume (see fig. 4.10 c)). A first approximation was done in [72] at this point, that is to make this development in series:

$$\arccos(x) \simeq \frac{\pi}{2} - \left( x + \frac{x^3}{6} + \frac{3x^5}{40} + \frac{15x^7}{336} \right) \quad (4.10)$$

where  $x = \frac{r^2 + H^2 - R_{cyl}^2}{2rH}$ . This approximation is valid only for  $\arccos(x) \approx 0$ , that is for  $x \approx 1$ . Considering that  $H > R_{cyl}$  and  $r \in [H - R_{cyl}, H + R_{cyl}]$ , evidently the approximation is correct

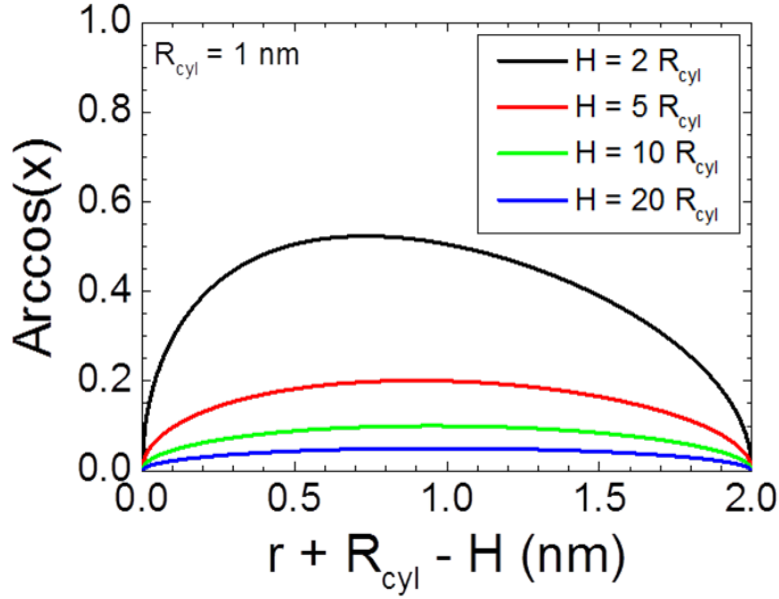


Figure 4.11: The function  $\arccos(x)$  where  $x = \frac{r^2 + H^2 - R_{cyl}^2}{2rH}$  was plotted as a function of  $r$ .  $R_{cyl}$  was fixed at 1 nm. Curves calculated assuming different values of  $H$  are shown. The  $\arccos(x)$  is small for all the values of  $r$  only if  $H$  is large with respect to  $R_{cyl}$ .

only if  $H$  is large with respect to  $R_{cyl}$  and therefore when the point  $P$  is far from the cylinder. This conclusion is confirmed by fig. 4.11, where  $\arccos(x)$  is plotted as a function of  $r$  for different values of  $H$ , assuming  $R_{cyl} = 1$  nm.

The abovementioned approximation allows integrating eq. (4.9) over the volume of the cylinder. The approximated total van der Waals potential energy for the point  $P$ -cylinder interaction was then calculated in [72]:

$$\begin{aligned}
 U_{P,cyl}^{approx} \approx & -\frac{3}{4} \pi Q_{cyl} \beta \left\{ \frac{\pi}{6(H - R_{cyl})^3} - \frac{\pi}{6(H + R_{cyl})^3} - \frac{3H - R_{cyl}}{8(H - R_{cyl})^3 H} + \right. \\
 & + \frac{3H + R_{cyl}}{8(H + R_{cyl})^3 H} + \frac{12H^3 + 36HR_{cyl}^2 - 12R_{cyl}^3 - 36H^2R_{cyl}}{144H^3(H + R_{cyl})^3} \ln\left(\frac{H - R_{cyl}}{H + R_{cyl}}\right) + \\
 & \left. \frac{-29H^3 + 21HR_{cyl}^2 - 11R_{cyl}^3 + 3H^2R_{cyl}}{144H^3} \left[ \frac{1}{(H - R_{cyl})^3} - \frac{1}{(H + R_{cyl})^3} \right] \right\} \quad (4.11)
 \end{aligned}$$

## 4.2. Tip and DNA models for the AFM height calculations

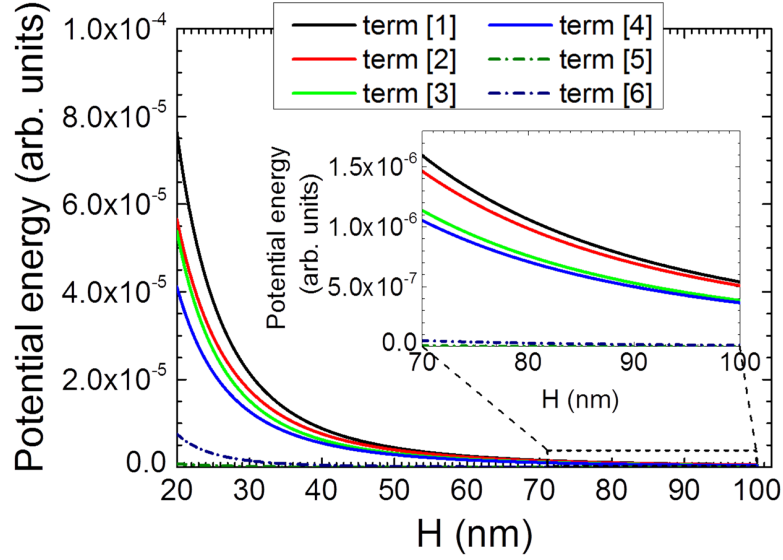


Figure 4.12: Dependence on  $H$  of each of the terms in eq. (4.11) (in absolute value). The value of  $R_{cyl}$  has been set to 1 nm. In the inset, a magnification of the plot for  $H \in [70, 100]$ .

where each term in parenthesis has been labeled with a number. Fig. 4.12 shows the relative weight of each term as a function of  $H$ . Here again I set  $R_{cyl} = 1$  nm. It is evident that the terms [5] and [6] are negligible with respect to the others in all the considered range, while the other terms are of the same order of magnitude.

Eq. (4.11) is an approximated evaluation of the van der Waals interaction between the point  $P$  and the infinite cylinder. The point  $P$  can be considered as the position of the generic infinitesimal volume  $dV_{sph}$  of the sphere, to which a density  $Q_{sph}$  can be assigned. The total sphere-cylinder potential energy has to be calculated making an integral over the volume of the sphere, that is:

$$U_{sph,cyl}^{approx} = Q_{sph} \int_{V_{sph}} U_{P,cyl}^{approx} dV_{sph} \quad (4.12)$$

However, further calculations in [72] to determine the whole sphere-cylinder interaction took into account only the terms [1] and [2]. In conclusion, on the basis of what presented here I can affirm that the analytical solution found by Montgomery et al. in [72] fails to describe the correct sphere-cylinder interaction at short distances and give a very qualitative result at large distances. Therefore I decided to perform numerical integrations in order to obtain a more correct evaluation of the point  $P$ -cylinder interaction. I used the software Wolfram Mathematica 8 to do these calculations.

I started again from eq. (4.9) which is not approximated. I defined  $r_i$  as  $H - R_{cyl} + i\Delta r$ , where  $i$  is an integer and  $\Delta r$  is the step of integration. For all calculations I set  $\Delta r = 0.001$  nm. The

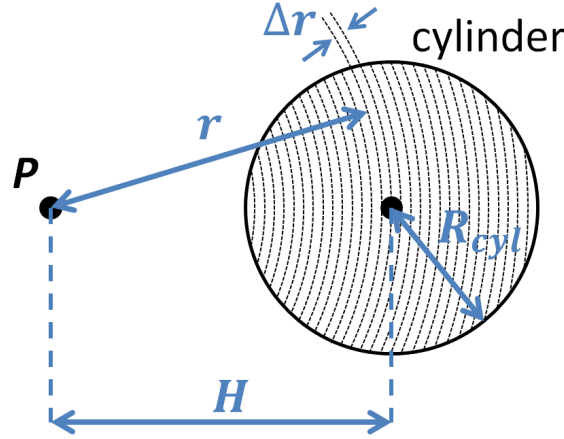


Figure 4.13: This sketch summarizes the meaning of the variables used in eq. (4.13). On the right of the image a top view of the cylinder is drawn.

point  $P$ -cylinder potential energy was calculated as:

$$\bar{U}_{P,cyl}(H, R_{cyl}) = -\frac{3}{4} \sum_{i=0}^{(2R_{cyl}/\Delta r)-1} \frac{1}{r_i^4} \arccos\left(\frac{r_i^2 + H^2 - R_{cyl}^2}{2r_i H}\right) \Delta r \quad (4.13)$$

where the notation  $\bar{U}_{P,cyl}$  was used to indicate the potential energy normalized with respect to the factor  $\pi\beta Q_{cyl}$ . The latter is just a multiplicative factor which is included in the definition of the Hamaker constant  $A_H$  (eq. (4.3)) and it can be ignored for the moment. Using eq. (4.13), numerical values of  $\bar{U}_{P,cyl}$  have been calculated varying both the distance of the point  $P$  and the supposed radius of the cylinder.

The next step was integrating over the volume of the sphere, whose radius was defined as  $R_{sph}$ . I fixed as reference the system of Cartesian coordinates described in fig. 4.14, having its origin on the cylinder axis. The  $y$  axis corresponds to the cylinder axis and the  $z$  axis was taken perpendicular to it and passing through the sphere center. A generic point inside the sphere has coordinates  $(x, y, z)$  and the coordinates of center of the sphere are  $(0, 0, z_0)$ .

For each point inside the sphere, the coordinate  $z$  varies in the interval  $[z_0 - R_{sph}, z_0 + R_{sph}]$ . For any given  $z$ , the coordinate  $x$  lies in the interval  $[-\sqrt{R_{sph}^2 - (z - z_0)^2}, \sqrt{R_{sph}^2 - (z - z_0)^2}]$ . Therefore, fixed a couple of values  $x$  and  $z$ , the values of  $y$  that lie inside the sphere are comprised in the range  $[-\sqrt{R_{sph}^2 - (z - z_0)^2 - x^2}, \sqrt{R_{sph}^2 - (z - z_0)^2 - x^2}]$ . According to the directions of the axis, if a couple of values  $x^*$  and  $z^*$  is fixed all the points  $(x^*, y, z^*)$  are at the same distance  $H^* = \sqrt{x^{*2} + z^{*2}}$  with respect to cylinder axis. Moreover, also the points  $(-x^*, y, z^*)$  are at the same distance  $H^*$  due to the symmetry of the system. Taking into account that the cylinder is infinitely long, the relation expressed in eq. (4.13) is invariant for translations along the  $y$  axis. This means that the integration on  $y$  can be avoided and that the element of volume of the sphere can be defined as:

$$dV_{sph} = 4 dx dz \sqrt{R_{sph}^2 - (z - z_0)^2 - x^2} \quad (4.14)$$

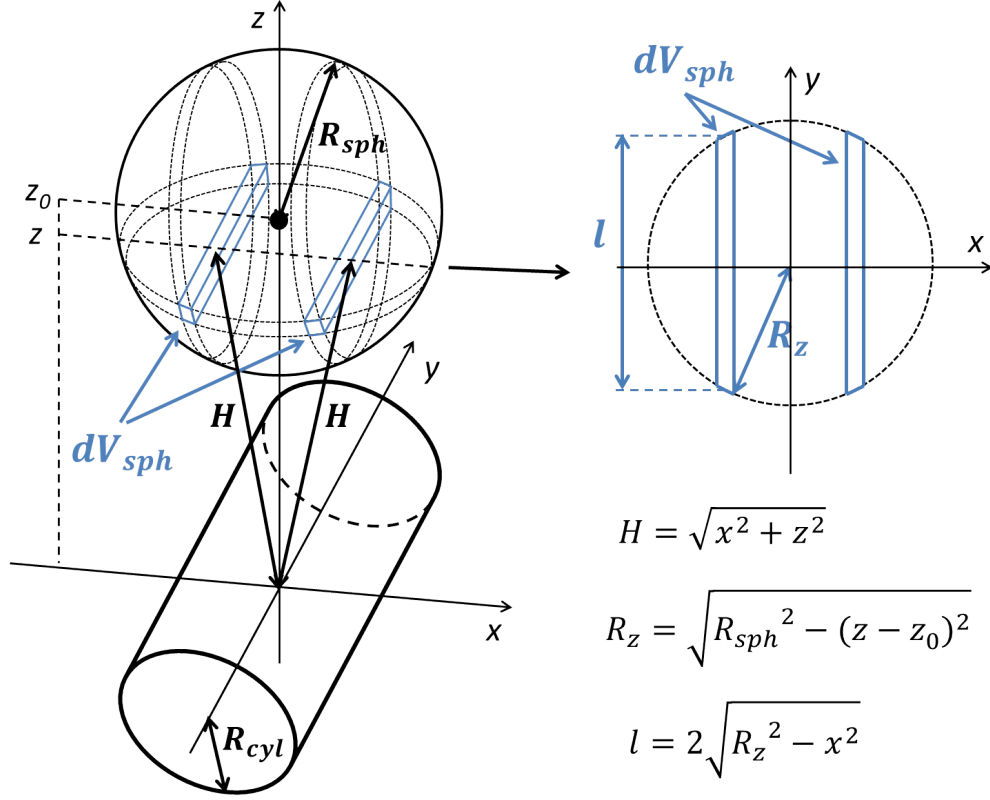


Figure 4.14: On the left, a representation of the sphere and of the (infinitely long) cylinder, showing the element of volume  $dV_{sph}$ . On the right, a top view of the layer of the sphere between  $z$  and  $z + \Delta z$ .

The element of volume  $dV_{sph}$  is represented in fig. 4.14 and corresponds to the ensemble of the two blue segments. The total sphere-cylinder van der Waals potential energy was then calculated in this way:

$$\begin{aligned} \bar{U}_{sph,cyl}(z_0, R_{cyl}, R_{sph}) = & \frac{4}{\pi} \sum_{i=-N}^{N-1} \sum_{j=0}^{M_i-1} \bar{U}_{P,cyl} \left( \sqrt{x_j^2 + z_i^2}, R_{cyl} \right) \times \\ & \times \sqrt{R_{sph}^2 - (z_i - z_0)^2 - x_j^2} \Delta x \Delta z \end{aligned} \quad (4.15)$$

where:

$$z_i = z_0 + i\Delta z; \quad x_j = j\Delta x; \quad N = \frac{R_{sph}}{\Delta z}; \quad M_i = \frac{\sqrt{R_{sph}^2 - (z_i - z_0)^2}}{\Delta x}.$$

$\bar{U}_{sph,cyl}$  is a normalized value of the total potential energy, being:

$$U_{sph,cyl} = \pi^2 \beta Q_{sph} Q_{cyl} \bar{U}_{sph,cyl} = A_H \bar{U}_{sph,cyl} \quad (4.16)$$

Both  $\Delta x$  and  $\Delta z$  were set to 0.01 nm for all calculations. In order to verify the accuracy of my evaluation of the sphere-cylinder potential energy, I compared it to potential energies relative to the van der Waals interaction of bodies with different geometries, for which an analytical solution exists. For this test, I considered the sphere-sphere and the sphere-surface potential energy described by eqs. (4.4) and (4.5) respectively. I defined the normalized potential energies  $\bar{U}_{sph,sph}$  and  $\bar{U}_{sph,surf}$  dividing  $U_{sph,sph}$  and  $U_{sph,surf}$  by the Hamaker constant  $A_H$ . In this way, the potential energies depended only on the geometry of the interacting bodies. I defined as  $S_1$  a sphere having radius  $R_{sph,1}$  and I compared the van der Waals interactions:

1. of  $S_1$  with a second sphere  $S_2$  with radius  $R_{sph,2}$  ( $\bar{U}_{S_1,S_2}$ );
2. of  $S_1$  with a cylinder with radius  $R_{cyl}$  ( $\bar{U}_{S_1,cyl}$ );
3. of  $S_1$  with a semi-infinite medium bound with a flat surface ( $\bar{U}_{S_1,surf}$ ).

Given a certain separation  $s$ , it is evident that  $\bar{U}_{S_1,cyl}(s) > \bar{U}_{S_1,S_2}(s)$  if  $R_{cyl} = R_{sph,2}$ . Moreover,  $\bar{U}_{S_1,cyl}(s)$  must approach  $\bar{U}_{S_1,surf}(s)$  when  $R_{cyl}$  goes to infinite.

Calculations were done fixing  $R_{sph,1} = R_{sph,2} = 2$  nm and evaluating the sphere-cylinder potential energy for  $R_{cyl} = 2, 5$  and 10 nm. Results are shown in fig. 4.15. The expected behavior of the potential energies is perfectly observed both at large and at short separations. I made the same test using the approximated sphere-cylinder van der Waals potential energy calculated in [72] (eq. (60) in that article). Fig. 4.16 shows results in this case and as expected the model completely failed in the evaluation of the interaction.

In conclusion, the numerical integrations that I made correctly describe the sphere-cylinder van der Waals interaction for all the values of the sphere-cylinder separation. The radius of the cylinder will be set to  $R_{cyl} = 1$  nm in order to simulate the theoretical radius of a DNA molecule. The radius of the sphere can be adapted to simulate interaction of a DNA molecule both with a DLC tip and with a silicon tip.

### 4.2.4 Chain of spheres vs. sphere van der Waals interaction

The model presented in section 4.2.3 simulates the pseudo-cylindrical shape of the DNA molecule frequently observed when making FM AFM imaging in dehydrated conditions. Experiments discussed in section 3.4.4 showed that it was possible to observe the B-form DNA double helix periodicity along segments of DNA molecules when using DLC tips. This result was never obtained with silicon tips. A possible explanation could be that larger silicon tips interact with a wider portion of molecule. Therefore the silicon tip-DNA interaction depends more on the average geometry of the molecule than on the local details. Inversely, the interaction of sharper DLC tips with DNA molecules is more localized, giving rise to a

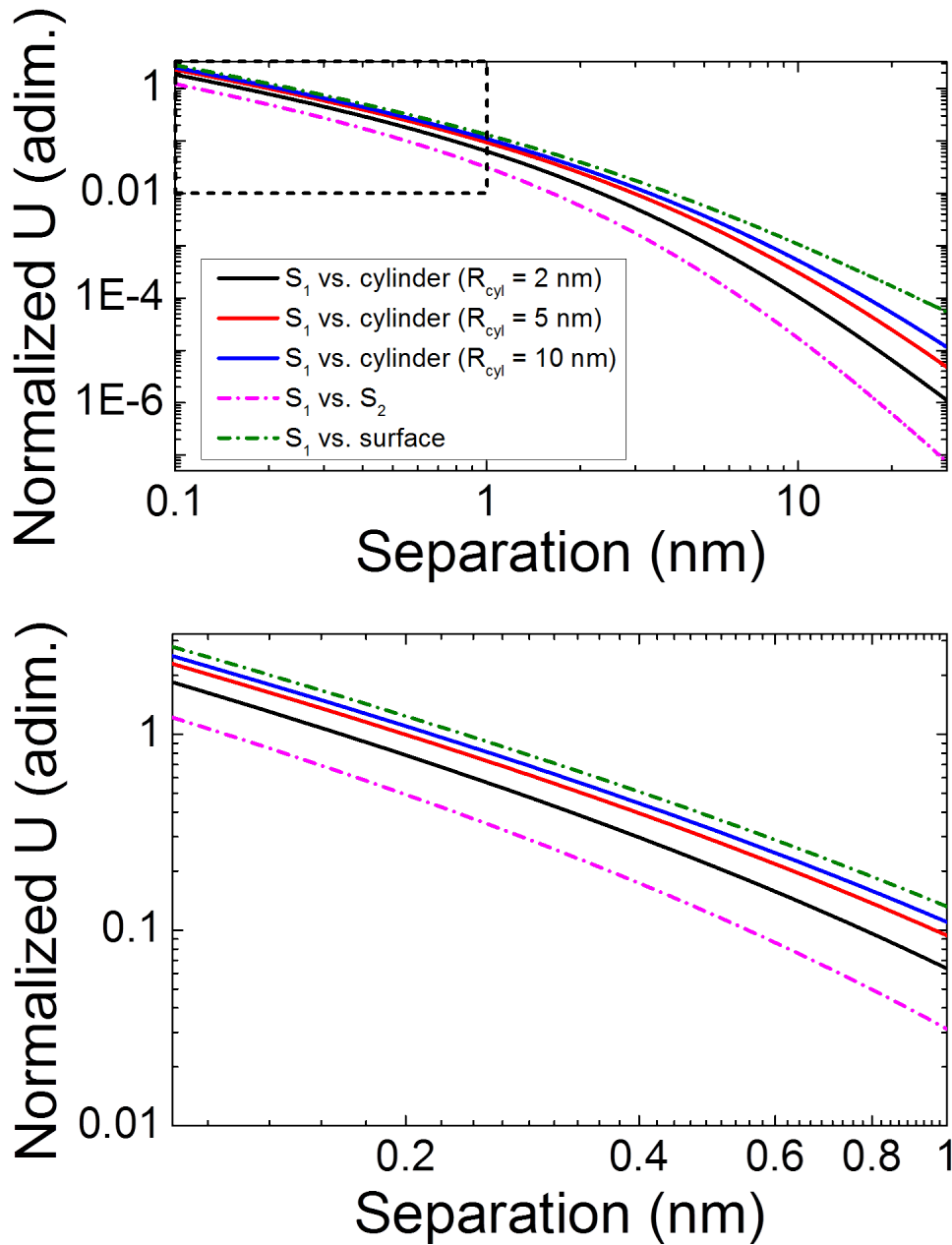


Figure 4.15: Comparison among different normalized potential energies (in absolute values). They are relative to the interaction of a sphere  $S_1$  ( $R_{sph,1} = 2$  nm) with: a 2 nm radius cylinder (black line); a 5 nm radius cylinder (red line); a 10 nm radius cylinder (blue line); a 2 nm radius sphere  $S_2$  (purple line); a flat semi-infinite medium (green line). The sphere-cylinder potential energies have been calculated using eq. (4.15). On the top: normalized potential energy vs. separation. On the bottom: magnification of the area at small separation marked with a dashed rectangle in the top image.

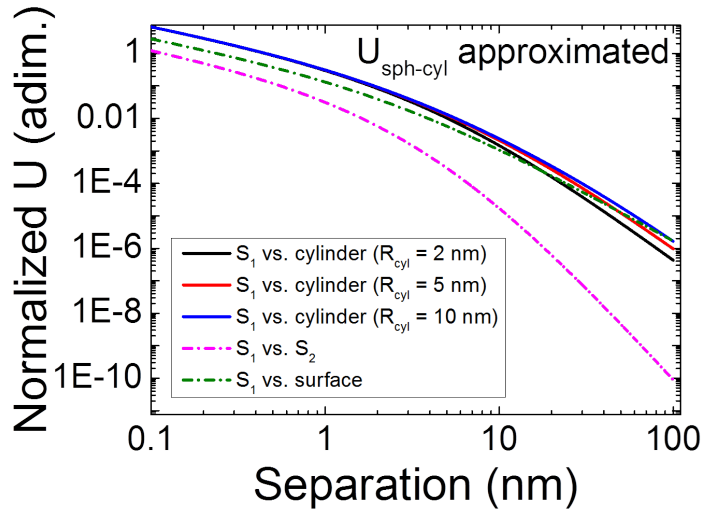


Figure 4.16: This figure is analogous to the top image of fig. 4.15, but the sphere-cylinder potential energies have been calculated using the approximated formula in [72] (eq. (60) in that article).

better groove contrast. In order to test this hypothesis, I created an alternative model for the DNA molecule which exhibited a corrugation along the DNA axis. I chose to represent the DNA molecule as a linear chain of contiguous spheres. The main advantage of this model was that the sphere-sphere van der Waals potential energy was known (eq. (4.4)) and it would have been relatively easy to check the difference between contrasts on the top of the molecule obtained with the two kind of tips. I used this model also to give an evaluation of the DNA height alternative to the one calculated with the cylindrical model. This model is basically the same used to study the groove contrast in spectroscopy measurements and explained in section 3.6.4. The total van der Waals potential energy between the sphere representing the tip and the chain of spheres representing the DNA molecule is shown in eq. (3.5). Also in this case, I supposed a chain of 20 spheres having a radius equal to 1 nm.

### 4.3 Results of calculations

In this section I will present the results of the calculations made using both the models of the DNA molecule. The results about the calculated DNA height in the two cases will be discussed, showing that the DNA height in FM AFM experiments is correlated to the dimensions and to the material of the AFM tip used. Then an explanation of the groove contrast visible over the DNA molecules in FM AFM imaging will be given. In particular, it will be discussed why it was possible to observe a corrugation compatible with the DNA double helix periodicity only with sharp DLC tips. Finally, I will show how the method for the prediction of the FM AFM height of a DNA molecule described in this chapter can be extended to other biological molecules, having dimensions comparable with the ones of a DNA molecule.



#### 4.3.1 Calculation of the DNA height in FM AFM

The two models of the DNA molecule were used to calculate the FM AFM height of a DNA molecule. To do this, simulations of FM AFM imaging experiments were done. A value of the frequency shift  $\Delta f$  was fixed for each simulation and then the vertical position of the tip with respect to the sample was determined. The separation of the tip with respect to the substrate was calculated using eq. (4.5), which describes the sphere-surface van der Waals potential energy. The total tip-substrate interaction should also include the presence of a thin layer of APTES or a residual quantity of  $Mg^{2+}$  on the substrate surface, according to the method of DNA deposition. Experiments described in figs. 3.12 and 3.13 in section 3.4.4 and figs. 4.1 and 4.3 in section 4.1 showed a substantial agreement in the measured value of the height for both the methods of deposition when using the same kind of tip to image DNA (in this case DLC). This value was 1 nm circa for all experiments. Therefore, I assumed that the method of deposition was non influential on the DNA height and that it was not necessary to consider the effect of both APTES and  $Mg^{2+}$  on the tip-substrate potential energy in my calculations. The Hamaker constant was set to  $A_H = 1.35 \times 10^{-19}$  J for the calculation of the substrate-silicon tip separation [62]. The value  $A_H = 1.7 \times 10^{-19}$  J reported for the diamond-mica Hamaker constant in vacuum [68] was used for the substrate-DLC tip separation.

The separation at the given value of  $\Delta f$  was also determined on the top of the DNA molecule.

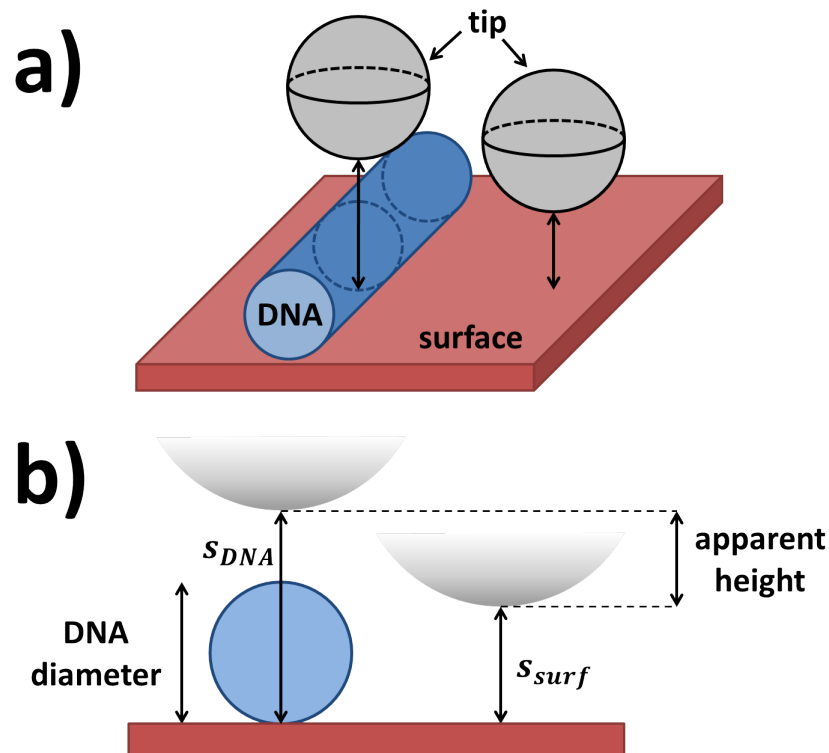


Figure 4.17: **a)** Sketch of the spherical tip passing over the cylinder representing the DNA molecule and over the surface. **b)** The DNA diameter, the tip-DNA separation  $s_{DNA}$ , the tip-substrate separation  $s_{surf}$  and the apparent height are represented here.

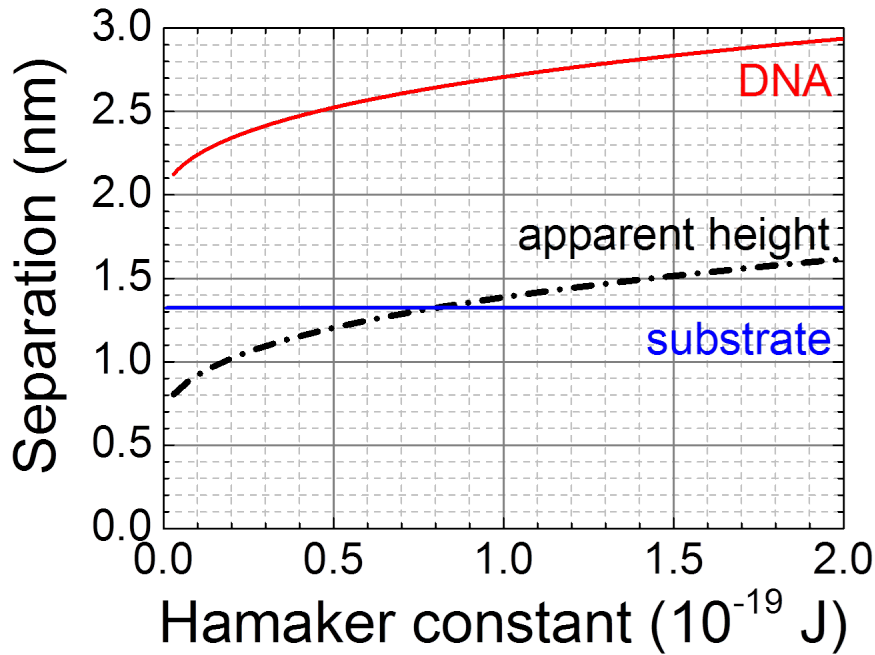


Figure 4.18: Tip separations over the DNA molecule (in red) and over the substrate (in blue), as a function of the tip-DNA Hamaker constant. The DNA molecule was modeled as an infinitely long cylinder. The simulation was done assuming a DLC tip as a probe. Parameters:  $r_{tip} = 2$  nm,  $f_0 = 325$  kHz,  $k = 40$  N/m,  $A_{H,surf} = 1.7 \times 10^{-19}$  J,  $\Delta f = -1.5$  Hz.

The total van der Waals potential energy acting on the tip in this position was assumed to be the sum of the tip-substrate and tip-DNA potential energies. The tip-DNA Hamaker constant has been left as a variable. It is known that its typical order of magnitude is  $10^{-19}$  circa for a wide variety of materials, and the DNA height was calculated as a function of the Hamaker constant in a range close to this value.

The separation curves  $s(\Delta f)$  were calculated as inverse functions of the frequency shift vs. distance curves, obtained applying eq. (1.36) to two specific cases: 1) when the total force was only due to the substrate; 2) when the total force was determined by the sum of the DNA and substrate contributions (that is, when the tip was over the DNA molecule). In both cases, the separation has been defined as the distance between the bottom of the tip and the substrate plane.

Fig. 4.17 illustrates the difference between the real DNA diameter (in this case, the DNA shape was modeled as a cylinder) and the calculated (or apparent) DNA height. The separation when the tip is over the DNA molecule has been defined as  $s_{DNA}(\Delta f)$ , while the separation when the tip is over the bare substrate as was called  $s_{surf}(\Delta f)$ . Therefore, the calculated height is equal to  $s_{DNA}(\Delta f) - s_{surf}(\Delta f)$ . A plot of both  $s_{DNA}$  and  $s_{surf}$  and of the apparent DNA height, all as a function of the tip-DNA Hamaker constant, is shown in fig. 4.18.

Calculations of the apparent height were made in order to simulate the conditions in which

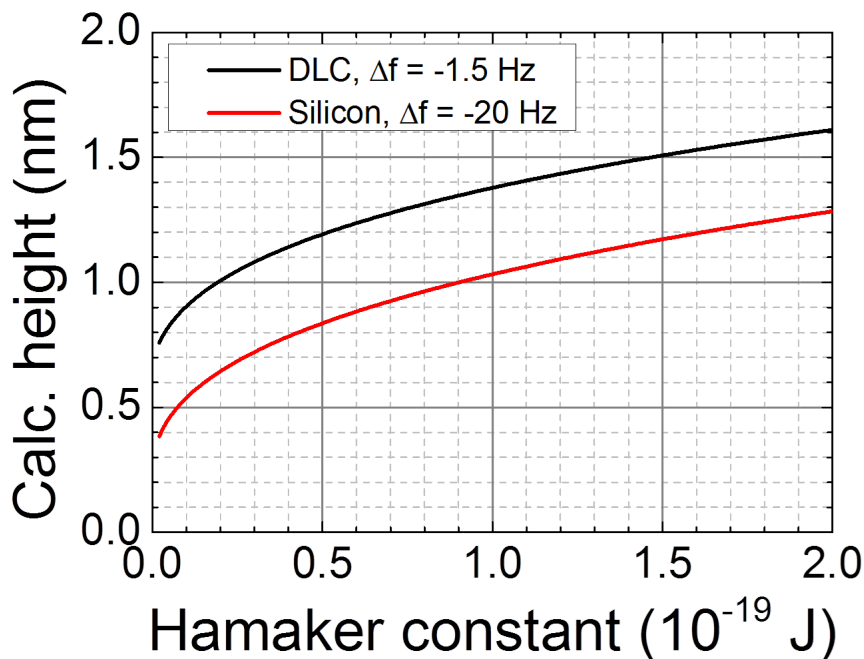


Figure 4.19: Calculated DNA height as a function of the tip-DNA Hamaker constant in a simulation of a FM AFM experiment. DNA was modeled as an infinitely long cylinder. Black curve: DNA measured with a DLC tip, simulation of the experiment in fig. 4.1 ( $r_{tip} = 2$  nm,  $f_0 = 336245$  Hz,  $k = 40$  N/m,  $A_{H,surf} = 1.7 \times 10^{-19}$  J,  $\Delta f = -1.5$  Hz). Red curve: DNA measured with a silicon tip, simulation of the experiment in fig. 4.2 ( $r_{tip} = 10$  nm,  $f_0 = 356157$  Hz,  $k = 14$  N/m,  $A_{H,surf} = 1.35 \times 10^{-19}$  J,  $\Delta f = -20$  Hz).

experiments discussed in section 4.1 were done. The tip radius, the cantilever spring constant and the tip-substrate Hamaker constant were adapted to the experiments, according to the kind of tip used. In the same way, the resonant frequency and the frequency shift were set to real value of the relative experiments.

The calculated DNA heights for the cylindrical DNA model are shown in fig. 4.19. The first observation that can be done is that the apparent height of DNA when using a silicon tip is smaller than the one obtained with a DLC tip. This is in qualitative agreement with the experimental results shown in section 4.1. Santos et al. [62] evaluated the Hamaker constant for the DNA-silicon tip interaction making AM AFM experiments in air, reporting a value of  $A_H = 0.3 \div 0.4 \times 10^{-19}$  J. In my simulation with a silicon tip (red curve in fig. 4.19), the calculated DNA height was between 0.7 and 0.8 nm in the same range of  $A_H$ . This evaluation is in perfect agreement with the DNA height measured with a silicon tip (experiment shown in fig. 4.2), where a value equal to 0.72 nm was obtained.

In experiments where DLC tips were used, The measured DNA height was 0.95 nm for DNA molecules deposited on APTES/mica and 0.97 nm for DNA molecules deposited with  $Mg^{2+}$  on mica. Considering the simulation made for DNA measured with a DLC tip (black curve in fig. 4.19), a calculated height of approximately 1 nm is obtained for values of the DNA-DLC tip

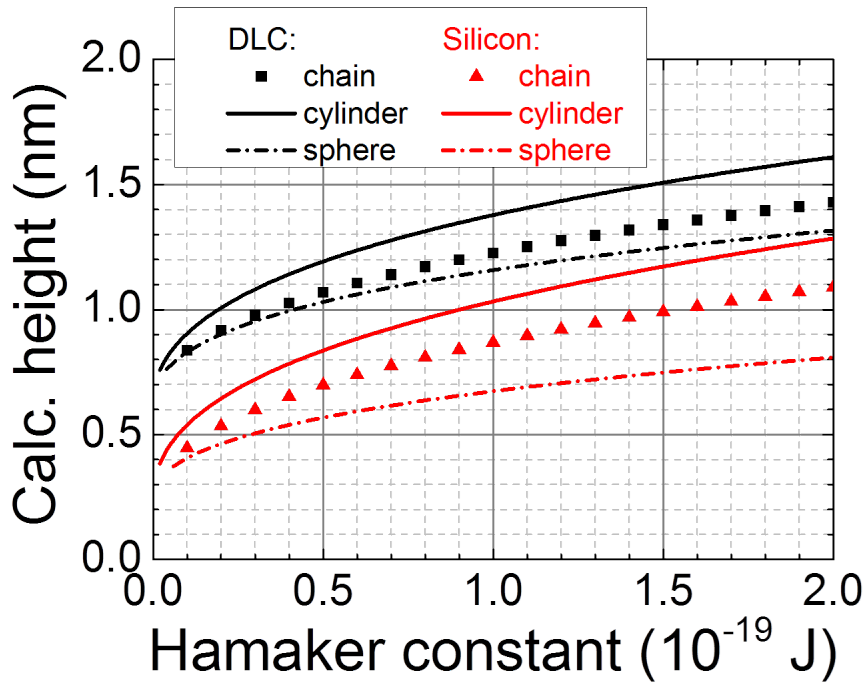


Figure 4.20: Calculated DNA height as a function of the tip-DNA Hamaker constant. DNA was modeled as a cylinder (continuous line), as a chain of spheres (points) and as a single sphere (dash-dotted line). Simulations of experiments with a DLC tip are shown in black ( $r_{tip} = 2$  nm,  $f_0 = 336245$  Hz,  $k = 40$  N/m,  $A_{H,surf} = 1.7 \times 10^{-19}$  J,  $\Delta f = -1.5$  Hz). Simulations of experiments with a silicon tip are shown in red ( $r_{tip} = 10$  nm,  $f_0 = 356157$  Hz,  $k = 14$  N/m,  $A_{H,surf} = 1.35 \times 10^{-19}$  J,  $\Delta f = -20$  Hz).

Hamaker constant close to  $0.2 \times 10^{-19}$  J.

The calculation of the DNA height was repeated using the model representing the DNA molecule as a chain of spheres. A series of 20 contiguous spheres having a radius equal to 1 nm was used. The height calculated on the top of the 10th was used as definition of the molecule height. This was done in order to avoid side effects which affected the calculation when considering the most external spheres. Results are plotted as a function of the tip-DNA Hamaker constant in fig. 4.20. The calculated DNA height was slightly smaller if compared to the similar calculations made assuming the cylindrical DNA model. This happened for simulations of experiments with both DLC and silicon tips. In this case, my simulations reproduced the experimental DNA height obtained with a silicon tip (0.72 nm) when the tip-DNA Hamaker constant was approximatively at  $0.5 \times 10^{-19}$  J, while they approximated the experimental height measured with DLC tips (1 nm circa) for values of the tip-DNA Hamaker constant in the interval between  $0.3$  and  $0.4 \times 10^{-19}$  J.

As an additional comparison, I plotted in fig. 4.20 evaluations of the DNA height obtained considering the interaction of the tip only with the 10th sphere. Simulations with a DLC tip showed that the contribution of the nearest sphere was dominant for small values of the tip-DNA Hamaker constant. The height values calculated using the chain of 20 spheres or

using only the 10th sphere were almost exactly superposed for  $A_H < 0.5 \times 10^{-19}$  J. On the contrary, there was a clear difference in evaluations made with silicon tips, showing a most delocalized interaction of tip which can be mainly ascribed to the larger tip radius.

The height calculations presented in this section allowed estimating the average tip-DNA Hamaker constant in vacuum for DLC and silicon tips. Taking into account the simulations made with both the models of the DNA molecule I obtained a value of  $0.3 \div 0.5 \times 10^{-19}$  J for the DNA-silicon Hamaker constant, which is consistent with the evaluation made by Santos et al. in [62]. Moreover, I estimated a value of  $0.2 \div 0.4 \times 10^{-19}$  J for the DNA-DLC tip Hamaker constant, that to my knowledge is the first evaluation ever made for this couple of materials.

#### 4.3.2 Calculations of the groove contrast in FM AFM

In the previous section I showed how to use the model of the chain of spheres to evaluate the DNA height. The position of the tip apex with respect to the substrate plane was defined as separation. I calculated the separation vs. frequency shift curve in a reference position along the chain of spheres, that is over the center of the 10th sphere. I calculated a second separation vs. frequency shift curve supposing that the tip was over the bare substrate. Then I fixed a certain  $\Delta f$  set point and I determined the apparent height as the difference between the two separation values.

I used the same model to quantify the expected groove contrast over a DNA molecule in a FM AFM experiment, simulating the movement of the AFM tip along the molecular axis. To accomplish this task, it was necessary to calculate a series of separation vs. frequency shift curves along the chain of spheres and then to evaluate the height as a function of the position. Again, I assumed the chain to be made of 20 spheres having a radius equal to 1 nm. A sketch of this kind of simulation is shown in fig. 4.21. When moving over the chain of spheres, the tip vertical position varies according to the underlying topography in order to keep constant the  $\Delta f$  setpoint.

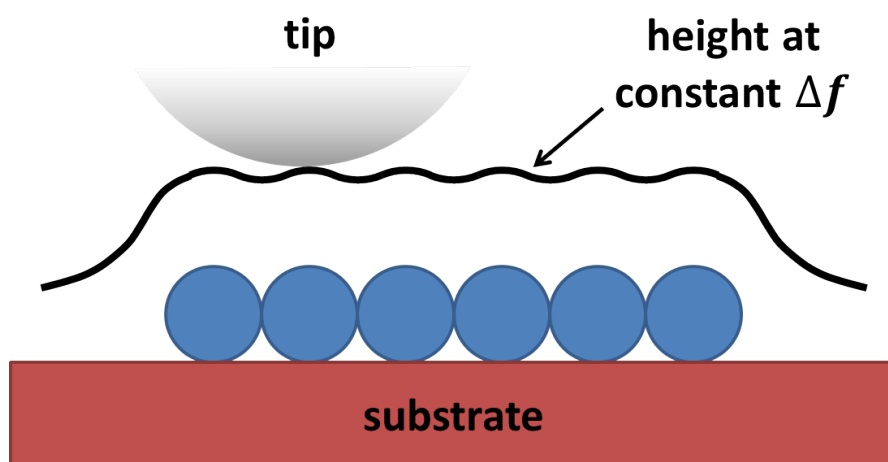


Figure 4.21: Representation of the AFM tip moving over the DNA molecule (modeled as a linear chain of spheres) at constant frequency shift.

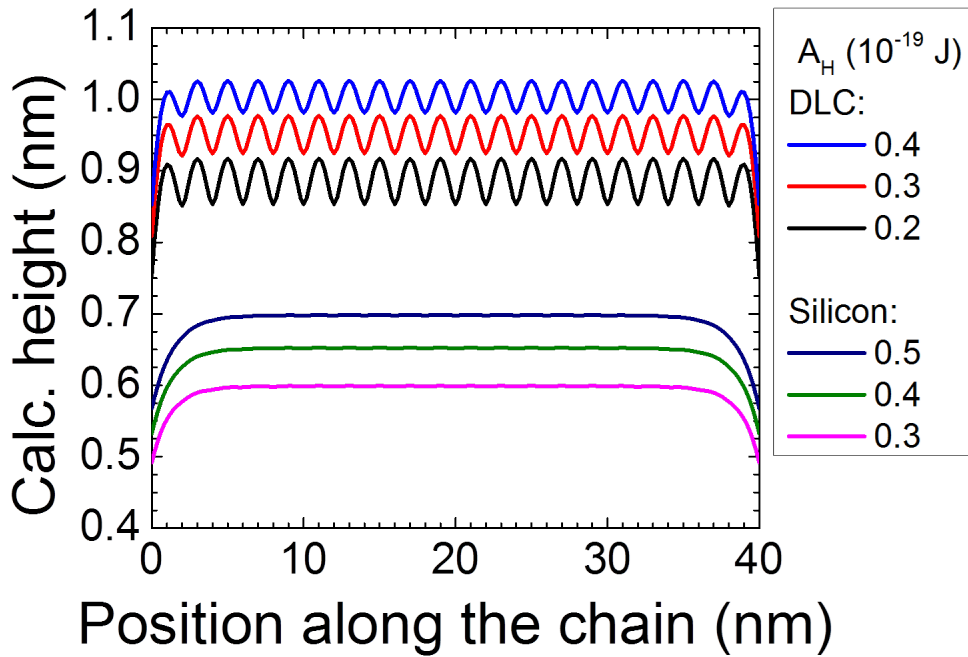


Figure 4.22: Apparent heights as a function of the position along the chain of spheres are plotted here. Calculations have been done supposing to use both a DLC tip ( $r_{tip} = 2$  nm,  $f_0 = 336245$  Hz,  $k = 40$  N/m,  $A_{H,surf} = 1.7 \times 10^{-19}$  J,  $\Delta f = -1.5$  Hz) and a silicon tip ( $r_{tip} = 10$  nm,  $f_0 = 356157$  Hz,  $k = 14$  N/m,  $A_{H,surf} = 1.35 \times 10^{-19}$  J,  $\Delta f = -20$  Hz). Heights for different values of the tip-DNA Hamaker constant  $A_H$  are shown.

Results of these calculations are shown in fig. 4.22, where apparent heights are plotted as a function of the position along the chain of spheres. Tip-DNA Hamaker constant were chosen according to the evaluation made in section 4.3.1. A contrast was clearly visible for all the curves relative to the DLC tip, with maxima corresponding to the centers of the spheres and minima in between two contiguous spheres. On the contrary, curves calculated supposing to use a silicon tip for the FM AFM experiment appeared almost flat. This difference in contrast between DLC and silicon tips is consistent with the experimental results I obtained when imaging DNA molecules by FM AFM and explains why the DNA double helix periodicity was observed only when using sharp DLC tips.

I defined the calculated groove contrast as the difference between the height over the center of the 10th sphere and the height at the center of the chain, that is in the “groove” between the 10th and the 11th sphere. The calculated contrast for both DLC and silicon tips is plotted as a function of the tip-DNA Hamaker constant in fig. 4.23. The plot shows an expected groove contrast having an average value of 0.05 nm circa between  $0.2$  and  $0.4 \times 10^{-19}$  J for calculation relative to the DLC tip. This value is in good agreement with the measured groove contrast in FM AFM imaging experiments (see fig. 3.12 f)).

In spite of its simplicity, the DNA model discussed in this section allowed reproducing the performances of DLC and silicon tips in FM AFM imaging. Additional refinements of the model

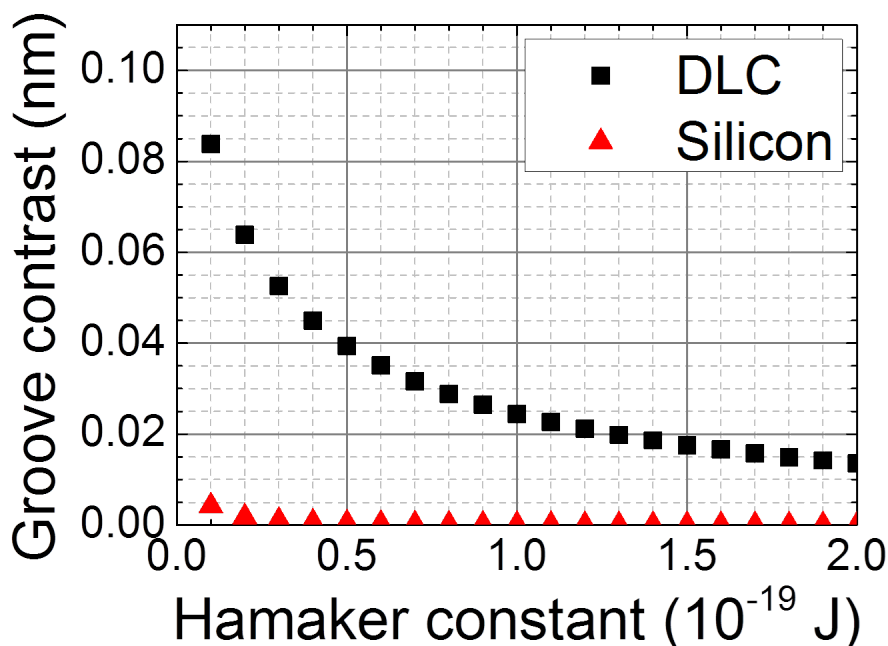


Figure 4.23: Calculated groove contrast as a function of the tip-DNA Hamaker constant. Calculations have been done supposing to use both a DLC tip ( $r_{tip} = 2$  nm,  $f_0 = 336245$  Hz,  $k = 40$  N/m,  $A_{H,surf} = 1.7 \times 10^{-19}$  J,  $\Delta f = -1.5$  Hz) and a silicon tip ( $r_{tip} = 10$  nm,  $f_0 = 356157$  Hz,  $k = 14$  N/m,  $A_{H,surf} = 1.35 \times 10^{-19}$  J,  $\Delta f = -20$  Hz).

are required in order to explain why it was not possible to observe also minor grooves in my experiments. Moreover, a better understanding of the forces acting on the tip at short distance is needed to overcome the approximation of considering only van der Waals contributions to the tip-DNA interaction.

#### 4.3.3 Applicability to the study of other biomolecules

Simple models have been defined in this chapter to give an explanation to the reduced value of DNA height with respect to its theoretical diameter. Moreover, they allowed evaluating the Hamaker constant of the van der Waals interaction between DNA and tips of different materials. The same methodology can be easily extended to the study of other biological molecules whose shape is compatible with the models here introduced. There are many biological samples of interest can be assimilated to a cylinder, such as amyloid fibrils, while several proteins have a globular shape and can be approximated to a sphere. Also for these molecules, the measured value of the height can have a mismatch with respect to the real diameter. In this section, I will briefly show how both the tip-molecule and the tip-substrate Hamaker constants can affect the measurement of the molecule height. I will also quantify the error made on the height estimation as a function of the molecule diameter.

First of all I recalculated the apparent height of an infinitely long cylinder having a radius equal

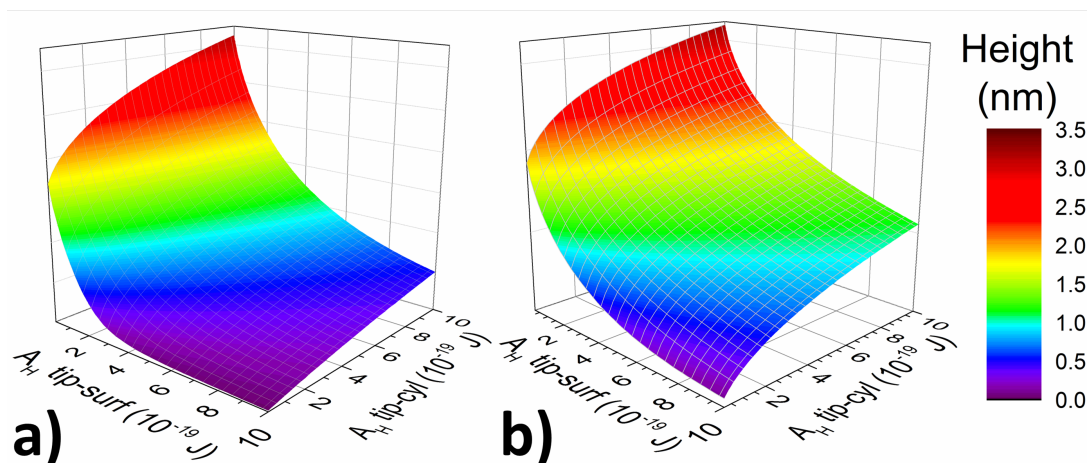


Figure 4.24: In this figure the apparent height as a function of both the tip-cylinder Hamaker constant and the tip-substrate Hamaker constant is plotted. In **a)** the result of the calculation made for a DLC-like tip ( $r_{\text{tip}} = 2$  nm,  $f_0 = 325$  kHz,  $k = 40$  N/m,  $\Delta f = -2$  Hz) is shown, while **b)** corresponds to the result of the calculation for a Mikromasch B-like tip ( $r_{\text{tip}} = 10$  nm,  $f_0 = 315$  kHz,  $k = 14$  N/m,  $\Delta f = -20$  Hz).

to 1 nm, letting to vary in this case also the tip-substrate Hamaker constant. Calculations were done supposing to simulate height measurements made both with a DLC and with a silicon tip. Both Hamaker constants were varied between 0 and  $10^{-18}$  J. Results in fig. 4.24 show that our calculation can be generalized to any tip-cylindrical molecule combination and if the Hamaker constants are known it is sufficient to use these two values to extract the apparent height.

Figs. 4.25 and 4.26 illustrate the importance of the AFM height measurement error as a function of the size of the molecule and its shape. As it can be seen, the error is bigger for spherical molecules than for cylindrical ones. The other important aspect is that the relative error is much more important for small molecules than for the bigger ones (the percentage of error with respect to the height can range from more than 50% for molecules whose height is less or equal to 2 nm) but it typically becomes less than 10% for molecules whose height is 10 nm or more. In conclusion, it appears that the real mechanism of contrast must be taken into account for a correct evaluation of the height when measuring small single molecules, while for molecule diameters of about 10 nm or more the height measured by FM AFM imaging is a good approximation of the real value.



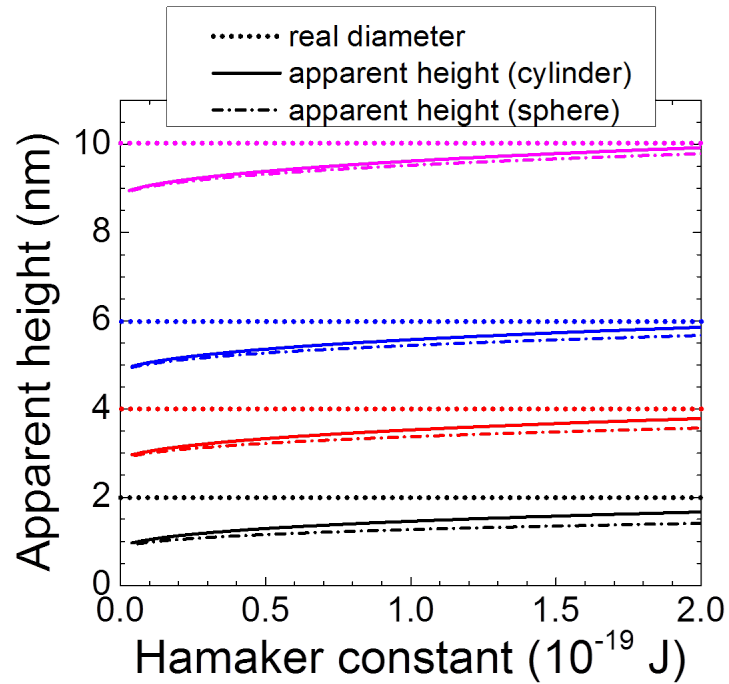


Figure 4.25: Calculated heights over a cylinder (continuous lines) and over a sphere (dash-dotted lines). The cylinder and the sphere are supposed to lie on mica. Calculations were made for a DLC-like tip ( $r_{tip} = 2$  nm,  $f_0 = 325$  kHz,  $k = 40$  N/m,  $\Delta f = -1.5$  Hz,  $A_{H,surf} = 1.7 \times 10^{-19}$  J) and different cylinder/sphere diameters  $d$ . Black curves:  $d = 2$  nm; red curves:  $d = 4$  nm; blue curves:  $d = 6$  nm; magenta curves:  $d = 10$  nm.

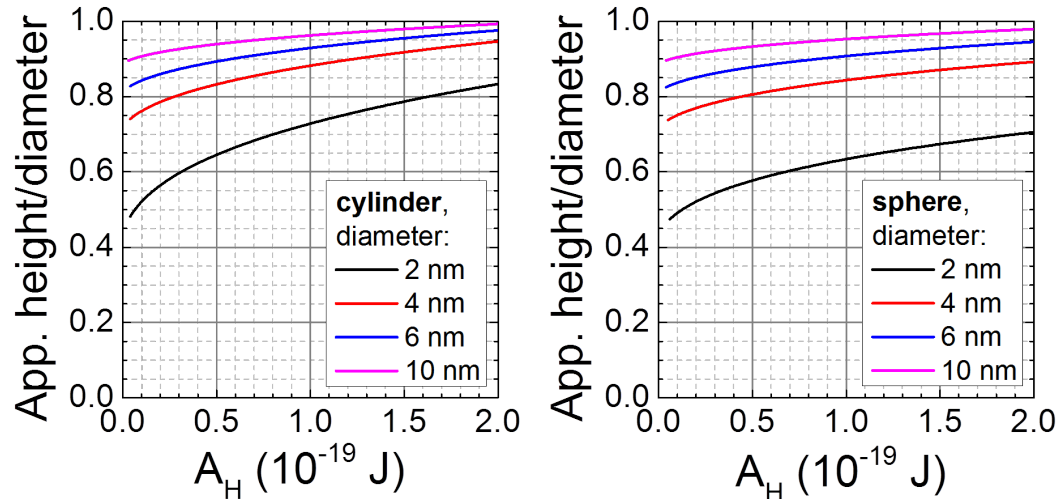


Figure 4.26: In this figure, the calculated heights shown in fig. 4.25 have been normalized with respect to the corresponding value of  $d$ . Calculations relative to cylinders are plotted on the left, while the ones relative to spheres are shown on the right. The color code is the same than fig. 4.25.



## 5 Conclusions

In this thesis I used Frequency Modulation AFM to study the conformation of DNA molecules in vacuum in order to understand if the physiological structure was conserved also in a highly dehydrated environment. A transition from the most common DNA B-form to the A-form is expected in dry conditions. DNA samples were prepared depositing the molecules on mica surfaces according to two different procedures, that is functionalizing the surface of mica with APTES or using  $Mg^{2+}$  ions. It is known that the APTES leads to a stronger attachment of DNA molecules with respect to  $Mg^{2+}$  ions. After deposition, samples prepared with the two methods were put in vacuum and imaged by FM AFM. The statistical analysis of the molecule lengths reported in section 3.4.2 showed that the average value of the measured DNA length was very consistent with the expected DNA length. The length histogram obtained with the  $Mg^{2+}$  deposition method showed a reduction of the DNA length, indicating a partial transition to the A-form configuration.

High resolution FM AFM images of DNA molecules deposited on APTES/mica showed in several case a corrugation over portions of DNA molecules that was compatible with the B-DNA double helix periodicity, when sharp Diamond-Like Carbon (DLC) tips were used as probe (section 3.4.4). This result was never obtained when using tips with a larger apex radius like Mikromasch silicon 10 nm radius tips or when molecules deposited with  $Mg^{2+}$  were studied.

However, most commonly non-contact AFM images did not allow observing any particular fine structure over DNA molecules even when deposited on APTES/mica. I assumed that this could have been in part due to the long range of van der Waals forces leading to the averaging of the signal over several nm of DNA. A confirmation of this hypothesis was obtained making constant height frequency shift maps over the DNA molecules. It showed that portions of DNA, which appeared in the usual pseudo-cylindrical shape in non-contact imaging, revealed a corrugation in frequency shift maps when the separation between the tip and the sample was progressively reduced (section 3.5.2). The periodicity of the corrugation was in some points similar to the double helix periodicity of B-DNA, but in general there was a lot of variability on this value. Constant height images allowed discovering details over DNA molecules unseen in normal imaging and absent in frequency shift maps made over the substrate. In a similar way force vs. separation curves measured along the DNA molecular axis allowed to appreciate a periodicity near to the maximum of the attractive force that could be correlated with the

## Chapter 5. Conclusions

---

presence of major grooves and sometimes also minor grooves (section 3.6.2).

The observation of a DNA height significantly smaller with respect to the theoretical diameter of DNA contrasted with the idea that DNA could still be in its physiological conformation. I modeled the interaction between the DNA and two types of AFM tips (silicon and DLC tips used for all the measurements presented in this thesis) and I made calculations to estimate the DNA height in non-contact AFM imaging experiments. I found that my models correctly described the DNA height loss (section 4.3.1). Moreover, I was capable to estimate tip-DNA Hamaker constants for DLC and silicon tips. My calculations also allowed to explain why the groove contrast was never observed in non-contact AFM imaging with silicon tips.

In conclusion, my experiments demonstrated that parts of DNA molecules still remain in the physiological B-form after being put in a highly dehydrated environment. It is rarely possible to appreciate it in non-contact AFM imaging due to intrinsic limitations of the technique. The strong interaction with APTES avoids the relaxation of the molecules. As a future perspective, it will be possible to apply the same methods I have developed in this thesis to the study of other single biological molecules. I have already obtained preliminary results on  $\alpha$ -synuclein molecules which are very promising.

# Bibliography

- [1] L. Schermelleh, R. Heintzmann, and H. Leonhardt, *A guide to super-resolution fluorescence microscopy*, *Journal of Cell Biology* 190, 2 (2010), 165.
- [2] G. Binnig, H. Rohrer, *Scanning tunneling microscopy*, *IBM Journal of Research and Development* 30, 4 (1986), 355.
- [3] G. Binnig, C. F. Quate, C. Gerber, *Atomic Force Microscope*, *Physical Review Letters* 56, 9 (1986), 930.
- [4] T. R. Albrecht, P. Grütter, D. Horne, and D. Rugar, *Frequency modulation detection using high-Q cantilevers for enhanced force microscope sensitivity*, *Journal of Applied Physics* 69, 2 (1991), 668.
- [5] R. García, R. Pérez, *Dynamic atomic force methods*, *Surface Science Reports* 47 (2002), 197-301.
- [6] F. J. Giessibl, *Advances in atomic force microscopy*, *Reviews of Modern Physics* 75, 3 (2003), 949.
- [7] A. Schirmeisen and H. Hölscher, *Physical Review B* 72 (2005), 045431.
- [8] F. J. Giessibl, *Forces and frequency shifts in atomic-resolution dynamic-force microscopy*, *Physical Review B* 56, 24 (1997), 16010.
- [9] J. E. Sader, S. P. Jarvis, *Accurate formulas for interaction force and energy in frequency modulation force spectroscopy*, *Applied Physics Letters* 84, 10 (2004), 1801.
- [10] A. Radenovic, *Development of low temperature Atomic Force Microscope for biological application*, Ph. D. thesis (2003), University of Lausanne (UNIL), Switzerland.
- [11] S. Tobenas, *Cryo-AFM development for high resolution DNA imaging and spectroscopy*, Ph. D. thesis (2008), Ecole Polytechnique Fédérale de Lausanne (EPFL), Switzerland, <http://infoscience.epfl.ch/record/115113>.
- [12] Newport Inc., Deere Avenue 1791, Irvine, CA 92606, USA.
- [13] OZ-Optics Ltd., 219 Westbrook Road, Ottawa, ON K0A 1L0, Canada, [http://www.ozoptics.com/ALLNEW\\_PDF/DTS0081.pdf](http://www.ozoptics.com/ALLNEW_PDF/DTS0081.pdf).
- [14] <http://www.spmtips.com/afm-probes.afm>.

## Bibliography

---

- [15] D. Klinov, S. Magonov, *Appl. Phys. Lett.* 84, 14 (2004), 2697-2699.
- [16] A.P.E. Research, Area Science Park, Basovizza Campus, s.s. 14, Km 163.5, Building Q, 34149 Trieste, <http://www.aperesearch.com/default.html>.
- [17] <http://www.specs-zurich.com/upload/cms/user/OC4ProductBrochure.pdf>.
- [18] M. Guggisberg, M. Bammerlin, C. Loppacher, O. Pfeiffer, A. Abdurixit, V. Barwich, R. Bennewitz, A. Baratoff, E. Meyer, and H.-J. Güntherodt, *Separation of interactions by noncontact force microscopy*, *Physical Review B* 61, 16 (2000), 11151-11155.
- [19] H. C. Hamaker, *The London-van der Waals attraction between spherical particles*, *Physica* 4, 10 (1937), 1058-1072.
- [20] <http://pubs.rsc.org/en/content/articlehtml/2010/cp/b924956g>.
- [21] [http://en.wikipedia.org/wiki/File:DNA\\_chemical\\_structure.svg](http://en.wikipedia.org/wiki/File:DNA_chemical_structure.svg).
- [22] <http://www.bbc.co.uk/schools/gcsebitesize/science/images/bidnabases.jpg>.
- [23] J. D. Watson and F. H. C. Crick, *A Structure for Deoxyribose Nucleic Acid*, *Nature* 171 (1953), 737-738.
- [24] J. D. Watson and F. H. C. Crick, *Genetical Implications of the structure of Deoxyribonucleic Acid*, *Nature* 171 (1953), 964-967.
- [25] R. Franklin and R. G. Gosling, *Molecular Configuration in Sodium Thymonucleate*, *Nature* 171 (1953), 740-741.
- [26] R. Franklin and R. G. Gosling, *Evidence for 2-Chain Helix in Crystalline Structure of Sodium Deoxyribonucleate*, *Nature* 172 (1953), 156-157.
- [27] A. Ghosh and M. Bansal, *A glossary of DNA structures from A to Z*, *Acta Crystallographica D* 59 (2003), 620-626.
- [28] A. Rich and S. Zhang, *Z-DNA: the long road to biological function*, *Nature Reviews Genetics* 4 (2003), 566-572.
- [29] [http://biotech.christopher-vidal.com/A-DNA,\\_B-DNA\\_and\\_Z-DNA.jpg](http://biotech.christopher-vidal.com/A-DNA,_B-DNA_and_Z-DNA.jpg).
- [30] R. E. Dickerson, H. R. Drew, B. N. Conner, R. M. Wing, A. V. Fratini and M. L. Kopka, *The Anatomy of A-, B-, and Z-DNA*, *Science* 216, 4545 (1982), 475-485.
- [31] S. L. Wolfe, *Molecular and Cellular Biology*, Wadsworth Publishing Company, Belmont, California, ISBN 0-534-12408-9 (1993).
- [32] [http://limbiclab.files.wordpress.com/2012/12/limbic\\_lab\\_dna\\_transcription\\_diagram1.png](http://limbiclab.files.wordpress.com/2012/12/limbic_lab_dna_transcription_diagram1.png).
- [33] <http://dna.microbiologyguide.com/s/10002/pics/danreplicationfork.png>.
- [34] G. Elgar and T. Vavouri, *Tuning in to the signals: noncoding sequence conservation in vertebrate genomes*, *Trends in Genetics* 24, 7 (2008), 344-352.

- [35] F. A. Aldaye, A. L. Palmer, H. F. Sleiman, *Assembling Materials with DNA as the Guide*, Science 321 (2008), 1795-1799.
- [36] A. V. Pinheiro, D. Han, W. M. Shih, and H. Yan, *Challenges and opportunities for structural DNA nanotechnology*, Nature Nanotechnology 6 (2011), 763-772.
- [37] P. W. K. Rothemund, *Folding DNA to create nanoscale shapes and patterns*, Nature 440, 7082 (2006), 297-302.
- [38] W. M. Shih, J. D. Quispe, and G. F. Joyce, *A 1.7-kilobase single-stranded DNA that folds into a nanoscale octahedron*, Nature 427, 6975 (2004), 571-660.
- [39] J. Nangreave, D. Han, Y. Liu and H. Yan, *DNA origami: a history and current perspective*, Current Opinion in Chemical Biology 14 (2010), 608-615.
- [40] Y. Ke, S. Lindsay, Y. Chang, Y. Liu, H. Yan, *Self-Assembled Water-Soluble Nucleic Acid Probe Tiles for Label-Free RNA Hybridization Assays*, Science 319 (2008), 180-183.
- [41] N. V. Voigt, T. Tørring, A. Rotaru, M. F. Jacobsen, J. B. Ravnsbæk, R. Subramani, W. Mamdough, J. Kjems, A. Mokhir, F. Besenbacher and K. V. Gothelf, *Single-molecule chemical reactions on DNA origami*, Nature Nanotechnology 5 (2010), 200-203.
- [42] A. Kuzyk, K. T. Laitinen and P. Törmä, *DNA origami as a nanoscale template for protein assembly*, Nanotechnology 20 (2009), 235305.
- [43] H. T. Maune, S. Han, R. D. Barish, M. Bockrath, W. A. Goddard III, P. W. K. Rothemund and E. Winfree, *Self-assembly of carbon nanotubes into two-dimensional geometries using DNA origami templates*, Nature Nanotechnology 5 (2010), 61-66.
- [44] I. H. Stein, C. Steinhauer, and P. Tinnefeld, *Single-Molecule Four-Color FRET Visualizes Energy-Transfer Paths on DNA Origami*, Journal of the American Chemical Society 133 (2011), 4193-4195.
- [45] B. Giese, *Long-Distance Charge Transport in DNA: The Hopping Mechanism*, Accounts of Chemical Research 33, 9 (2000), 631-636.
- [46] G. B. Schuster, *Long-Range Charge Transfer in DNA: Transient Structural Distortions Control the Distance Dependence*, Accounts of Chemical Research 33, 4 (2000), 253-260.
- [47] D. Porath, A. Bezryadin, S. de Vries and C. Dekker, *Direct measurement of electrical transport through DNAmolecules*, Nature 403 (2000), 635-638.
- [48] J. D. Slinker, N. B. Muren, S. E. Renfrew and J. K. Barton, *DNA charge transport over 34 nm*, Nature Chemistry 3 (2011), 228-233.
- [49] D. Dulić, S. Tuukkanen, C.-L. Chung, A. Isambert, P. Lavie and A. Filoramo, *Direct conductance measurements of short single DNA molecules in dry conditions*, Nanotechnology 20 (2009), 115502.
- [50] A. J. Storm, J. van Noort, S. de Vries, and C. Dekker, *Insulating behavior for DNA molecules between nanoelectrodes at the 100 nm length scale*, Applied Physics Letters 79, 23 (2001), 3881-3883.

## Bibliography

---

- [51] A. Y. Kasumov, M. Kociak, S. Guéron, B. Reulet, V. T. Volkov, D. V. Klinov, H. Bouchiat, *Proximity-Induced Superconductivity in DNA*, *Science* 291 (2001), 280-282.
- [52] M. Wolter, P. B. Woiczikowski, M. Elstner, and T. Kubař, *Response of the electric conductivity of double-stranded DNA on moderate mechanical stretching stresses*, *Physical Review B* 85 (2012), 075101.
- [53] H. G. Hansma, D. E. Laney, M. Bezanilla, R. L. Sinsheimer, and P. K. Hansma, *Applications for Atomic Force Microscopy of DNA*, *Biophysical Journal* 68 (1995), 1672-1677.
- [54] H. G. Hansma, and P. K. Hansma, *Potential applications of atomic force microscopy of DNA to the human genome project*, *Proceedings of the SPIE-The International Society for Optical Engineering (USA)* 1891 (1993), 66-70.
- [55] J. Mou, D. M. Czajkowsky, Y. Zhang, Z. Shao, *High-resolution atomic-force microscopy of DNA: the pitch of the double helix*
- [56] C. Leung, A. Bestembayeva, R. Thorogate, J. Stinson, A. Pyne, C. Marcovich, J. Yang, U. Drechsler, M. Despont, T. Jankowski, M. Tschöpe, and B. W. Hoogenboom, *Atomic Force Microscopy with Nanoscale Cantilevers Resolves Different Structural Conformations of the DNA Double Helix*, *Nano Letters* 12 (2012), 3846-3850.
- [57] S. Ido, K. Kimura, N. Oyabu, K. Kobayashi, M. Tsukada, K. Matsushige, and H. Yamada, *Beyond the Helix Pitch: Direct Visualization of Native DNA in Aqueous Solution*, *ACS Nano* 7, 2 (2013), 1817-1822.
- [58] J. Adamcik, F. Valle, G. Witz, K. Rechendorff, and G. Dietler, *The promotion of secondary structures in single-stranded DNA by drugs that bind to duplex DNA: an atomic force microscopy study*, *Nanotechnology* 19 (2008), 384016.
- [59] Z. Liu, Z. Li, H. Zhou, G. Wei, Y. Song and L. Wang, *Immobilization and condensation of DNA with 3-aminopropyltriethoxysilane studied by atomic force microscopy*, *Journal of Microscopy* 218, 3 (2005), 233-239.
- [60] A. Y. Fadeev and T. J. McCarthy, *Self-Assembly Is Not the Only Reaction Possible between Alkyltrichlorosilanes and Surfaces: Monomolecular and Oligomeric Covalently Attached Layers of Dichloro- and Trichloroalkylsilanes on Silicon*, *Langmuir* 16, 18 (2000), 7268-7274.
- [61] F. Moreno-Herrero, J. Colchero, A. M. Baró, *DNA height in scanning force microscopy*, *Ultramicroscopy* 96, 2 (2003), 167-174.
- [62] S. Santos, M. Stefancich, H. Hernandez, M. Chiesa, and N. H. Thomson, *Hydrophilicity of a Single DNA Molecule*, *Journal of Physical Chemistry C* 116 (2012), 2807-2818.
- [63] <http://gwyddion.net/>
- [64] L. Gross, F. Mohn, N. Moll, P. Liljeroth, G. Meyer, *The Chemical Structure of a Molecule Resolved by Atomic Force Microscopy*, *Science* 325 (2009), 1110-1114.
- [65] Y. Sugimoto, P. Pou, M. Abe, P. Jelinek, R. Pérez, S. Morita and Ó. Custance, *Chemical identification of individual surface atoms by atomic force microscopy*, *Nature* 446 (2007), 64-67.



- [66] A. Cerreta, D. Vobornik, G. Di Santo, S. Tobenas, L. Alonso-Sarduy, J. Adamcik and G. Dietler, *FM-AFM constant height imaging and force curves: high resolution study of DNA-tip interactions*, Journal of Molecular Recognition 25 (2012), 486-493.
- [67] M. A. Lantz, H. J. Hug, R. Hoffmann, P. J. A. van Schendel, P. Kappenberger, S. Martin, A. Baratoff, H.-J. Güntherodt, *Quantitative Measurement of Short-Range Chemical Bonding Forces*, Science 291 (2001), 2580-2583.
- [68] L. Bergström, *Hamaker constants of inorganic materials*, Advances in Colloid and Interface Science 70 (1997), 125-169.
- [69] B. J. Albers, T. C. Schwendemann, M. Z. Baykara, N. Pilet, M. Liebmann, E. I. Altman and U. D. Schwarz, *Data acquisition and analysis procedures for high-resolution atomic force microscopy in three dimensions*, Nanotechnology 20 (2009), 264002.
- [70] C. Argento and R. H. French, *Parametric tip model and force-distance relation for Hamaker constant determination from atomic force microscopy*, Journal of Applied Physics 80 (1996), 6081-6090.
- [71] R. García and A. San Paulo, *Attractive and repulsive tip-sample interaction regimes in tapping-mode atomic force microscopy*, Physical Review B 60, 7 (1999), 4961-4967.
- [72] S. W. Montgomery, M. A. Franchek, and V. W. Goldschmidt, *Analytical Dispersion Force Calculations for Nontraditional Geometries*, Journal of Colloid and Interface Science 227 (2000), 567-584.



## ANDREA CERRETA

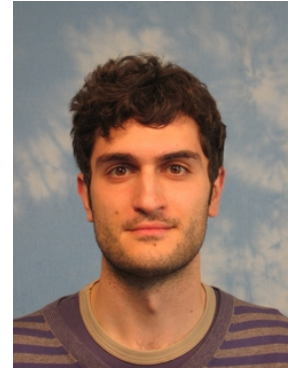
Private address: Chemin du Noirmont 13, 1004 Lausanne, Switzerland

Telephone: + 41 79 884 08 81

E-mail: [andreacerreta@inwind.it](mailto:andreacerreta@inwind.it)

Web page: <http://people.epfl.ch/andrea.cerreta>

Citizenship: Italian



### EXPERTISE

Physics, Biophysics; DNA, Amyloids; Atomic Force Microscopy (Frequency Modulation, Amplitude Modulation); Vacuum Chambers; Low Energy Electron Diffraction; Surface Analysis; Thin Films

### EDUCATION

#### 2009-2013 PhD in Physics

Thesis: Frequency Modulation Atomic Force Microscopy on Biomolecules: Force Measurements and High Resolution Images of DNA.  
Ecole Polytechnique Fédérale de Lausanne (EPFL), Lausanne, Switzerland

#### 2005-2009 Master's Degree in Physics

*Laurea Specialistica in Fisica, Curriculum di "Fisica della Materia"*  
Università La Sapienza, Roma, Italy

#### 2001-2005 Bachelor's Degree in Physics

*Laurea Triennale in Fisica*  
Università La Sapienza, Roma, Italy

### RESEARCH EXPERIENCE

#### PhD Student, April 2009 – Present

*Laboratory of the Physics of Living Matter, EPFL, Switzerland*

- Developed Frequency Modulation Atomic Force Microscopy in UHV for the study of biomolecules. Obtained highly resolved images of DNA and Amyloid fibrils. Measured and modeled the AFM probe-DNA interaction.

#### Research Assistant, January 2008 - June 2009

*LOTUS Laboratory, Physics Department, Università La Sapienza, Roma, Italy*

*Supervisors: Prof. C. Mariani, Prof. M. G. Betti*

- Studied the morphology and the structure of Cu-Phthalocyanine thin films grown in UHV over Si(111) wafers using Atomic Force Microscopy, Low Energy Electron Diffraction and Energy Dispersive X-ray Diffraction.

#### Intern, February 2005 - May 2005

*ESCA Laboratory, Chemistry Department, Università La Sapienza, Roma, Italy*

*Supervisor: Prof. C. Coluzza*

- Analyzed silicon surfaces functionalized with Porphyrin and Ferrocene molecules, using Atomic Force Microscopy in UHV.

## OTHER SKILLS

---

- **Languages:** Italian (mother tongue); fluent in English and French.

- **Computers:** Graphing and data analysis: Origin and Excel.  
Scientific computing: Mathematica.  
Image analysis: Gwiddion, SPIP.  
Programming languages: C++.

## PUBLICATIONS

---

A. Cerreta, D. Vobornik, and G. Dietler, "Fine DNA Structure Revealed by Constant Height Frequency Modulation AFM Imaging", *European Polymer Journal*, article in press (2013).

A. Cerreta, D. Vobornik, G. Di Santo, S. Tobenas, L. A. Sarduy, J. Adamcik, and G. Dietler, "FM-AFM constant height imaging and force curves: high resolution study of DNA-tip interactions", *Journal of Molecular Recognition* 25 (2012), 486-493;

A. Cerreta, D. Vobornik, S. Tobenas, J. Adamcik, L. A. Sarduy, G. Di Santo, and G. Dietler, "Fine structure of DNA in ultrahigh vacuum revealed by AFM force probing", article submitted to *Nano Letters*.

## PRESENTATIONS AT CONFERENCES

---

Oral presentation: "Quantitative AFM height measurements". 4th Multifrequency AFM Conference, Madrid, October 15-17, 2012.

Oral presentation: "Fine DNA Structure Revealed by Frequency Modulation AFM". International Conference on Scanning Probe Microscopy on Soft and Polymeric Materials, Kerkrade (Netherlands), 23-26 September 2012.

Oral presentation: "Force spectroscopy on DNA and amyloid fibrils by means of FM-AFM". 14th International Conference on non-contact Atomic Force Microscopy, Lindau (Germany), September 18-22, 2011.

Oral presentation: "FM-AFM constant height imaging and force curves DNA-tip interactions". AFM Biomed Conference, Paris, August 23-27, 2011.

Oral presentation: "Achieving sub-molecular resolution on biological samples: constant height frequency shift imaging of dsDNA by Cryo-AFM". 3rd Multifrequency AFM Conference, Madrid, March 14-15, 2011.

Poster: "High resolution imaging and force spectroscopy on DNA and other biological samples in UHV with Cryo-AFM". Swiss Soft Days (2nd Edition) at EPFL, Lausanne, June 23, 2010.

## TEACHING

---

2011/12: EPFL Lausanne, semester II: assistant, General Physics IV (prof. Dietler);

2011/12: EPFL Lausanne, semester I: assistant, General Physics III (prof. Dietler);  
2010/11: EPFL Lausanne, semester II: assistant, General Physics IV (prof. Dietler);  
2010/11: EPFL Lausanne, semester I: assistant, General Physics III (prof. Dietler);  
2009/10: EPFL Lausanne, semester II: assistant, Biophysics II (prof. Dietler);  
2009/10: EPFL Lausanne, semester I: assistant, General Physics III (prof. Dietler);